SPACOMM 2013

The Fifth International Conference on Advances in Satellite and Space Communications

ISBN: 978-1-61208-264-6

April 21 - 26, 2013

Venice, Italy

SPACOMM 2013 Editors

Timothy Pham, Jet Propulsion Laboratory, USA

Pascal Lorenz, University of Haute-Alsace, France

SPACOMM 2013

Foreword

The Fifth International Conference on Advances in Satellite and Space Communications (SPACOMM 2013), held between April 21st-26th, 2013 in Venice, Italy, continued a series of events attempting to evaluate the state of the art in academia and industry on the satellite, radar, and antennas based communications bringing together scientists and practitioners with challenging issues, achievements, and lessons learnt.

Significant efforts have been allotted to design and deploy global navigation satellite communications systems. Satellite navigation technologies, applications, and services still experience challenges related to signal processing, security, performance, and accuracy. Theories and practices on system-in-package RF design techniques, filters, passive circuits, microwaves, frequency handling, radars, antennas, and radio communications and radio waves propagation have been implemented. Services based on their use are now available, especially those for global positioning and navigation. For example, it is critical to identify the location of targets or the direction of arrival of any signal for civilians or on-purpose applications; smarts antennas and advanced active filters are playing a crucial role. Also progress has been made for transmission strategies; multiantenna systems can be used to increase the transmission speed without need for more bandwidth or power. Special techniques and strategies have been developed and implemented in electronic warfare target location systems.

We take here the opportunity to warmly thank all the members of the SPACOMM 2013 Technical Program Committee, as well as the numerous reviewers. The creation of such a high quality conference program would not have been possible without their involvement. We also kindly thank all the authors who dedicated much of their time and efforts to contribute to SPACOMM 2013. We truly believe that, thanks to all these efforts, the final conference program consisted of top quality contributions.

Also, this event could not have been a reality without the support of many individuals, organizations, and sponsors. We are grateful to the members of the SPACOMM 2013 organizing committee for their help in handling the logistics and for their work to make this professional meeting a success.

We hope that SPACOMM 2013 was a successful international forum for the exchange of ideas and results between academia and industry and for the promotion of progress in the field of satellite and space communications.

We are convinced that the participants found the event useful and communications very open. We also hope the attendees enjoyed the charm of Venice, Italy.

SPACOMM Advisory Committee:

Stelios Papaharalabos, ISARS/National Observatory of Athens, and Athens Information Technology (AIT), Greece
Piotr Tyczka, Poznan University of Technology, Poland
Michael Sauer, Corning Cable Systems, USA
Ling Pei, Finnish Geodetic Institute, Finland

SPACOMM 2013

Committee

SPACOMM Advisory Committee

Stelios Papaharalabos, ISARS/National Observatory of Athens, and Athens Information Technology (AIT), Greece
Piotr Tyczka, Poznan University of Technology, Poland
Michael Sauer, Corning Cable Systems, USA
Ling Pei, Finnish Geodetic Institute, Finland

SPACOMM 2013 Technical Program Committee

Ayman Mahmoud Ahmed, NARSS-Cairo, Egypt
Mohamed Al-Mosawi, University of Portsmouth, UK
Markos P. Anastasopoulos, National Technical University of Athens, Greece
Iva Bacic, University of Zagreb, Croatia
Marco Baldi, Università Politecnica delle Marche - Ancona, Italy
Mark Bentum, University of Twente & ASTRON, The Netherlands
Igor Bisio, University of Genoa - Italy, Italy
Shkelzen Cakaj, Telecom of Kosovo / Prishtina University, Kosovo
Enzo Alberto Candreva, University of Bologna, Italy
Emmanuel Chaput, IRIT-CNRS, France
Bruno Checcucci, Perugia University, Italy
Vittorio Dainelli, Rheinmetall Italia S.p.A. - Rome, Italy
Leonardo Dagui de Oliveira, Escola Politécnica da Universidade de Sao Paulo, Brazil
Francescantonio Della Rosa, Tampere University of Technology, Finland
Felix Flentge, ESA/ESOC HSO-GIB - Darmstadt, Germany
Thierry Gayraud, LAAS-CNRS, Université de Toulouse, France
Mathieu Gineste, Thales Alenia Space, France
Alaa Eldin Saad Hassan, NARSS-Cairo, Egypt
Konstantinos Kontis, The University of Manchester, UK
Otto Koudelka, TU Graz, Austria
Massimiliano Laddomada, Texas A&M University - Texarkana, USA
Simona Lohan, Tampere University of Technology, Finland
Krešimir Malaric, University of Zagreb, Croatia
Herwig Mannaert, University of Antwerp, Belgium
Emmanouel T. Michailidis, University of Piraeus, Greece
Marina Mondin, Politecnico di Torino, Italy
Brian Niehöfer, Technische Universität Dortmund, Germany
Nele Noels, University of Gent, Belgium
Pasquale Pace, DEIS - University of Calabria, Italy
Stelios Papaharalabos, ISARS/National Observatory of Athens, and Athens Information Technology (AIT), Greece

Copyright Information

For your reference, this is the text governing the copyright release for material published by IARIA.

The copyright release is a transfer of publication rights, which allows IARIA and its partners to drive the dissemination of the published material. This allows IARIA to give articles increased visibility via distribution, inclusion in libraries, and arrangements for submission to indexes.

I, the undersigned, declare that the article is original, and that I represent the authors of this article in the copyright release matters. If this work has been done as work-for-hire, I have obtained all necessary clearances to execute a copyright release. I hereby irrevocably transfer exclusive copyright for this material to IARIA. I give IARIA permission or reproduce the work in any media format such as, but not limited to, print, digital, or electronic. I give IARIA permission to distribute the materials without restriction to any institutions or individuals. I give IARIA permission to submit the work for inclusion in article repositories as IARIA sees fit.

I, the undersigned, declare that to the best of my knowledge, the article is does not contain libelous or otherwise unlawful contents or invading the right of privacy or infringing on a proprietary right.

Following the copyright release, any circulated version of the article must bear the copyright notice and any header and footer information that IARIA applies to the published article.

IARIA grants royalty-free permission to the authors to disseminate the work, under the above provisions, for any academic, commercial, or industrial use. IARIA grants royalty-free permission to any individuals or institutions to make the article available electronically, online, or in print.

IARIA acknowledges that rights to any algorithm, process, procedure, apparatus, or articles of manufacture remain with the authors and their employers.

I, the undersigned, understand that IARIA will not be liable, in contract, tort (including, without limitation, negligence), pre-contract or other representations (other than fraudulent misrepresentations) or otherwise in connection with the publication of my work.

Exception to the above is made for work-for-hire performed while employed by the government. In that case, copyright to the material remains with the said government. The rightful owners (authors and government entity) grant unlimited and unrestricted permission to IARIA, IARIA's contractors, and IARIA's partners to further distribute the work.

Table of Contents

Concatenated Turbo/LDPC codes for deep space communications: performance and implementation 1
Carlo Condo

Capacity Saving Analysis of Lp-problem based Allocation with Packet Loss and Power Metrics in GEO-Satellite Communications Channels 7
Igor Bisio, Stefano Delucchi, Fabio Lavagetto, and Mario Marchese

New Optical Communication Capabilities Using Nanosatellites 13
Francesco Sansone, Lorenzo Olivieri, and Alessandro Francesconi

Toward Self-Reconfiguration of Switched Ethernet Architectures in the Next Generation of Space Launchers 17
Robert Jeremy, Georges Jean-Philippe, and Divoux Thierry

Development of Wideband Dual Polarized of Microstrip Antennas for Microwave Remote Sensing 23
Akbar Eslami, Manohar Deshpande, James Lee, Henry Mishoe, Jamiiru Luttamaguzi, and Ehsan Sheybani

Hybrid Beamformer for TPMS Interference Suppression 28
Suk-seung Hwang, Cheol Park, and Seong-min Kim

Multi-millisecond GNSS Maximum Likelihood Bit Synchronization Method 34
Gerardo Ludovico Puga, Pedro Agustin Roncagliolo, and Javier Gonzalo Garcia

Turbo Decoder VLSI Architecture with Non-Recursive max* Operator for 3GPP LTE Standard 40
Ashfaq Ahmed, Maurizio Martina, and Guido Masera

A Novel Range-spread Target Detection Algorithm Based on Waveform Entropy for Missile-borne Radar 46
Bo Liu, Wenge Chang, and Xiangyang Li

A Brief Analysis of the Motion Compensation for FMCW SAR 52
Gaowei Jia, Wenge Chang, Xiangyang Li, and Zhiyong Zhao

A Novel DDS-PLL Hybrid Structure to Generate the LFM Signal 58
Zhiyong Zhao, Xiangyang Li, Wenge Chang, and Gaowei Jia

Research of Current Movements of the Earth's crust in the Territory of Almaty City 63
Zhumabek Zhantayev, Baurzhan Kurmanov, Assylkhan Bibossinov, and Kairat Sadykov

Cloud top height estimation from the Meteosat water vapor imagery using computational intelligence techniques: Preliminary results 66
Stavros Kolios, Petros Karvelis, Chrysostomos Stylios, and Periklis Tagkas

The Two-Loop Tracking Strategy for Real-Time Multi-Antenna GNSS Receivers 72
Pedro A. Roncagliolo, Jorge Cogo, and Javier G. Garcia

Concatenated Turbo/LDPC Codes for Deep Space Communications: Performance and Implementation

Carlo Condo
Department of Electronics and Telecommunications
Politecnico di Torino
Torino, Italy
carlo.condo@polito.it

***Abstract*—Deep space communications require error correction codes able to reach extremely low bit-error-rates, possibly with a steep waterfall region and without error floor. Several schemes have been proposed in the literature to achieve these goals. Most of them rely on the concatenation of different codes that leads to high hardware implementation complexity and poor resource sharing. This work proposes a scheme based on the concatenation of non-custom LDPC and turbo codes that achieves excellent error correction performance. Moreover, since both LDPC and turbo codes can be decoded with the BCJR algorithm, our preliminary results show that an efficient hardware architecture with high resource reuse can be designed.**

***Keywords*—LDPC; turbo; concatenation; deep space**

I. Introduction

The world of communications is characterized by a continuous strive for better performance: communication systems are usually pushed towards higher throughput, lower Bit-Error-Rate (BER) and lower power consumption with every generation. A particular application is deep space communications: due to the limited number of complete developments, their evolution in this domain is slower than in other application fields. Moreover, their requirements and constraint can differ substantially from all other communication environments. Transmission between spacecrafts and Earth are supposed to be sporadic events, but the limited amounts of available power and the long distances make failed reception, and consequent retransmission, an unacceptable event. For this reason, deep space missions do not require a high throughput, while at the same time they demand very strict BER and frame-error-rate (FER) performance. The Consultative Committee for Space Data Systems (CCSDS) suggests a set of rules (a *de facto* standard) for all space-related communication systems. In [1] four channel coding schemes are described, while in [2] the considered channel coding options are assembled into application-wise FEC schemes. Deep space exploration requires the use of powerful error correction codes, such as turbo codes [3], lower rate low-density-parity-check (LDPC) codes [4] and concatenated Reed-Solomon (RS) and convolutional codes. Various works have proposed deep space FEC schemes, also using codes that are different from those suggested in [1]: from custom-constructed single codes [5] to more complex concatenated schemes [6]. Concatenation between different codes has been frequently considered in order to improve performance. "Guaranteed-performance-codes" like RS or BCH codes are often used as Outer Codes (OCs) thanks to their measurable error correction capabilities, and joined to Inner Codes (ICs) such as convolutional or LDPC, used in WiMAX and DVB-S2. The same RS+convolutional FEC scheme devised in [2] allows these codes to rival with the more powerful LDPC and turbo codes. However, concatenation comes at a usually high implementation cost: decoding support for sometimes very different codes must be provided, increasing area and power consumption. Low-complexity decoders have been designed for many codes [7], [8] but steps have been recently taken towards flexibility, with area efficient multi-code decoders [9], [10].

This paper presents a deep space oriented FEC scheme by serial concatenation of LDPC and turbo codes. Section II describes how, through a particular representation of the LDPC parity check matrix, both kinds of codes can be decoded with the same algorithm, allowing very low-cost implementation of a joint decoder. The FEC scheme is described in detail in Section III. Performance of the concatenated scheme is compared with the standard requirements in Section IV, together with a set of recent works both on deep space communications and on concatenated codes. Finally, an estimation of the complexity of decoder supporting both codes is made in Section V.

II. Turbo and LDPC decoding algorithms

Convolutional Turbo Codes (or CTCs) are obtained as the parallel concatenation of two constituent Convolutional Code (CC) encoders. Consequently, also the decoder is made of two different parts, called Soft-In-Soft-Out (SISO) or Maximum-A-Posteriori (MAP) decoders, and connected by an interleaver Π and a de-interleaver Π^{-1}. Each MAP decoder implements the BCJR algorithm [11], which produces extrinsic metrics from *a priori* information. Representing the constituent CC as a trellis, let us define k as a trellis step and u as an uncoded symbol. Each decoder computes $\lambda_k[u] = \lambda_k^{apo}[u] - \lambda_k^{apr}[u] - \lambda_k[\mathbf{c}^u]$ where $\lambda_k^{apo}[u]$ is the a-posteriori information, $\lambda_k^{apr}[u]$ is the *a priori* information and $\lambda_k[\mathbf{c}^u]$ is the systematic component of the intrinsic information. The a-posteriori information is obtained as follows:

$$\lambda_k^{apo}[u] = \max_{e:u(e)=u}^{*} \{b(e)\} - \max_{e:u(e)=\tilde{u}}^{*} \{b(e)\} \qquad (1)$$

where $\tilde{u} \in \mathcal{U}$ is an uncoded symbol taken as a reference (usually $\tilde{u} = \mathbf{0}$) and $u \in \mathcal{U} \setminus \{\tilde{u}\}$ with $\mathcal{U}$ the set of uncoded

 ISBN: 978-1-61208-264-6

symbols; e is a trellis transition and $u(e)$ is the corresponding uncoded symbol. Following the Max-Log-MAP approximation [12], for a small BER degradation the $\overset{*}{\max}\{x_i\}$ function becomes $\max\{x_i\}$. The term $b(e)$ in (1) can consequently be defined as:

$$b(e) = \alpha_{k-1}[s^S(e)] + \gamma_k[e] + \beta_k[s^E(e)] \quad (2)$$

$$\alpha_k[s] = \max_{e:s^E(e)=s} \left\{\alpha_{k-1}[s^S(e)] + \gamma_k[e]\right\} \quad (3)$$

$$\beta_k[s] = \max_{e:s^S(e)=s} \left\{\beta_{k+1}[s^E(e)] + \gamma_k[e]\right\} \quad (4)$$

$$\gamma_k[e] = \lambda_k^{apr}[u(e)] + \lambda_k[\mathbf{c}(e)] \quad (5)$$

where $s^S(e)$ and $s^E(e)$ are the starting and the ending states of e, $\alpha_k[s^S(e)]$ and $\beta_k[s^E(e)]$ are the forward and backward metrics associated to $s^S(e)$ and $s^E(e)$ respectively, while $\lambda_k[\mathbf{c}(e)]$ is the channel intrinsic information.

LDPC codes are identified by a sparse parity check matrix $\mathbf{H}$, of size $M \times N$. A received codeword must satisfy all the parity checks (rows) of $\mathbf{H}$, i.e. $\mathbf{H} \cdot x' = 0$, where x is the codeword of length N. Different decoding approaches are possible, depending on the graph representation of $\mathbf{H}$: the classical approach defines a bipartite graph with N Variable Nodes (VNs) and M Check Nodes (CNs), and edges between VN_i and CN_j if a nonzero entry is present in column i and row j of $\mathbf{H}$. Layered decoding [13] on the contrary, sees $\mathbf{H}$ as a multipartite graph composed of different layers of parity checks: this scheduling allows to exploit faster convergence thanks to multiple updates of the bit error probabilities within a single iteration.

Calling $\lambda[c]$ the Logarithmic Likelihood Ratio (LLR) of symbol c and, for column k in $\mathbf{H}$, bit LLR $\lambda_k[c]$ is initialized to the corresponding received soft value. These are the VN-to-CN messages. The following operations are executed for all parity constraints l in a given layer, and reiterated up to the desired level of reliability:

$$\Delta\lambda_{lk}[c] = \lambda_k[c] - \Lambda_{lk}^{apr} \quad (6)$$

$$\lambda_k[c] = \Delta\lambda_{lk}[c] + \Lambda_{lk}^{apo} \quad (7)$$

where Λ_{lk}^{apo} is the CN-to-VN message, namely the updated version of Λ_{lk}^{apr}, that is initialized to 0, and stored for the next iteration. Several exact and approximated algorithms have been proposed to calculate Λ_{lk}^{apo}: the most common algorithm used in LDPC decoding is the *Belief Propagation* (BP) algorithm, of which one of the most used approximations is the *min-sum* and its variations [14].

It can be clearly seen that LDPC and turbo decoding processes share many characteristics. Both of them are iterative, rely on soft information, are usually implemented in their logarithmic form, while commonly being represented through special kinds of graphs. A particularly interesting exploitation of these characteristics has been proposed in [15]. Every row of $\mathbf{H}$ is seen as a turbo code with trellis length equal to the row weight: a direct link between turbo and LDPC codes is drawn, and turbo decoding algorithms can be applied to LDPC codes with minor adjustments. The BCJR-based LDPC decoding relies on the fact that binary LDPC codes have a 2-state trellis: state metrics can consequently be expressed as differences $\Delta\alpha[c]$ and $\Delta\beta[c]$, reducing the quantization noise. Defining $\Phi(x, y) = \max(x, y) - \max(x+y, 0)$ and considering the Max-Log-MAP approximation [16], the CN-to-VN message update becomes:

$$\Lambda_{lk}^{apo} = \Phi(\Delta\alpha_k[c], \Delta\beta_k[c]) \quad (8)$$

$$\Delta\alpha_k = \Phi(\Delta\alpha_{k-1}[c], \Delta\lambda_{lk}[c]) \quad (9)$$

$$\Delta\beta_k = \Phi(\Delta\beta_{k+1}[c], \Delta\lambda_{lk}[c]) \quad (10)$$

where $\Delta\alpha[c]$ and $\Delta\beta[c]$ at the edge of the trellis are initialized as the minimum value of the dynamic range.

III. Proposed FEC scheme

In the CCSDS recommended standard [17] transmission data rates of up to 2.048 Mb/s are foreseen for the next missions, while FEC schemes must be able to guarantee bit error floors not higher than 10^{-9}. The need for effective coding schemes, alongside simple decoding algorithms, makes code concatenation one of the smartest solutions. The powerful Turbo and LDPC codes have been considered for concatenation before ([18]) but the low level of details provided and the unsatisfying results leave room for further investigation.

The devised FEC scheme is shown in Fig. 1: an LDPC code is serially concatenated to a turbo code. The outer encoder encodes the input bits, and the resulting codeword is used as input for the inner encoder. Being responsible of the first, rough decoding, the IC should work well also in presence of a large number of errors. Since turbo codes have better performance than LDPC at low SNR [19], they have been chosen as IC. On the contrary, receiving the updated information from the inner decoder, the OC decoder, that is an LDPC code, can fully exploit its deep waterfall region and low error floor. An interleaver scrambles the output of the OC encoder before the second encoding, while the inverse function is inserted between the decoders. Since, depending on the rate and characteristics of the chosen codes, the block sizes may not be compatible, an optional padding block has been placed after the interleaver: zeros are added to the scrambled codeword to fit the required number of bits. This reduces the coding efficiency but allows for flexible concatenation. The padding bits are removed after the IC decoding, before the deinterleaver.

The decoding process starts in the IC decoder, which performs up to Iter_{in} iterations. After Iter_{in} the codeword is stripped of the padding bits, descrambled and passed to the OC decoder. Both turbo and LDPC code decoding algorithms involve soft information: while the IC decoder receives measures of bit error probabilities from the channel estimator, the OC decoder must rely on the metrics updated by the IC decoder. In particular, the LDPC decoder receives as intrinsic information for the initialization of $\lambda_k[c]$ the bit-level extrinsic output of the turbo SISO $\lambda_k[u]$. These metrics are passed through the deinterleaver along with the codeword.

 ISBN: 978-1-61208-264-6

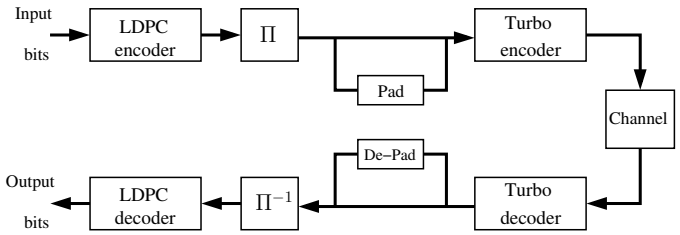

Figure 1: Serial concatenation of LDPC and turbo codes FEC scheme

The CCSDS suggests three FEC schemes for space communications in [1]: a RS-convolutional codes concatenated scheme, turbo codes and LDPC codes. Deep space communications requiring very low bit error rates address turbo codes in particular, allowing four code rates ranging from 1/6 to 1/2, and four information block lengths in the range 1784-8920. The WiMAX standard [19] relies on a wide set of Quasi-Cyclic LDPC codes (QC-LDPC), together with turbo codes of different length and rates. The two code types are mutually exclusive options in the standard: their proven effectiveness and implementation-friendly structure, however, make them ideal candidates for concatenation towards deep-space applications, regardless of the relatively low performance of WiMAX LDPC codes w.r.t. CCSDS LDPC codes. Thanks to the wide variety of available codes, it has been possible to experiment with different code combinations consisting of both WiMAX and CCSDS codes. Though CCSDS Single-Binary (SB) turbo codes employ 16 states, it is proven in Section IV that also the Duo-Binary (DB), eight-state codes used in WiMAX guarantee very good results while keeping the decoding complexity low.

IV. Simulations and performance comparisons

To evaluate the effectiveness of the proposed approach, simulations have been run on a proprietary tool. Its deeply customizable structure allows to select codes, channel model, SNR and result reliability level, together with decoding algorithms and related choices (number of iterations, stopping criteria). Moreover, it is possible to tweak a set of implementation-oriented characteristics, like different approximations of the chosen algorithms and number of bits assigned to the representation of the metrics.

In order to comply as much as possible with the requirements of CCSDS, the turbo codes suggested in [1] have been used as ICs in a first batch of simulations, and concatenated with WiMAX LDPC codes. The relatively high rate of the OC results in a concatenated rate that is very close to the CCSDS specifications. Block size compliance is guaranteed by using, if needed, multiple LDPC codewords as a single turbo information block, together with padding bits. The maximum allowed number of iterations has been set to 10 for both IC and OC decoder, and following most of the state of the art on deep space communications, the AWGN channel model has been chosen.

Moving towards a hardware implementation of the proposed FEC scheme, some limitations have been inserted in the simulation environment. To correctly evaluate the impact of soft information quantization on the BER and FER, the dynamic range of all metrics involved in the decoding process has been limited to 10 or 9 bits, with 3 bits of fractional part. For the same reason, both the LDPC and turbo codes have been decoded with the BCJR algorithm, thus leading to low decoding complexity.

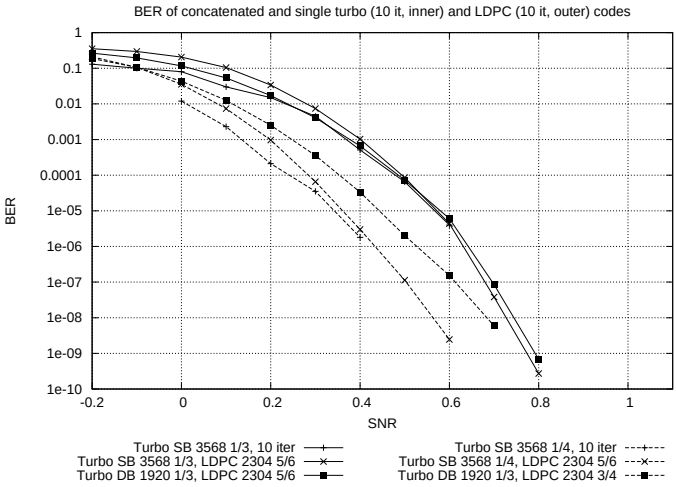

Figure 2: Concatenated LDPC and turbo BER, AWGN channel, BPSK modulation

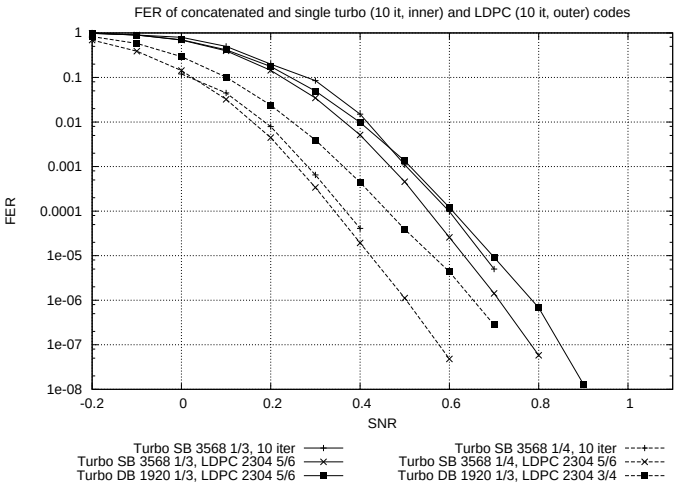

Figure 3: Concatenated LDPC and turbo FER, AWGN channel, BPSK modulation

Early experimentations have shown that the gain that can be obtained with the insertion of a bit interleaver between the two encoders is negligible w. r. t. the additional complexity, and it has not been considered in the plotted curve. This limited effect is mainly due to the sparse structure of the $\mathbf{H}$ matrix, that acts as an interleaver by itself [18].

Fig. 2 and 3 plot a set of meaningful BER and FER curves respectively. The "+" marker indicates the curves provided by CCSDS in [1] for SB turbo codes of rate 1/3 (continuous) and 1/4 (dashed). They are obtained with 10 decoder iterations, QPSK modulation and AWGN channel. The ×-marked curves show the performance of these codes when concatenated with a WiMAX rate 5/6 LDPC code. It can be seen that both

 ISBN: 978-1-61208-264-6

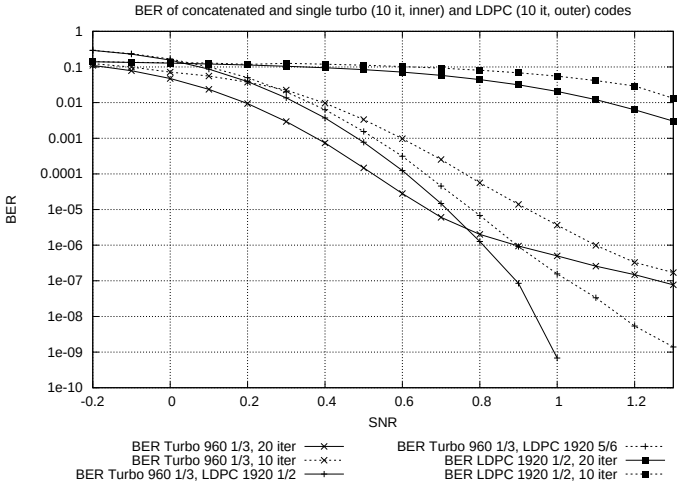

Figure 4: LDPC and DB turbo BER, concatenated and single-code, AWGN channel, BPSK modulation

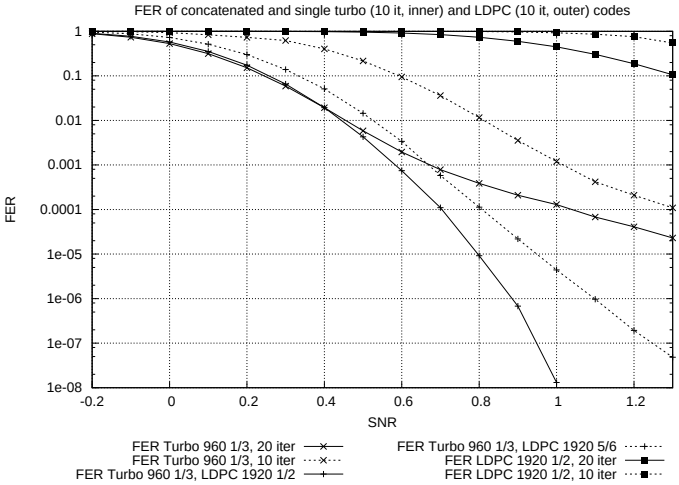

Figure 5: LDPC and DB turbo FER, concatenated and single-code, AWGN channel, BPSK modulation

concatenated BER and FER follow very closely the standard's curves: FER results are particularly encouraging, thanks to aggregated error distributions that are addressed later in this section. Moreover, plots in [1] show error floors as early as BER=10^{-6} (block length 8920): the minimum BER simulated with the concatenated scheme is slightly above 10^{-10}, with no signs of error floor.

The continuous, ■-marked curves have been obtained by substituting to the SB turbo code of CCSDS in the concatenated scheme a WiMAX DB turbo code of comparable size and same rate. The difference between the two curves is negligible, while the complexity of an 8-state turbo decoder is much lower than a 16-state one, as shown in Section V.

To evaluate the influence of IC and OC respective rates on the decoding performance, a second set of simulations has been run: the IC rate has been fixed to 1/3 and by changing the OC rate it has been possible to obtain concatenated rates equal to those of CCSDS turbo codes. In both Fig. 2 and 3, the dashed, ■-marked curve has a concatenated rate of 1/4, obtained by CTC 1/3 + LDPC 3/4. It can be noticed how the lower rate of the OC fails to deliver the same BER and FER results as CTC 1/4 + LDPC 5/6: this behavior, observed also in the CTC 1/6 + LDPC 5/6 against CTC 1/3 + LDPC 1/2 case, reveals how the IC turbo rate is more critical than for the LDPC OC.

Fig. 4 plots a set of BER curves to compare the performance of WiMAX concatenated codes against single LDPC and turbo codes. The curves showing the "+" marker refer to the concatenated FEC scheme: both use a WiMAX turbo code of rate 1/3 and 960 two-bit input symbols. The continuous line has been obtained using a rate 1/2, codeword length 1920 LDPC, while the dashed one with a rate 5/6 LDPC. The higher rate LDPC results in a less steep curve: this degradation can be addressed by rising Iter_{in}, with the two curves superimposed at Iter_{in}=20. These plots are compared to the constituent rate 1/3 CTC and rate 1/2 LDPC with different numbers of allowed iterations. Since the concatenated scheme has at its disposal up to 20 iterations (10 CTC + 10 LDPC), single-code curves are plotted with both 20 and 10 iterations maximum. The concatenated BER shows very good performance at low E_b/N_0, crossing the 10^{-6} threshold at E_b/N_0=0.9 dB when using the rate 5/6 LDPC OC. At higher E_b/N_0, its performances are even more remarkable: a total of $2 \cdot 10^8$ frames have been simulated for all the shown E_b/N_0 points, for a total of $1.92 \cdot 10^{11}$ information bits, and no errors were counted for E_b/N_0 higher than 1.0 dB when using the rate 1/2 LDPC code. The curves show no sign of error floor and constant BER decrease. At low E_b/N_0, the 20-iterations single CTC outperforms the concatenated schemes of up to 0.15 dB: the difference is smaller than that reported in [18] with much more favorable conditions, and the crossing point occurs at a higher BER and much lower E_b/N_0.

Fig. 5 shows the FER curves for the same parameters as Fig. 4: the concatenated FER reaches very low values ($7 \cdot 10^{-8}$ with rate 5/6 LDPC code). The difference with the 20-iteration single CTC curve at low E_b/N_0 is substantially reduced (0.08 dB maximum) w. r. t. the BER, and the crossing point is moved at lower E_b/N_0. This is due to the fact that very often a failed decoding with the concatenated scheme is due to a high number of wrong bits within the same frame. Consequently, BER and FER scale differently, since errors are clustered together and affect a very low number of frames.

Table I provides a comparison of the proposed FEC scheme with similar state of the art solutions. Solution **A** refers to CCSDS SB turbo 1/4 + WiMAX LPDC 5/6, while solution **B** to CCSDS SB turbo 1/3 + WiMAX LPDC 5/6, both already shown in Fig. 2 and Fig.3. To help a fair comparison with coding schemes with different rate, the Δ_{SHN} row identifies the distance of the BER curve from the Shannon limit at BER=10^{-6}: in both cases the distance is less than 1.5 dB. The obtained Δ_{SHN} is similar to that of the AR4JA LDPC codes proposed by CCSDS [1], but has been obtained with a much smaller number of iterations.

In a recent work [20], a FEC scheme for 3D HDTV using an outer block turbo code (BTC) concatenated to an LDPC code is proposed. The scheme is shown to outperform the DVB-

TABLE I. PERFORMANCE COMPARISON AMONG FEC SCHEMES

	A	**B**	[20]	[21]	[5]	[6]	[22]	[18]	[23]
Application	Deep space		3D HDTV	Satellite	Deep space	Deep space	–	Mobile	
Inner Code	SB CTC		LDPC	NB-LDPC	QC-LDPC	LT	Parallel	SB CTC	
Outer Code	QC-LDPC		BTC	LT		NB-LDPC	RSC/LDPC	LDPC	
Rate$_{in}$	1/4	1/3	1/2	2/3	1/3	25/49	1/2	1/3	
Rate$_{out}$	5/6	5/6	467/500	9/10		49/50	1/2	7/8	
Rate$_{concatenated}$	5/24	5/18	467/1000	3/5		1/2	1/3	7/24	
Input$_{in}$	3568		16 K	1000 symbols	2379	32 K	504	2048	
Input$_{out}$	1920		15 K	900 symbols		16 K	504	1792	
Inner Decoding Alg.	BCJR		BP	FFT-BP	BP	N/A	Log-MAP	BP	
Outer Decoding Alg.	BCJR		CHASE	MP			LLR-BP	Log-MAP	
Iter$_{in}$	10		50	20	15	N/A	8	5	5
Iter$_{out}$	10		N/A	N/A			10	50	100
Quantization	10-9 bits		Floating Point	Floating Point	Floating Point	Adaptive	Floating Point	Floating Point	
Channel	AWGN		Rayleigh	AWGN	AWGN	AWGN	AWGN	AWGN	
E_b/N_0 @ BER=10^{-6}	0.43	0.65	4.4	1.85	N/A	N/A	2.35	1.75	1.55
FER @ BER=10^{-6}	$8 \cdot 10^{-6}$	$8 \cdot 10^{-6}$	$4 \cdot 10^{-4}$	N/A			$2 \cdot 10^{-5}$	N/A	N/A
Δ_{SHN} @ BER=10^{-6}	1.38	1.43	4.50	1.55			2.90	2.43	2.23
minimum BER	$2 \cdot 10^{-9}$	$< 10^{-10}$	$2 \cdot 10^{-7}$	$8 \cdot 10^{-7}$	$3 \cdot 10^{-6}$	N/A	$1.2 \cdot 10^{-7}$	$4 \cdot 10^{-7}$	$2 \cdot 10^{-7}$
minimum FER	$6 \cdot 10^{-8}$	$1.1 \cdot 10^{-8}$	$8 \cdot 10^{-5}$	N/A	N/A	10^{-8}	$6 \cdot 10^{-6}$	N/A	N/A
E_b/N_0 @ min	0.6	0.9	4.6	2.0	0.3	1.05	2.5	1.9	1.6

T2 standard serial concatenation of BCH and LDPC codes. Contrariwise to CTCs, BTCs are obtained by concatenating various BCH codes, and decoded via CHASE algorithm, whose implementation complexity is estimated comparable to that of BCJR. The BER and FER performance are greatly outperformed by this work's, with approximately 4 dB gain, and a very high Δ_{SHN}. This could partly be due to the higher code rate and to the fading channel model, but [20] sets a very high number of iterations for the inner code, a large block size and floating point precision for the simulations, all factors that contribute to the improvement of results.

Luby Transform (LT) or fountain codes have been used together with non-binary LDPC (NB-LDPC) codes in [21] for satellite communications. The resulting system is very flexible, thanks to LT codes, and the presence of NB-LDPC codes guarantees a high error correction power even at high rates. The decoding complexity, however, suffers from the concurrent FFT-based BP and message passing algorithms, much higher than a single BCJR. The BER shows 1.2 dB loss w. r. t. solution **B**: for the same rate and precision, the two FEC systems should yield comparable results. This is confirmed by the comparable Δ_{SHN} metrics. Both **A** and **B**, however, outperform the LT+binary LDPC codes of [24].

The QC-LDPC construction scheme for deep space communications described in [5] gives very good results without making use of concatenation: although the curves do not show low BER points, a 0.4 dB gain can be observed against the plots with similar rate in Fig. 2. These curves have been drawn with floating-point precision and a decoding algorithm devoid of approximations: some degradation of performance is consequently to be expected after the implementation. The complexity of the probability-domain BP algorithm, moreover, is very high, burdening the hypothetical hardware with large area occupation and high power consumption.

The joint source-channel coding scheme described in [6], aimed at deep space image transmission, uses Raptor codes, *i. e.* a concatenation of an LT code with a precode, in this case a very high-rate NB-LDPC. This powerful coding scheme, also addressed in [21], obtains very good results at high coding rates: FER shows only 0.15 dB loss w. r. t. solution **B**, regardless of the rate difference.

In [22] parallel concatenation of LDPC and RSC codes is explored. The LLR-based BP algorithm implemented for the LDPC part allows good performance also with relatively small block sizes and a few allowed iterations: still, it is outperformed by **A** by 1.70 dB gain at BER=10^{-6} and one dB smaller Δ_{SHN}, with even more difference in the FER curves.

The two closely related works [18] and [23] implement CTCs as inner and LDPC codes as OCs, decoding them with Log-MAP and probability-domain BP algorithms respectively. The work in [23] presents the same system as [18], with the addition of a certain number of global decoder iterations that slightly improve the BER. The plotted curves show a degradation of the concatenated scheme (5+50 iterations) w. r. t. the single turbo code (5 iterations) of up to 0.3 dB that has not been observed in this work (Fig. 4). Rates are comparable to that of **B**, and they both use the AWGN channel model, while the block size of **B** is larger. Regardless of the much higher precision and number of iterations allowed in [18], **A** and **B** yield better BER and Δ_{SHN} results, with a gain ranging from 0.90 to 1.10 dB at BER=10^{-6}.

V. IMPLEMENTATION COMPLEXITY

The proposed FEC scheme joins the BER of turbo codes at low E_b/N_0 with that of LDPC codes at higher E_b/N_0, resulting in very steep performance curves that are well suited for deep space communications. However, concatenation is usually expensive when it comes to implementation, since decoding is required for both codes separately. Resource sharing can be attempted, but if the decoding algorithms are very different the obtained area saving are often overweighted by the additional logic required. Since LDPC and turbo codes can be decoded with the BCJR algorithm, it is possible to share a large part of the datapath. Currently, the authors

 ISBN: 978-1-61208-264-6

are working on a flexible and efficient decoder meeting the requirements for concatenated LDPC and turbo decoding: the decoder must be able to switch between LDPC and turbo configurations on-the-fly, in case of IC failed decoding. Partial synthesis estimations show that around 95% of the LDPC datapath can be shared with the turbo datapath. Moreover, due to the higher number of states in the trellis of turbo codes, the LDPC decoder architecture can exploit an internal level of parallelism (up to 8× in presence of 16-state turbo codes). This aspect is particularly useful in case many LDPC codewords are used as a single information block for turbo codes. Taking as an example the multi-core LDPC-turbo decoder presented in [9], a 95% shared datapath would result in a 14% area reduction in every processing element. The limited throughput requirements set by CCSDS allow to scale down the operating frequency: in **B**, a throughput of 2 Mb/s would be achieved at 8 MHz, with a huge decrease in power consumption.

BP and CHASE algorithms used in [20] are very different and, to the best of our knowledge, datapath sharing has never been considered. However, the adaptive BP proposed in [25] for BTC decoding is likely to allow at least partial resource sharing. Also in case of LT and NB-LDPC codes used in [21] and [6], while the datapaths are different, both decoding processes rely on a bipartite graph: this can lead to some degree of sharing of the internal connections and memories.

In [22] LDPC decoding is performed through LLR-BP: the min-sum approximation only requires sums and minimum extractions, making its implementation very simple. In [26] resource sharing between min-sum and SISO-based turbo decoding is considered, resulting in unsatisfying improvements: the overhead would be even greater with the probability-domain BP used in [18].

VI. Conclusion and future work

In this paper, a FEC scheme relying on serial concatenation of parallel CTCs and LDPC codes is presented. Detailed simulations and comparison with the state of the art show competitive results, outperforming or being comparable to the latest concatenation and deep space schemes. The use of the same algorithm to decode both codes leads to a small area, low power implementation that is currently under development. Early complexity estimations show that it is possible to implement the proposed approach at a very small cost w. r. t. even single code deep space communications FEC schemes.

References

[1] *TM Synchronization and Channel Coding - Summary of Concept and Rationale*, Consulative Committee for Space Data Systems (CCSDS) Std. 130.1-G-2, Nov. 2012.

[2] *TM Channel Coding Profiles*, Consulative Committee for Space Data Systems (CCSDS) Std. 131.4-M-1, Jul. 2011.

[3] C. Berrou, A. Glavieux, and P. Thitimajshima, "Near Shannon limit error correcting coding and decoding: Turbo codes," in *IEEE International Conference on Comm.*, 1993, pp. 1064–1070.

[4] R. G. Gallager, "Low density parity check codes," *IRE Transactions on Information Theory*, vol. IT-8, no. 1, pp. 21–28, Jan 1962.

[5] N. Andreadou, F.-N. Pavlidou, S. Papaharalabos, and P. Mathiopoulos, "Quasi-cyclic low-density parity-check (QC-LDPC) codes for deep space and high data rate applications," in *Satellite and Space Communications, 2009. IWSSC 2009. International Workshop on*, sept. 2009, pp. 225 –229.

[6] O. Bursalioglu, G. Caire, and D. Divsalar, "Joint source-channel coding for deep space image transmission using rateless codes," in *Information Theory and Applications Workshop (ITA), 2011*, feb. 2011, pp. 1 –10.

[7] Z. Wang and Z. Cui, "Low-complexity high-speed decoder design for Quasi-Cyclic LDPC codes," *Very Large Scale Integration (VLSI) Systems, IEEE Transactions on*, vol. 15, no. 1, pp. 104 –114, jan. 2007.

[8] A. Ahmed, M. Awais, A. ur Rehman, M. Maurizio, and G. Masera, "A high throughput turbo decoder VLSI architecture for 3GPP LTE standard," in *Multitopic Conference (INMIC), 2011 IEEE 14th International*, dec. 2011, pp. 340 –346.

[9] C. Condo, M. Martina, and G. Masera, "VLSI implementation of a multi-mode turbo/LDPC decoder architecture," *Circuits and Systems I, IEEE Transactions on*, to appear.

[10] M. Alles, T. Vogt, and N. Wehn, "FlexiChaP: A reconfigurable ASIP for convolutional, turbo, and LDPC code decoding," in *Turbo Codes and Related Topics, 2008 5th International Symposium on*, 2008, pp. 84 –89.

[11] L. R. Bahl, J. Cocke, F. Jelinek, and J. Raviv, "Optimal decoding of linear codes for minimizing symbol error rate," *IEEE Transactions on Information Theory*, vol. 20, no. 3, pp. 284–287, Mar 1974.

[12] S. Papaharalabos, P. T. Mathiopoulos, G. Masera, and M. Martina, "On optimal and near-optimal turbo decoding using generalized $\max^*$ operator," *IEEE Comm. Letters*, vol. 13, no. 7, pp. 522–524, Jul 2009.

[13] D. Hocevar, "A reduced complexity decoder architecture via layered decoding of LDPC codes," in *Signal Processing Systems, IEEE Workshop on*, 2004, pp. 107 – 112.

[14] M. Fossorier, M. Mihaljevic, and H. Imai, "Reduced complexity iterative decoding of low-density parity check codes based on belief propagation," *IEEE Trans. on Comm.*, vol. 47, no. 5, pp. 673 –680, May 1999.

[15] M. Mansour and N. Shanbhag, "Turbo decoder architectures for low-density parity-check codes," in *Global Telecommunications Conference, 2002. GLOBECOM '02. IEEE*, vol. 2, nov. 2002, pp. 1383 – 1388 vol.2.

[16] M. Martina, G. Masera, S. Papaharalabos, P. T. Mathiopoulos, and F. Gioulekas, "On practical implementation and generalizations of max* operator for turbo and LDPC decoders," *IEEE Transactions on Instrumentation and Measurement*, vol. 61, no. 4, pp. 888–895, Apr 2012.

[17] *Radio Frequency and Modulation Systems Part 1: Earth Stations and Spacecraft*, Consulative Committee for Space Data Systems (CCSDS) Std. 401.0-B-21, Jul. 2011.

[18] S. H. Lee, J. A. Seok, and E. K. Joo, "Serial concatenation of LDPC and turbo code for the next generation mobile communications," in *Wireless and Optical Communications Networks, 2005. WOCN 2005. Second IFIP International Conference on*, march 2005, pp. 425 – 427.

[19] *IEEE Standard for Local and Metropolitan Area Networks Part 16*, IEEE Std 802.16e-2005 Std., 2006.

[20] K. Kwon, H. H. Im, and J. Heo, "An improved FEC system for next generation terrestrial 3D HDTV broadcasting," in *Consumer Electronics (ICCE), 2012 IEEE International Conference on*, jan. 2012, pp. 327 – 328.

[21] W. Lei, L. Jing, and W. J. bo, "Design of concatenation of fountain and non-binary LDPC codes for satellite communications," in *Information Engineering and Computer Science (ICIECS), 2010 2nd International Conference on*, dec. 2010, pp. 1 –4.

[22] S. Gounai, T. Ohtsuki, and T. Kaneko, "Performance of concatenated code with LDPC code and RSC code," in *Communications, 2006. ICC '06. IEEE International Conference on*, vol. 3, june 2006, pp. 1195 – 1199.

[23] S. H. Lee, J. A. Seok, and E. K. Joo, "Serially concatenated LDPC and turbo code with global iteration," in *Systems Engineering, 2005. ICSEng 2005. 18th International Conference on*, aug. 2005, pp. 201 – 204.

[24] W. Yao, L. Chen, H. Li, and H. Xu, "Research on fountain codes in deep space communication," in *Image and Signal Processing, 2008. CISP '08. Congress on*, vol. 2, may 2008, pp. 219 –224.

[25] C. Jego and W. Gross, "Turbo decoding of product codes using adaptive belief propagation," *Communications, IEEE Transactions on*, vol. 57, no. 10, pp. 2864 –2867, october 2009.

[26] J. Dielissen, N. Engin, S. Sawitzki, and K. van Berkel, "Multistandard FEC decoders for wireless devices," *Circuits and Systems II, IEEE Transactions on*, vol. 55, no. 3, pp. 284 –288, march 2008.

 ISBN: 978-1-61208-264-6

Capacity Saving Analysis of L_p-problem based Allocation with Packet Loss and Power Metrics in GEO-Satellite Communications Channels

Igor Bisio, Stefano Delucchi, Fabio Lavagetto, Mario Marchese
DITEN - University of Genoa
Genoa, Italy
Email: igor.bisio, stefano.delucchi, fabio.lavagetto, mario.marchese@unige.it

***Abstract*—This paper introduces a criterion, based on the L_p-problem, which has been employed to allocate capacity among Earth Stations. The obtained allocations permit a performance compromise between Packet Loss and Transmitted Power, which are taken into account as performance metrics. Moreover, starting from the proposed L_p-problem based allocation and considering specific analytical models for the Packet Loss Probability (PLP) and the Transmitted Power (TP), the paper highlights the existence of a Capacity Bound, independent of the overall capacity available C_{TOT}, on which the allocations converge. The main contribution of the paper concerns the performance analysis, carried out by simulation, which shows that the proposed method enables a significant savings of capacity and Transmitted Power and simultaneously, with only a limited worsening of the Packet Loss.**

Keywords-Satellite Communications; Multi-Objective Programming; Lp-problem based Allocation; Capacity Bound; Performance Analysis;

I. INTRODUCTION

Resource allocation in modern satellite networks, such as satellite-sensor [1], LTE [2] and WiMax [3], plays a crucial role and needs to be deeply investigated. In several previous works (such as [4], [5], [6] and [7]), we consider a scenario composed of a satellite communication system of Z earth stations that receive TCP traffic flows from a fixed number of sources and forward them onto a common geostationary satellite channel with an overall available capacity set equal to C_{TOT} [bps]. The channel state is modeled by considering the fading effect, due to atmospheric conditions, that have a negative impact on the quality of communications. As a consequence, to compensate, we apply a Forward Error Correction (FEC) encoding system, selecting the code rate as a function of the fading level F, expressed in [dB], undergone by each station. From the viewpoint of the higher protocol layers (i.e., above the network layer) the redundancy bits added to protect the transmitted information cause a reduction of the available capacity for transmission. Taking into account the proposed scenario, the problem considered in this paper is the well known capacity allocation problem. The goal is to share the channel capacity among the earth stations according to the policy defined in [6] whose performance is further analysed and discussed in this paper. The proposed allocation problem models each transmission entity (i.e., the Earth Stations) using some functions, which values are directly proportional to the capacity allocated, that represent some metrics that need to be optimized simultaneously (e.g., the Packet Loss Probability, shortly PLP, and the Transmitted Power, shortly TP, as done in this work). If the functions are in contrast to each other, as it happens in the case of this paper, the solution of the allocation problem must represent a compromise. For this reason we use the Multi-Objective Programming (MOP) framework to formulate the allocation problem thereby obtaining a solution also known as the Pareto Optimal Point (POP) set. To find out a single solution from this set, which is representative of the best compromise between the adopted metrics, we apply the L_p-*problem*.

An important consequence of the proposed approach is that its solution converges if C_{TOT} increases (i.e., the Capacity Bound (CB) discussed in [6]). It enables a significant capacity savings with respect to the allocation of the overall resources available on the channel: C_{TOT}. In fact, sharing all the channel capacity enables to optimize the value of a decreasing metric, however this is not true for an increasing metric. So it is useless to allocate the whole capacity but a significant portion can be reserved to increase the number of earth stations that can transmit on the satellite channel. It is worth noticing that all the stations, that are allowed to transmit, experience the same conditions in terms of PLP and TP.

The aim of this paper is to present a performance analysis of the allocation problem proposed, by focusing on the evaluation of the benefits obtained, considering the value of the PLP and the TP, with respect to the allocation of the whole available capacity C_{TOT}. Another key point of this paper is the evaluation of the increment of the number of earth stations computed by using a formula of the average number of earth stations, which can transmit with fixed value of PLP and TP, is presented.

As next step of the research presented in this work, adaptive modulation and coding techniques, applied together with the resource allocation, for example based on the DVB-S2 standard as in [8] and [9], will be object of thorough study. The rest of the paper is organized as follows. The next section presents a brief survey of the state of the art of resource allocation for satellite and wireless communications systems. In Section II the model adopted for the capacity

 ISBN: 978-1-61208-264-6

allocation is presented while Section III describes the formulae employed for the Packet Loss Probability (PLP) and Transmitted Power (TP). Section IV presents the simulation results that highlight the advantages obtained allocating a capacity equal to the CB, obtained by using our allocation method with respect to the allocation of the overall available capacity. Finally Conclusions are drawn.

II. The Formulation Allocation Problem

The model adopted in this paper and developed in previous works by same authors ([5] and [6]), is based on three different components. The physical entities represent the earth stations, which are composed by different queues called virtual entities. Each queue is characterized by several objective function that model some performance metrics such as the Packet Loss Probability and the Transmitted Power, as done in this work.

A. The MOP based capacity allocation problem

To formalize the MOP based capacity allocation we define two vectors: the first one, reported in (1) is the control vector and contains all the capacities allocated to each virtual entity for each physical entity considered. Formally we consider that each physical entity is identified by $z \in [1, Z]$. Y_z is the number of virtual entities of the $z-th$ physical entity. Each virtual entity is identified by $y_z \in [1, Y_z]$. M_{y_z} is the number of objective functions for each virtual entity y_z. Each objective function, of a given $y_z - th$ virtual entity, is identified by the index $m \in [1, M_{y_z}]$. C_{y_z} is the capacity allocated to the virtual entity y of the physical entity z

$$\mathbf{C} = (C_{1_1}, C_{2_1}, C_{3_1}, ..., C_{Y_1}, ..., C_{1_Z}, C_{2_Z}, C_{3_Z}, ..., C_{Y_Z}) \tag{1}$$

In this work the capacity allocation is supposed to be carried out in a centralized fashion: the control vector is the output of a centralized decision maker and represents the decision taken by the allocation algorithm, that is the capacity assigned to each queue in each earth station. It is worth noticing that the overall capacity allocated to the $z-th$ physical entity, C_z is the sum of the capacities allocated to all its virtual entities that are $C_z = \sum_{y=1}^{Y_z} C_{y_z}$.

The second vector defined is the so called objective function vector and contains the value of each objective function of each virtual entity in each physical entity. All the components of this vector are the metrics, the PLP and the TP analytically defined in Section III that need to be optimized simultaneously.

$$\begin{aligned}\mathbf{F}(\mathbf{C}) = (&F_{1,1_1}(\mathbf{C}), ... \\ &F_{M_{1_1},1_1}(\mathbf{C}), ..., F_{1,Y_Z}(\mathbf{C}), ..., F_{M_{Y_Z},Y_Z}(\mathbf{C}))\end{aligned} \tag{2}$$

In (2), the generic term $F_{m,y_z}(\mathbf{C})$ is the $m-th$ objective function of the $y-th$ virtual entity of the $z-th$ physical entity. Considering the Multi Objective Programming theory formalized in [5] with the control vector defined in (1) and the objective function vector (2) is possible to formalize the MOP based capacity allocation problem as follows:

$$\begin{cases} \mathbf{C}_{opt} = \Big(C_{1_1,opt}, C_{2_1,opt}, .., C_{Y_1,opt}, .., \\ C_{1_Z,opt}, C_{2_Z,opt}, .., C_{Y_Z,opt}\Big) = \arg\min_{\mathbf{C}} \mathbf{F}(\mathbf{C}); \\ C_{y_z} \geq 0, \forall y_z \in [1, Y_z]. \forall z \in [1, Z] \\ \sum_{z=1}^{Z} \sum_{y=1}^{Y_z} C_{y_z} \leq C_{TOT} \end{cases} \tag{3}$$

An important boundary is imposed in (3): the sum of the capacity allocated to each virtual entity must be lower or equal to the overall capacity available in the channel C_{TOT}. As a consequence the MOP capacity allocation problem determines a feasibility region that contains all the control vector that may be admissible solutions. The goal of this allocation policy is to determine a control vector C_{opt} that simultaneously minimizes all the components of the objective function vector.

The solution of the defined problem is not single but it is a set, called Pareto Optimal Points (POP) set. The position of this set depends on the characteristics of the objective functions considered: if all objective functions are strongly decreasing [10], then a solution $\mathbf{C}_{opt}$ is a POP if and only if the solution is on the constraint boundary $\sum_{z=1}^{Z} \sum_{y=1}^{Y_z} C_{y_z} = C_{TOT}$. If this condition is not true the POP set may also stay also inside the feasibility region which means that the Pareto Optimal may also be a point for which $\sum_{z=1}^{Z} \sum_{y=1}^{Y_z} C_{y_z} < C_{TOT}$.

The strongly decreasing assumption concerning the objective-function vector is quite typical because common performance functions applied in telecommunication networks such as Packet Loss Probability, Packet Delay and Packet Jitter are quantities that decrease their values when the allocated capacity value increases. This is not true if other important metrics are also used: power, but also processing and computation effort. In those cases, as done in this paper considering the PLP as one of the adopted metrics, the allocation of the overall available capacity C_{TOT} may not be the optimal choice. In fact as previously said the optimal solution may also be also inside the feasibility region and not on the constraint boundary. The aim of this paper is to identify a solution through the MOP approach, as well as to compare the performance by way of the results obtained sharing the overall capacity available among the considered earth stations.

B. The L_p-problem based capacity allocation

As previously said, the MOP based capacity allocation problem determines as a solution a set of points. In this

paper we apply the L_p-problem to obtain a single control vector that represents a compromise between the adopted metrics. The idea is to allocate capacity so that the value of each objective function is as close as possible to its ideal value. The set of ideal capacities (i.e. the ideal vector (4)) is composed of the ideal decision variable vector elements $C_{y_z,id}^{F_{k,y_z}}$ for which F_{k,y_z} attains the optimum value

$$\begin{aligned}&\mathbf{C}_{id}^{F_{k,y_z}} = \Big(C_{1_1,id}^{F_{k,y_z}}, C_{2_1,id}^{F_{k,y_z}}, ..., C_{Y_1,id}^{F_{k,y_z}}, ..., \\ &C_{1_Z,id}^{F_{k,y_z}}, C_{2_Z,id}^{F_{k,y_z}}, ..., C_{Y_Z,id}^{F_{k,y_z}}\Big) = \arg\min_{\mathbf{C}} F_{k,y_z}(\mathbf{C}); \\ &\forall k \in [1, M_{y_z}], \forall y_z \in [1, Y_z], \forall z \in [1, Z]\end{aligned} \tag{4}$$

Each element $C_{y_z,id}^{F_{k,y_z}}$ can assume a value between 0 and C_{TOT}, independently of any physical constraint and of the values of the other components of vector (4). It is called ideal (utopian) for this reason. For example, if a generic objective function is decreasing versus the allocated capacity, it is obvious that it is ideal to use all the possible capacity C_{TOT}, while if it is increasing versus capacity, it is ideal allocating no capacity at all. The values of vector (4) are considered known in the remainder of the paper while the vector in (5) contains each objective function attaining its ideal value.

$$\begin{aligned}\mathbf{F}_{id} = \Big(&F_{1,1_1,id}\Big(\mathbf{C}_{id}^{F_{1,1_1}}\Big), .., F_{k,y_z,id}\Big(\mathbf{C}_{id}^{F_{k,y_z}}\Big), .., \\ &F_{M_{Y_Z},Y_Z,id}\Big(\mathbf{C}_{id}^{F_{M_{Y_Z},Y_Z}}\Big)\Big)\end{aligned} \tag{5}$$

To compute the distance to the ideal vector we apply the generic norm p and in (6) and in (7) is reported the formulation of the L_p-problem based capacity allocation (L_pCA)

$$\begin{aligned}&\mathbf{C}_{all} = (C_{1_1,all}, C_{2_1,all}, ..., C_{Y_1,all}, ..., C_{1_Z,all}, C_{2_Z,all}, ..., \\ &C_{Y_Z,all}) = \arg\min_{\mathbf{C}\subset\mathbf{C}_{opt}} J_p(\mathbf{C})\end{aligned} \tag{6}$$

where $J_p(\mathbf{C})$ is a function representing the generic norm, usually indicated with the symbol L_p [10]:

$$\begin{aligned}J_p(\mathbf{C}) = \Bigg(&\sum_{z=1}^{Z}\sum_{y=1}^{Y_z}\sum_{k=1}^{M_{yz}} w_{k,y_z}\Big|F_{k,y_z}(\mathbf{C}^{F_{k,y_z}})+ \\ &- F_{k,y_z,id}\Big(\mathbf{C}_{id}^{F_{k,y_z}}\Big)\Big|^p\Bigg)^{1/p}\end{aligned} \tag{7}$$

and $\sum_{k=1}^{M_{yz}} w_{k,y_z} = 1$, $w_{k,y_z} > 0, \forall k \in [1, M_{y_z}]$, $\forall y_z \in [1, Y_z], \forall z \in [1, Z]$ so to assure the Pareto optimality of the solution. Modifying the values of the weights it is possible to differentiate the importance of the considered objective functions. As a consequence, the proposed capacity allocation is elastic and can be applied to different scenarios with heterogeneous traffic flow with different QoS requirements (e.g., telephony, video-conferencing, audio/video streaming, web transactions).
The most interesting contribution of this work, that is a consequence of the allocation method proposed, concerns a comprehensive analysis of the performance assured by the existence of a Capacity Bound, that has been demonstrated in [6]. This point represents a Pareto Optimal Point (POP) on which the L_pCA problem converges. It implies that, from the practical viewpoint, a Satellite Service Provider may provide capacity allocations to all the entities involved in the allocation process without employing the overall available capacity. It allows dedicating the rest of the capacity to further possible entities. As shown in Section IV, moreover, it can be done without penalizing the overall performance and without capacity wasting.

III. The Objective Functions

In this paper each physical entity represents an Earth Station that transmits through a satellite channel and is composed by a single queue (as a consequence, physical and virtual entities are not differentiated). Each considered entity is represented by two objective functions that are the Packet Loss Probability, shortly PLP, due to congestion ($F_{1,1_z} = P_{loss_z}(C_z)$) and the Transmitted Power, shortly TP, ($F_{2,1_z} = W_{tx_z}(C_z)$) and the constrain is defined by the amount of available capacity ($\sum_{z=1}^{Z}\sum_{y=1}^{Y_z} C_{y_z} \leq C_{TOT}$).

A. Packet Loss Probability Function

The PLP model used in this paper is referred to the loss due to congestion for a Transmission Control Protocol (TCP) based traffic flow and is analytically reported in (8):

$$P_{loss_z}(C_z) = \frac{k_z \cdot N_z^2}{(\frac{R_z \cdot C_z \cdot rtt_z}{l} + Q_z)^2} \tag{8}$$

It is worth noticing that the PLP model adopted in this work is a decreasing function with respect to the allocated capacity C_z. Moreover in this paper, the values of the parameters reported in (8), applied in the performance analysis section, and the related meanings are: k_z=128/81 is a constant depending on TCP protocol, N_z =10 is the number of active TCP connection for the *z-th* station, Q_z is the buffer size, equal to 10 packets, for the *z-th* station. rtt is the round trip time, equal to 512 [ms], l =1500 [byte] is the TCP packet size and R_z and C_z are the code rate and the capacity allocated to the *z-th* station, respectively. Channel conditions vary over the time and, in this paper, the undergone fading level F_z for each station represents the satellite channel status. Each Earth Station is supposed to apply different code rates in dependence on the channel status modeled considering the fading level. Code rates are assigned as in Table I. This hypothesis allows considering packet losses due to congestion because channel errors are made negligible by

TABLE I: APPLIED CODE RATES

F_z $[dB]$	0.0 - 1.0	1.0 - 2.0	2.0 - 3.0	3.0 - 4.0	4.0 - 5.0
R_z	7/8	5/6	3/4	2/3	1/2

applying encoding. On the other hand, as previously said, from the application layer view point, represents a reduction in the available capacity for the considered station. So the detriment of the channel conditions due to the fading effect is modeled by a reduction of the capacity available to a station with respect to the portion allocated as reported in equation (8) where the applied code rate is the capacity reduction factor.

B. Transmitted Power Function

The TP of the *z-th* station is reported in (9):

$$TP_z(h_z, C_z) = (2^{\frac{C_z}{W}} - 1) \cdot \frac{1}{h_z} \tag{9}$$

Considering the formulation of the TP is possible to view that it is an increasing function with respect to the allocated capacity C_z. h_z, called link constant in this paper, takes into account the parameters related to the satellite link. In more detail, it contains the transmission antenna gain G_{T_z} of the *z-th* station, the receiver antenna gain on the satellite G_R (common for each station) both equal to 10^4, the Boltzman constant *k* equal to $1.38{\cdot}10^{-23} J{\cdot}K^{-1}$, the noise temperature *T* set to 290 [K] (considering additive white Gaussian noise), the bandwidth of the satellite channel *W*=1 [MHz] and the Free Space Loss (*FSL*) set equal to 10^{19} as defined in [11]. In practice, the coefficient $\frac{1}{h_z}$ is:

$$\frac{1}{h_z} = \frac{k \cdot T \cdot W \cdot FSL}{G_{T_z} \cdot G_R} \tag{10}$$

The Transmitted Power function is obtained by combining two equations: $C_z = B \cdot log_2\left(1 + \left(\frac{C}{N}\right)_z\right)$ the Hartley-Shannon law, and $\left(\frac{C}{N}\right)_z = \frac{G_{T_z} \cdot G_R \cdot TP_z}{k \cdot T \cdot B \cdot FSL}$ that represents the carrier to noise ratio [11].
It is worth noticing that the employment of equation (9) as transmitted power function implies the hypothesis that the transmission bit rate of the $z-th$ station is equal to the allocated capacity C_z. Both the objective functions considered in this paper are continuous and differentiable in $\mathbb{R}$ so assuring the existence of a solution of the L_p-problem applied.

C. The Capacity Bound

In this paper we consider Z physical entities, a single virtual entity for each physical entity ($Y_z = 1 \, \forall z \in [1, Z]$) and two objective functions for each virtual entity ($k = 2 \, \forall y_z \in [1, Y_z], \forall z \in [1, Z]$). Considering the two objective functions previously introduced, the vector $\mathbf{F}(\mathbf{C})$, defined in (2) it is possible to define a capacity bound where our allocation converges. In practice, given fixed channel conditions, if the overall capacity available for the entire communications system significantly grows, the POP solution provided by solving (3), considering $J_p(\mathbf{C})$ as defined in (7), will not significantly change tending, in the sense of a horizontal asymptote, to a quantity called Capacity Bound C^{bound}. From a formal viewpoint,

$$C^{bound} = \sum_{z=1}^{Z} C_z^{bound}, C^{bound} < C_{TOT} \tag{11}$$

where C_z^{bound} is the portion of capacity allocated to the $z-th$ Earth Station when the overall allocation converges on the defined bound. The mentioned C^{bound} exists and is finished if $C_z^{bound} \; \forall z \in [1, Z]$ is a quantity independent of C_{TOT} when C_{TOT} tends to infinity. [6] defines three conditions, regarding the objective functions used, that assure the existence of the capacity bound. Moreover it demonstrates also that the proposed L_pCA, with the considered metrics, satisfies these conditions.

IV. PERFORMANCE ANALYSIS

The scenario considered in this performance evaluation has been implemented through the *ns-2* simulator. It is composed by $Z = 2$ Earth Stations that transmit TCP traffic over a common geostationary satellite channel. The overall duration of the simulation is 300 [s]. The allocation is done each 5 [s] (i.e., allocation period) and the Fading Level suffered by each $z-th$ station, expressed by F_z, assumes values, kept constant in each allocation period, that belong to Table I. It is worth noticing that F_z is not included in (10) because the fading is supposed to be compensated applying the FEC encoding. As a consequence the terms F_z does not modify the value of TP, which depends only on the *FSL*.
The main contribution of this section is the investigation of the advantages of the proposed L_pCA approach in terms of saved capacity, which are strictly related to the existence of the Capacity Bound. In more detail, the performed tests consider the two earth stations with a random fading level considered uniformly distributed among all possible levels and the code rate is consequently chosen according to the aforementioned table. Obviously, the fading level value is considered known when the allocation algorithm acts. Each value of the performance metrics reported in the figures below represents the average of the values obtained by a number of simulation runs aimed at guaranteeing a confidence interval of the 95%.
The Transmitted Power [W] (TP) values, reported in the following figures, are computed through the objective function (9) itself on the basis of the allocated capacity C_z; the packet loss has been computed, for each allocation period, as the number of packets lost for congestion over the number of sent packets, measured through

 ISBN: 978-1-61208-264-6

the available *ns-2* simulation counters. For this reason, in the following, the results are presented in terms of Packet Loss Rate (PLR). Five weighs configurations are applied to give more, or less, importance to an objective function with respect to the other for both the stations ($z = 1$ and $z = 2$): $w_{1,1_z}$=0.1 and $w_{2,1_z}$=0.9; $w_{1,1_z}$=0.25 and $w_{2,1_z}$=0.75; $w_{1,1_z}$=0.5 and $w_{2,1_z}$=0.5; $w_{1,1_z}$=0.75 and $w_{2,1_z}$=0.25; $w_{1,1_z}$=0.9 and $w_{2,1_z}$=0.1.

The practical purpose of this section is to explicitly evaluate the ratio between the obtained capacity allocations and the related performance with L_pCA, which operates at the C^{bound} value, and the reference case in which the overall capacity C_{TOT} is employed.

To reach the aim, we define the quantity, C_z^{ref}, for the $z-th$ station, which represents the capacity allocated to the $z-th$ station according to its channel condition, applying the L_PCA and imposing that the overall capacity is used, in practice $\sum_{z=1}^{Z} C_z^{ref} = C_{TOT}$. Similarly, the quantity $PLR_z(C_z^{ref})$ and $TP_z(C_z^{ref})$ are, respectively, the Packet Loss Rate and the Transmitted Power of the $z-th$ station obtained allocating to it C_z^{ref}.

In this work we define the *Capacity Saving Ratio* (C_{SR}) as the quantity reported in (12), which is the percentage of the capacity saved using C^{bound} (i.e., to employ C_z^{bound} for the $z-th$ station), with respect to the overall capacity available, C_{TOT} (i.e., to employ C_z^{ref} for the $z-th$ station):

$$C_{SR} = \frac{\left| C^{bound} - C_{TOT} \right| \cdot 100}{C_{TOT}} \quad (12)$$

In the same way, we define the *Transmitted Power Saving Ratio* (TP_{SR}) as the percentage of the average TP saved with respect to the TP obtained sharing the overall available capacity: (13).

$$TP_{SR} = \frac{\left| \sum_{z=1}^{Z} \left(TP_z(C_z^{bound}) - TP_z(C_z^{ref}) \right) \right| \cdot 100}{\sum_{z=1}^{Z} TP_z(C_z^{ref})} \quad (13)$$

Similarly, the *Packet Loss Rate Increasing Ratio* (PLR_{IR}) is defined as the percentage of PLR increase obtained allocating C_z^{bound} to the $z-th$ Station with respect to the PLR obtained allocating the overall capacity among the station:

$$PLR_{IR} = \frac{\left| \sum_{z=1}^{Z} \left(PLR_z(C_z^{bound}) - PLR_z(C_z^{ref}) \right) \right| \cdot 100}{\sum_{z=1}^{Z} PLR_z(C_z^{ref})} \quad (14)$$

The defined metrics are reported in figures 1, 2 and 3. In all cases, the advantage of the L_pCA employment is clear and very satisfactory.

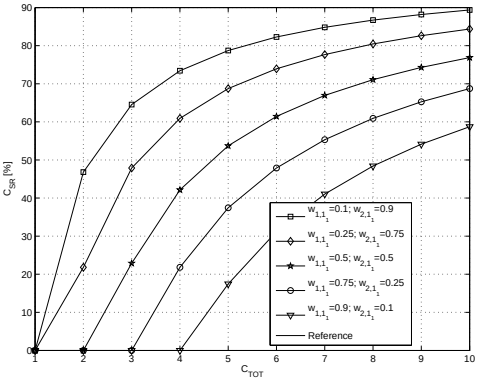

Figure 1: Capacity Saving Ratio using L_pCA.

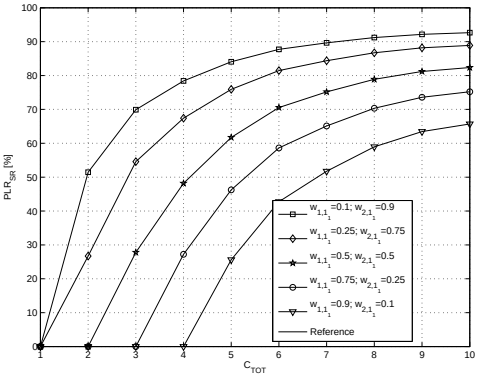

Figure 2: Packet Loss Rate Increasing Ratio using L_pCA.

A further consequence of the capacity saving obtained with the L_pCA is the possibility to serve other stations with the same channel, without the necessity of increase the C_{TOT} and, simultaneously, without a degradation of the performance in terms of PLR and TP. Obviously, the number of stations depends on their channel condition but it is possible to compute the average number as we define in the following:

$$N(C_{TOT}, C^{bound}, Z) = \left\lfloor (C_{TOT} - C^{bound}) \cdot \frac{Z}{C^{bound}} \right\rfloor \quad (15)$$

where Z are the Earth Stations that transmit traffic over the satellite link, and N is the number of Earth Stations that can be served with the same channel. In equation (15) the average increase of Earth Station number N is calculated as the inferior integer part of the product between the capacity saving obtained applying the L_pCA given by ($C_{TOT} - C^{bound}$) and the inverse of the average capacity allocated to a single station (i.e., $\frac{Z}{C_{TOT}}$). Obviously, this quantity increases if the overall capacity (C_{TOT}) increases or if the allocated capacity (C^{bound}) decreases.

In Figure 4 is reported the average increase of the number of Earth Stations $N(C_{TOT}, C^{bound}, Z)$ that can transmit on

the satellite channel. In this case Z is set equal to 2, C_{TOT} varies in the range $[1-10]Mbps$.

V. CONCLUSIONS

The work extends the capacity allocation method proposed in [5] modeled as the MOP problem. In particular, a criterion based on the L_p-problem is proposed to find out a capacity allocation, among Earth Stations, representative of a compromise if Packet Loss Probability (PLP) and Transmitted Power (TP) are taken into account as performance metrics. Moreover, applying the proposed L_p-problem based allocation and considering PLP and TP analytically modeled as in Section III, the obtained allocations converge on a Capacity Bound. This bound is independent of the overall capacity available C_{TOT}. The performance analysis shows that the proposed method enables a significant capacity and TP saving and, simultaneously, a limited worsening of the packet losses. From the practical viewpoint, the paper contribution implies that a Service Provider may provide capacity allocations to Z Earth Stations without employing its overall available capacity and may dedicate the rest of it to other possible entities without penalizing the overall performance and avoiding capacity wasting.

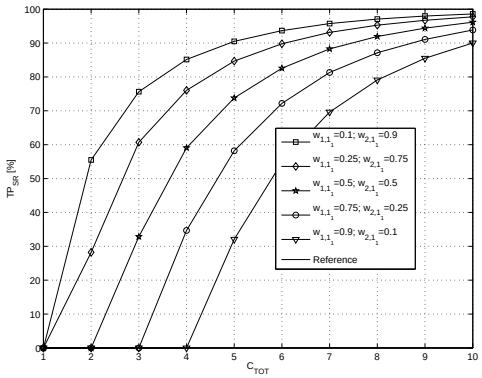

Figure 3: Transmitted Power Saving Ratio using L_pCA.

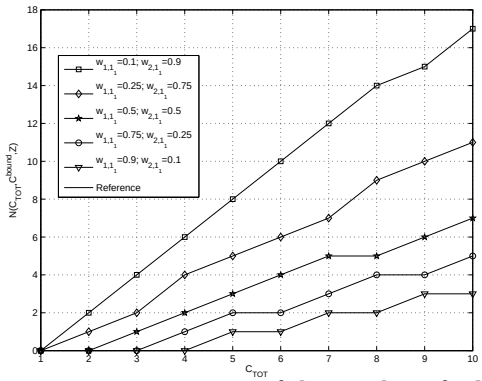

Figure 4: Average increasing of the number of Allowed Earth Station using L_pCA.

REFERENCES

[1] N. Celandroni, E. Ferro, A. Gotta, G. Oligeri, C. Roseti, M. Luglio, I. Bisio, M. Cello, F. Davoli, A. D. Panagopoulos, M. Poulakis, S. Vassaki, T. De Cola, M. A. Marchitti, Y. F. Hu, P. Pillai, S. Verma, K. Xu, and G. Acar, "A survey of architectures and scenarios in satellite-based wireless sensor networks: system design aspects", International Journal of Satellite Communications and Networking, vol. 31, no. 1, 2013, pp. 1-38. [Online]. Available: http://dx.doi.org/10.1002/sat.1019

[2] M. Amadeo, G. Araniti, A. Iera, and A. Molinaro, "A Satellite-LTE Network with Delay-Tolerant Capabilities: Design and Performance Evaluation," IEEE Vehicular Technology Conference (VTC Fall), 2011, pp. 1-5.

[3] G. Araniti, M. Condoluci, A. Molinaro, and S. Pizzi, "Radio-Aware Subgroups Formation for Multicast Traffic Delivery in WiMAX Networks," IEEE 23rd International Symposium on Personal, Indoor and Mobile Radio Communications (PIMRC), September 2012, pp. 477-482.

[4] K.-D. Lee, "An efficient real-time method for improving intrinsic delay of capacity allocation in interactive geo satellite networks", Vehicular Technology, IEEE Transactions on, vol. 53, no. 2, March 2004, pp. 538-546.

[5] I. Bisio and M. Marchese, "Power saving bandwidth allocation over geo satellite networks", Communications Letters, IEEE, vol. 16, no. 5, May 2012, pp. 596-599.

[6] I. Bisio, S. Delucchi, F. Lavagetto, and M. Marchese, "Capacity bound of mop-based allocation with packet loss and power metrics in satellite communications systems", in IEEE Global Communications Conference, 2012. GC 12, Dec. 2012, p. to appear.

[7] I. Bisio, S. Delucchi, F. Lavagetto, and M. Marchese, "Comparison among Resource Allocation Methods with Packet Loss and Power Metrics in Geostationary Satellite Scenarios", in IEEE International Conference on Communications, 2013. ICC 13, Jun. 2013, p. to appear.

[8] S. Mukherjee, M. De Sanctis, T. Rossi, E. Cianca, M. Ruggieri, R. Prasad, "Mode Switching Algorithms for DVB-S2 Links in W Band", in IEEE Global Communications Conference, 2010. GC 10, 6-10 December, 2010.

[9] S. Mukherjee, M. De Sanctis, T. Rossi, E. Cianca, M. Ruggieri, R. Prasad, "On the Optimization of DVB-S2 Links in EHF Bands", IEEE Aerospace Conference 2010, Big Sky (Montana), March 2010, pp. 1-11.

[10] K. M. Miettinen, "Nonlinear Multiobjective Optimization", Boston, USA: Kluwer Academic Publisher, 1998.

[11] L. J. Ippolito, "Satellite Communications System Engineering", Chichester, UK: John Wiley & Sons Ltd, 2008.

 ISBN: 978-1-61208-264-6

New Optical Communication Capabilities Using Nanosatellites

F. Sansone, L. Olivieri, A. Francesconi
Centre of Studies and Activities for Space CISAS "G. Colombo"
University of Padova
Padova, Italy
francesco.sansone@studenti.unipd.it, lorenzo.olivieri@studenti.unipd.it, alessandro.francesconi@unipd.it

***Abstract*—In this paper, the benefits derived from the exploitation of nanosatellites for complex telecommunication missions are presented, along with their limitations, and laser technology is identified as a viable solution to dramatically increase the downlink and crosslink capabilities of such miniature platforms. Then, the critical technological issues concerning the integration of an optical telecom terminal on a nanosatellite platform are discussed, considering the perspective advancements in areas such as power generation, propulsion and attitude control. The incompatibility of laser terminals pointing requirements with the current and perspective nanosatellite attitude stability has been identified as the most critical issue to be addressed in order to implement optical links on nanosatellites. A possible solution is presented at the end of the discussion.**

Keywords-nanosatellite; optical link

I. INTRODUCTION

The term *nanosatellite* refers to the class of satellites weighting between 1 and 10 kg, which were initially conceived to offer students and young engineers valuable educational experiences with real flight programs; their exploitation was boosted by the introduction of the CubeSat standard in 2003. The interest showed by space agencies and academic institutions in such miniature platforms is constantly increasing because of their inherent advantages. The reduced mass, prototyping and production time of nanosatellites, as well as low launch cost as piggyback payloads allow universities, corporations and small companies to access to space easily. As of December 2012, 149 missions based on nanosatellites were flown and many others are on schedule [1], [2].

The inherent low cost of a single nanosatellite can be further reduced when mass production of standard units is applied, making these miniature platforms particularly appealing for the realization of satellite constellations suitable for earth observation, mapping or telecommunication applications. In particular, LEO telecom constellations based on nanosatellites could be attractive since they can provide global continuous coverage, overcoming the visibility limitations of large GEO platforms, and can be cost-effective even with respect to the existing LEO systems. The integration of high data rate, compact telecommunication terminals on nanosatellite platforms could pave the way to mission scenarios unexpected to this day.

In this work, three illustrative perspective scenarios have been identified and are briefly presented below.

1) *Extension of GEO satellites coverage to polar areas and urban canyons*. A LEO constellation of nanosatellites providing continuous coverage over polar regions can be used as a bridge to extend the coverage of GEO telecom satellites (see Fig. 1a), which is usually limited to the ±71° latitudinal band when a minimum elevation angle of 10° is considered. Also, the system can be used to better cover densely urbanized areas. This way, the capabilities of GEO satellites can be increased at a very low relative cost.
2) *Data relay constellation for scientific satellites in LEO*. Scientific missions in LEO produce a large amount of data, while few, short windows are available for downlink to ground stations. A constellation of miniature platforms capable of high data rate down/crosslinks providing continuous global coverage will make it possible to download data to ground stations not visible to the scientific satellites, almost in real time, as shown in Fig. 1b.
3) *Low cost constellation for situational awareness*. In case of unavailability of ground infrastructures due to natural or man-made disasters, situational awareness can be maintained exploiting a LEO nanosatellite constellation, as depicted in Fig. 1c. Crosslink capabilities could dramatically reduce the access time to any point of the Earth surface.

However, the advantages given by the exploitation of nanosatellites are counterbalanced by severe technical limitations, which make them unattractive for complex or high performance missions. Such limitations are represented by the short life (few years) and the limited on-board resources in terms of power and volume available to the payload, attitude control and telecommunications. In particular, downlink and crosslink capabilities are limited by both the on-board power and the poor attitude stabilization typical of nanosatellites, which often rely only on permanent magnet bars and hysteresis rods, preventing the exploitation of narrow-beam antennas for high data rate links. Typically, nanosatellite communication systems use the VHF or UHF frequency band, and are based on monopole or microstrip patch antennas, with wide beamwidth and data rate often bounded to a few tens of kbit/s. Sometimes the S band is

 ISBN: 978-1-61208-264-6

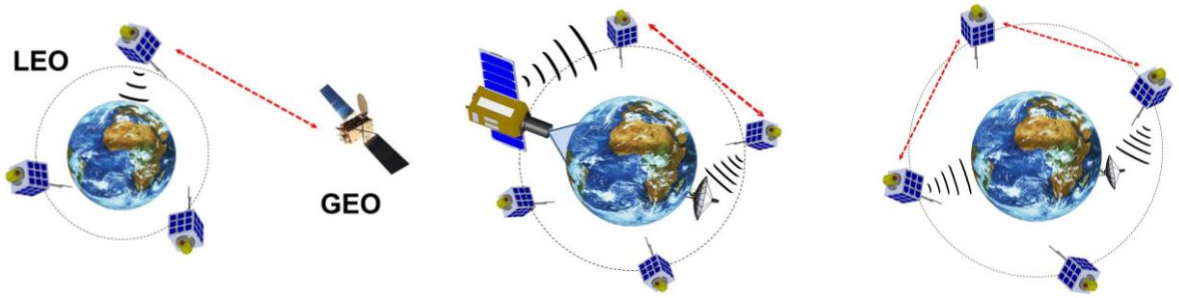

(a) (b) (c)

Figure 1. Illustrative new mission scenarios: (a) extension of GEO satellites coverage to polar areas and urban canyons, (b) data relay constellation for scientific satellites in LEO, (c) low cost constellation for situational awarness.

exploited for higher data rate. This is the case of the Generic Nanosatellite Bus [3], whose dual communication system uses a UHF monopole antenna receiver system for uplink at 4 kbps and an S-band transmitter patch antenna set for downlink, capable of data rates between 32 kbps to 256 kbps.

In this paper, the advantages of exploiting optical links on nanosat platforms are discussed in section II. The state of the art of the main technologies required for the realization of the aforementioned mission scenarios is summarized in section III, along with the perspective advancements in those fields. Finally, section IV presents the system that is developed by the authors to cope with the current technological limitations which these days prevent the integration of laser communication terminals onboard nanosatellites.

II. CREATING NEW COMMUNICATION CAPABILITIES USING NANOSATELLITES

In this section, the benefits derived by the exploitation of optical link devices onboard nanosatellites are discussed.

Telecom systems based on laser technology are characterized by very narrow beamwidth and high frequency carriers (hundreds of THz), which make it possible to obtain very high data rate transmissions with more compact and less power consuming devices, with respect to RF systems. In addition, optical links can provide secure channels, as they are immune to jamming and cannot be intercepted. Moreover, there are no licence regulations on the use of optical frequency bands and bandwidths, so great commercial opportunities are possible. Although it cannot be considered a standard technology yet, several optical link devices were developed and tested in the last years [4]-[6]; among them, examples of compact devices are represented by STRV-2 [7] and SOTA [8].

As an example, two RF and one laser-based communication systems for high data rate links are compared in order to determine which technical solution is more suitable for integration on nanosatellites class platforms. The carriers of the two RF systems are set to 2.5 and 20 GHz respectively, the former representing the state of the art of RF communication systems for miniature satellites and the latter representing perspective advancements in this field [9]. The selected laser wavelength is 1.55 μm. A LEO – LEO crosslink scenario is considered with an intersatellite distance of 5000 km and the link requirements are expressed in terms of desired data rate and BER, which are set to 500 Mbit/s and 1E-6 respectively. The former is set roughly 3 orders of magnitude greater than typical maximum data rates for nanosatellites. Then, in order to compare systems with equivalent performance, the RF and optical terminals design assumptions, such as antenna diameter and bandwidth, are set in order to provide the same link margin. For simplicity, the emitter and receiver terminals are supposed to be identical. After that, the link budget is assessed, leading to the estimation of the required power and system mass for all the considered solutions. As regards the optical system, the total mass and power consumption are estimated using empirical correlations between these parameters and the telescope aperture, which were derived from a literature survey on existing optical link devices. The estimates account also for the mechanical active pointing system. On the other hand, the antenna and transmitter mass, as well as the transmitter input power for the RF systems have been estimated considering the relations provided by [10]. An additional mass of at least 1 kg is added to account for the antenna steering mechanism, derived from a literature survey of analogous systems [11]-[12]. Table 1 summarizes the terminals design assumptions and presents the results given by the link budget calculation and the total mass and power consumption estimation; the total mass of the RF systems is given by the sum of the antenna, transmitter and steering mechanism masses. The pointing accuracy required by each system was also calculated according to [13] and is reported in the last line of Table 1.

The results point out that the laser-based system requires a much lower power input with respect to the RF systems and its mass is considerably lower. In fact, the total estimated masses of the RF terminals exceed the nanosat standard limits. However, the pointing accuracy needed to achieve the communication requirements is much more

 ISBN: 978-1-61208-264-6

TABLE I. RESULTS FROM THE LINK BUDGET FOR A RF SYSTEM AND A LASER-BASED TERMINAL PROVIDING A LINK WITH DATA RATE OF 500 MBIT/S, BER OF 10^{-6} AND SAME LINK MARGIN

DESIGN ASSUMPTIONS				
	Unit	**RF 1**	**RF 2**	**Optical**
Antenna diameter	[m]	0.3	0.3	0.02
Carrier frequency	[GHz]	2.5	20	193.5E3
Wavelength	[m]	0.120	0.015	1.55E-6
Bandwidth	[MHz]	500	500	500
Modulation	[/]	BPSK	BPSK	BPSK
RESULTS				
	Unit	**RF 1**	**RF 2**	**Optical**
Trx gain	[dB]	15.31	33.37	91.34
EIRP	[dB]	54.97	54.97	76.71
Trx power	[W]	>1000	144.62	0.035
E_b/N_0	[dB]	12.00	12.00	12.00
Link margin	[dB]	1.30	1.30	1.30
Beamwidth	[rad]	0.49	0.06	96E-6
Total mass	[kg]	>100	15	3.5
Total power	[W]	>1000	395	20
Pointing accuracy	[rad]	0.020	0.003	4E-6

stringent for the optical system, as a consequence of the very narrow beamwidth.

III. TECHNOLOGICAL GAPS

In this section the main technological issues that must be addressed to enable the exploitation of nanosatellite platforms for optical communication are briefly discussed.

A. Miniaturized Optical Link Terminal

The mass of existing laser-based communication terminals for space applications ranges between 5 and 160 kg, while their power consumption is within 28 and 150 W. The main drivers for sizing an optical terminal are the telescope aperture and the laser output power, which together contribute to the transmission gain. With the recent availability of compact, reliable and more powerful laser diodes the telescope dimensions can be reduced while maintaining a high transmission gain, thus enabling the realization of low-mass terminals. An optical communication system for microsatellite platforms, with preliminary mass, power consumption and data rate assessment of 5 kg, 45 W and 2.5 Gbit/s respectively, is currently under development [14]; therefore, it is expected that in the near future terminals suitable for integration on nanosatellite platforms can be realized with current technology.

B. Power Generation

An estimated power consumption of 20 W for the miniaturized laser terminal results from the analysis performed in section II. According to [15], so far the average available power on-board nanosatellite platforms does not exceed 10 W, even when GaAs solar cells are used. The limiting factor is essentially the small area available to solar cells, even when deployable solar arrays are exploited. A promising solution to this issue is represented by rollable solar arrays based on thin polymide foils, which are characterized by a very high specific power generation (>200 W/kg) [16], [17]. A total power consumption of 60 W can be delivered by a deployable, thin film solar array of 0.4 m^2, for a total weight of only a few hundred grams. Thus, it seems that power available on nanosatellite platforms will increase dramatically in the next years.

C. Propulsion

Considering a mission scenario in which a nanosatellite constellation is exploited for telecommunication, propulsion capabilities are essential for orbit maintenance and correction. In high LEO (1000 km or more), the most significant long-term semi-major axis perturbation is due to solar radiation pressure, as the Earth atmosphere density is almost negligible; for a 10 kg platform, a total ΔV of 50 m/s is estimated for orbit corrections throughout a 5 years mission. It seems that such performance can be achieved using currently available technology, as promising results were obtained in the last years exploiting pulsed plasma thrusters and field emission electric propulsion systems [18], [19].

D. Pointing Accuracy and Stability

As pointed out in section II, lasercom devices require very stringent pointing accuracy and stability as a consequence of their narrow beamwidth. The needed pointing accuracy is at least in the order of a ten microradians. To this date, this requirement is far beyond the capabilities of any kind of attitude control system considering both nanosatellites and larger platforms. In addition, the bus attitude stability is critical to establish an optical connection between two spacecraft. As a reference point, the ADCS of the Generic Nanosatellite Bus for the BRITE mission [20], which is scheduled to launch in 2013, will be capable of unprecedented performance for nanosatellites, with attitude accuracy and stability of <1° and 60'' respectively, exploiting a miniature startracker for fine attitude determination and a set of nano reaction wheels. Such performance do not meet the aforementioned requirements, so it is clear that they can be achieved only with a dedicated pointing system. However, moving gimbals could generate additional disturbances the bus ADCS must deal with, which sums to the vibrations generated by large deployable solar arrays based on thin polymide films. At best, considering a nanosatellite platform provided with 3-axis attitude control and damping system, the residual vibrational environment of the bus in LEO is characterized by a few milliradians amplitude oscillations at low frequency (<5 Hz).

In summary, in the near future the capabilities of nanosatellites are expected to increase significantly as power generation and propulsion are concerned; in addition, recent advancements in laser technology will enable the realization of miniaturized optical terminals for

 ISBN: 978-1-61208-264-6

telecommunications. However, both the state of the art of ADCS and the expected advancements in this area seem insufficient to meet the attitude stability requirements needed for a steerable laser communication terminal.

IV. CONCLUSIONS AND FUTURE WORK

The exploitation of LEO constellations based on nanosatellites for telecommunication scenarios is attractive for the benefits derived from the low mass, production time and overall cost of such miniature platforms. However, the exploitation of nanosatellites for complex missions is still prevented by their current severe resources limitations. In this paper, optical communication has been identified as a viable solution to increase significantly the communication data rate available to payloads onboard nanosatellites. The technological aspects which play a key role in the realization of new mission scenarios have been discussed considering the current state of the art of nanosatellite technologies and their perspective advancements in the near future. Considering the actual limitations of ADCS of nanosatellites, the laser terminal pointing accuracy and stability have been identified as the most critical issues which must be addressed to enable the exploitation of optical telecom terminals onboard nanosatellite platforms.

In this framework, the exploitation of a miniaturized, actively stabilized platform as an interface between the optical terminal and the host spacecraft is the chosen solution to cope with the current nanosats ACDS limitations. The active rejection of both low and high frequency vibrations from the bus to the laser terminal and viceversa not only will enable the exploitation of optical links on miniature satellites, but it will also allow to relax the requirements on both the ADCS of the host spacecraft and the pointing mechanism of the optical terminal. The authors are currently developing an integrated system composed by a miniaturized laser communication terminal and an actively controlled ultra-stable parallel platform with 3 rotational dof (shown in Fig. 2). This system is conceived to be mounted on top of a nanosatellite bus with 3-axis attitude control based on standard technologies (3 reaction wheels and 3 torquerods), but provided with sufficient power generation capabilities to sustain the optical communication terminal. The system performance will be evaluated though laboratory test using an attitude simulator testbed.

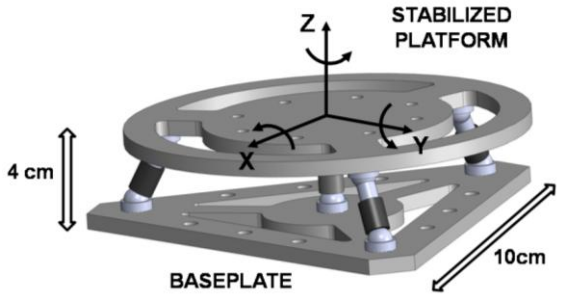

Figure 2. Preliminary configuration of the actively-stabilized platform.

REFERENCES

[1] http://www.slideshare.net/mpariente/nanosatellite-industry-overview - retrieved: February 2013

[2] http://en.wikipedia.org/wiki/List_of_CubeSats - retrieved: February 2013

[3] F. M. Pranajaya and R. E. Zee, "Generic nanosatellite bus for responsive mission," Proc. 5th Responsive Space Conference, Loa Angeles, CA, USA, April 2007, pp. 134-140

[4] G. Griseri, "SILEX pointing acquisition and tracking: ground test and flight performances," Proc.4th ESA International Conference on Spacecraft Guidance, Navigation and Control nn Systems, Noordwijk, The Netherlands, 18–21 October 1999, pp. 467-472

[5] Y. Fujiwara et al., "Optical inter-orbit communications engineering test satellite (OICETS)," Acta Astronautica 61, 2007, pp. 163 – 175

[6] G. Baister, P. Gatenby, J. Lewis, and M. Witting, "The SOUT optical intersatellite communication terminal," IEE Proc on Optoelectronics, , Vol. 141 No. 6, December 1994, pp. 345-355

[7] A. Biswas, G.Williams, K. E. Wilson, H. Hakakha, R. Steiger, and E. J. Korevaar, "Results of the STRV-2 lasercom terminal evaluation tests," Proc. SPIE Free-Space Laser Communication Technologies X, Vol. 3266, January 1998, 2-13, San Jose, California, USA

[8] Y. Koyama et al., "SOTA: small optical transponder for micro-satellite," IEEE Int. Conf. on Space Optical Systems and Applications, Santa Monica, CA, USA, May 2011, pp. 97-101

[9] J. A. King, J. Ness, G. Bonin, M. Brett, and D. Faber, "Nanosat Ka-band communications - a paradigm shift in small satellite data throughput," Proc. 26th Annual AIAA/USU Conference on Small Satellites, Logan, Utah, USA, August 2012

[10] J. R. Wertz and W. J. Larson, "Space Mission Analysis and Design," Microcosm Press and Kulver Academic Publishers, 1999

[11] http://www.astrium.eads.net/en/equipment/antenna-pointing-mechanism-electronics-apme.html - retrieved: February 2013

[12] SSTL Antenna Pointing Mechanism Sales Brochure, July 2012

[13] V. W. S. Chan, "Optical satellite networks," J. Lightwave Technol. 21, NO. 11, November 2003, pp. 2811-2827

[14] T. Dreischer, B. Thieme, M. Bacher, K. Buchheim, and P. Hyvönen, "OPTEL-μ: a compact system for optical downlinks from LEO satellites," Proc. 12th International Conf. on Space Operations, Stockholm, June 2012

[15] J. Bouwmeester and J. Guo, "Survey of worldwide pico- and nanosatellite missions, distributions and subsystem technology," Acta Astronautica 67, December 2010, pp. 854 – 862

[16] K. Otte, L. Makhova, A. Braun, and I. Konovalov, "Flexible Cu(In,Ga)Se_2 thin-film solar cells for space application," Thin Solid Films 511 –512, July 2006, pp. 613-622

[17] R. Barrett et al., "Development of a passively deployed roll-out solar array," AIAA Journal, 2006, 21(12), pp. 4011-4023.

[18] C. Scharlemann et al., "Propulsion for nanosatellites," Proc. 32nd International Electric Propulsion Conference, Wiesbaden, Germany, September 2011, pp. 11–15

[19] P. Shaw, "Pulsed plasma thrusters for small satellites," doctoral thesis, University of Surrey, June 2011

[20] K. A. Carroll, S. Rucinski, and R. E. Zee, "Arc-minute nanosatellite attitude control: enabling technology for the BRITE stellar photometry mission," Proc. 18th Annual AIAA/USU Conference on Small Satellites, Logan, Utah, USA, August 2004, SSC04-V-2

 ISBN: 978-1-61208-264-6

Toward Self-Reconfiguration of Switched Ethernet Architectures in the Next Generation of Space Launchers

Jérémy Robert[1,2], Jean-Philippe Georges[1,2], Thierry Divoux[1,2]
[1]Université de Lorraine, CRAN, UMR 7039, Campus Sciences - BP 70239,
F-54506 Vandœuvre-lès-Nancy, France
[2]CNRS, CRAN, UMR7039, France
Email: firstname.name@univ-lorraine.fr

***Abstract*—Nowadays, many embedded systems use specific data buses (like CAN in vehicles or MIL-STD-1553B in launchers) to ensure the exchange of data. To reduce the cost, the mass and to increase performance, a solution is to rely on a components off-the-shelf (COTS) technology. As switched Ethernet is a well-known solution and widely implemented, this technology is studied for the next generation of space launchers. In this paper, we focus on the reliability issue. In case of network components failure and without reconfiguration mechanism, the network will not carry on control data anymore. Performance of Ethernet reconfiguration solutions may be not enough efficient regarding real-time constraints. This paper aims hence at coping with real-time guarantees of self reconfiguration for Ethernet networks, especially in the space launchers. An experimental evaluation has been leaded on a real case study during a Centre National d'Etudes Spatiales (CNES) French Research & Technology (R&T) activity.**

Keywords- fault-tolerant network; industrial Ethernet; real-time.

I. INTRODUCTION

Nowadays, many embedded systems (aircrafts, satellites, launchers) use several specific data buses which ensure the exchange of either the control data or the service data (measurement or supervision). Particularly, the Ariane 5 launchers use a MIL-STD-1553B data bus [1] to transport the control data while the telemetry data flow is managed by a dedicated (and proprietary) bus. The MIL-STD-1553B bus relies on a centralized communication scheme inherent to its command/response mechanism. As illustrated in Fig. 1, the duplex architecture was seen as a way to ensure reliability (this choice was not derived inherently from system requirements). In this architecture, the bus and the end-nodes are therefore redundant. When a failure occurs on the bus (or a bus segment), the control of the launcher is based only on the redundant sensors data (not concerned by the failure). As a consequence, the communication system is tolerant to a single failure.

Currently, there are many new objectives for the next generation of space launchers [2]:

- reduction of the total cost of the launch system,
- avionics mass reduction and
- avionics performance improvement (keeping at least the same reliability)

To meet these objectives, there is an attempt to rely on an unique components off-the-shelf (COTS) technology. In this context, the different networks could be unified in a single communication system which will support more and more traffics or even large data (such as images, videos or extended telemetry data). As a consequence, the bus MIL-STD-1553B become unsuitable (due to its low bandwidth).

Among several COTS networks, switched Ethernet is the most cost and mature effective solution [3]. Indeed, this technology is a well-known standard and widely implemented in several domains [4] such as manufacturing systems, automotive [5], transport, aviation [6], motion control [7]. As in all industrial area, it reclaims real-time and reliability requirements, such that the network must fulfill with Quality of Service (QoS) criteria like end-to-end delays, jitter, losses and availability. Several works have dealt with the temporal requirements of switched Ethernet architectures [8], [9], [10]. From this temporal aspect, the feasibility of switched Ethernet architecture (depicted in Fig. 2) in the next generation of space launchers has been highlighted in [11]. The purpose of this paper is to increase the robustness of switched Ethernet architectures up to (at least) the same reliability level than with MIL-STD-1553B.

As in all systems, the reliability in a switched Ethernet architecture can be increased with redundancy. This one can be classified into two categories (see IEC SC65C WG15 and [12]): "redundancy in the network" or "redundancy in the nodes". The first one suggests to extend the network topology with redundant links (and even switches): end stations are attached to a single switch only, and hence interconnected to a single network. In the second one, the nodes have on the contrary (at least) two ethernet cards connected to two (parallel) redundant Ethernet networks.

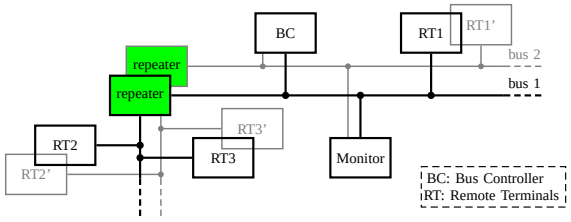

Figure 1. Overview of current MIL-STD-1553B architecture

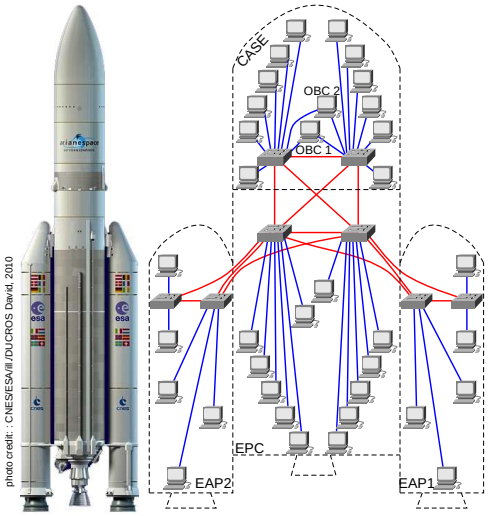

Figure 2. Physical meshed architecture

In reality, MIL-STD-1553B solution is based on a duplex architecture. However, it could lead to cost increase and all messages sent by all end nodes on the bus concerned by failure are still lost (the application was based only on the redundant sensors data). As introduced in [12], we suggest to refer to a "redundancy in the network" solution in which the network can reconfigure itself to ensure the continuity of service. It may be noticed that Automatic Repeat reQuest (ARQ) protocols can improve the reliability, but regarding the real-time requirement, none are considered here. To face with a failure of the local interconnection point of a device, redundancy of the end nodes will be used. Our objectives are therefore to have a reconfiguration mechanism transparent for the application point of view, and to minimize the time of the reconfiguration action (and so the losses). It corresponds to a real-time requirement for the reconfiguration strategy [13], and will be qualified in the following as:

THE RECOVERY TIME: *the time necessary to switch to a backup solution and ensure the continuity of service. An application can tolerate a limited time of interruption of service, called grace time [14].*

To minimize the recovery time, the literature reports many solutions [15] which rely on redundancy management. Redundancy is here supported by a physical meshed architecture. Relevant protocols in this category, Media Redundancy Protocol (MRP) [14] and Rapid Spanning-Tree Protocol (RSTP) [16] are based on two main steps: fault detection and topology reconfiguration. Fault detection is typically achieved by the asynchronous periodic transmission of particular frames between switches. Recovery time issues for real-time systems are coming from these exchanges and from the asynchronism due to the distribution of the algorithm. In order to reduce the recovery time, MRP protocol considers a centralized approach, but only for a ring topology. For all these reasons, this paper will suggest a novel centralized approach for the physical topology supervision and the logical topology reconfiguration. Another feature is that it can be applied in any physical meshed topology.

The remainder of the paper continues as follows: the section II presents an overview of our proposition and describes formally the proposal. Section III illustrates the proposed method by its application to a real case study obtained in the framework of a "CNES french R&T activity" and highlights the performance of our solution. Finally, in section IV some conclusions and future work are given.

II. Research Proposal: Autonomic Switched Ethernet Reconfiguration

The objective of the paper is to suggest a fast recovery solution enabling to ensure fast recovery time in harsh environment. In the framework of CNES activities, this paper deals primarily with space applications in which typical expected QoS criteria are : 1 ms end-to-end delays, any loss of frames, no current requirements in terms of bandwidth (note that in the future, it could be the case, e.g., for the telemetry traffic). This solution is particularly proposed for any meshed switched topologies.

A. Proposition overview

The core idea of our proposition is to reject the logical trees to control all paths in a deterministic way. It is suggested to apply a layer 2 routing to control the "route" taken by each flow. This consists of filling in the forwarding table a priori. Indeed, this table acts as a filter which enables the switch to match an incoming frame to an appropriate MAC-destination address entry and forward the frame to the next hop (with a specific output port) towards the final destination as specified in this table.

Let us remember that the objective of our proposition is that the network could reconfigure itself when a failure occurs. As a consequence, the network should be able to detect a failure and modify (or more exactly reconfigure) the forwarding table to restore an active (and known) path. To achieve this, we suggest to introduce a central agent capable of detecting any failure and reconfiguring an active logical topology. This agent has a global view of the network (and so of the network state). This view can be obtained by requesting all switches periodically (*via* Simple Network Management Protocol - SNMP). Indeed, any switches store the states of its ports in a specific database called Management Information Base (MIB). This information is updated thanks to a physical link integrity function (defined in the standard 802.3) on any switches.

Therefore, from the global view of the network, the central agent can detect a link or a switch failure. In case of link failure, the port state (concerned by the failure) is modified (from "up" to "down" state). When a switch failure occurs, the switch is not reachable anymore (no response to the periodic request).

 ISBN: 978-1-61208-264-6

Once a failure detected, the central agent sends a reconfiguration message in order to modify a (or many) output port(s) in the forwarding table. Although exchanges induced by this reconfiguration mechanism will lead to an over-consumption of the network capacity, it will remain highly limited compared to a capacity of $100\ Mb/s$ and to the current amount of traffic (around $500\ Kb/s$) for Ariane 5 launcher. It leads to a set of new paths between two nodes. As in RSTP, paths will be computed along a spanning-tree. In this proposition, paths with unsuitable end-to-end delays will be rejected [11]. In fact, paths will be computed by a routing algorithm such as Dijkstra's algorithm or Bellman-Ford algorithm. To maintain a deterministic control, they will be computed off-line before the configuration of the network, i.e. in the design phase. The number of paths will be related to the number of flows and to the reliability (e.g. for a single recovery, at least two times the number of flows, but in reality less).

The next subsection presents in a formal way, the reconfiguration algorithm which will be implemented in the central agent. It is planed that hardware implementation issues will be dealt with as well as the distribution of this functionality for facing with this central point of failure.

B. Formal considerations

In a formal way, we consider a network graph $G = (X, A)$ where X is the matrix containing the state of all switch ports and A the matrix representing the physical connectivity between the switches. Let n the number of switches in the architecture and m the number of ports that a switch has (in this paper, it is assumed that all switches have the same number of ports). The element of X is written as $X_{i,j} \in \{0, 1\}$ which represents the state of switch $j \in \{1, n\}$ port i with $i \in \{1, m\}$. X is defined such as $X = [X_1 \dots X_j \dots X_n]$ where X_j represents the port states of switch j. The element of A is noted as $A_{(i,j),(i',j')} \in \{0, 1\}$ represents the physical capacity to communicate between the port i of the switch j and the port i' of switch j'. This network graph will have to be updated periodically as written in line 3 of Algorithm 1. Indeed, in monitoring the states of ports (the matrix X), the network graph is accordingly modified. It is important to note that the performance of our solution will depend on the value of this monitoring period. This criterion will be evaluated in the next section.

Let us remember that our goal is to fill in or update the forwarding table. For that, we have to look for the output ports associated to each destination on all switches. A list D of all stations (represented by their MAC addresses ($@MAC$)) is defined. It is necessary to know on which port of which switch are located the end-stations. A matrix D' is thereby defined to contain the network attachment of the different stations such as $D'_{i,j} \in D$ represents the connection of end stations (with MAC address $@MAC$) on the port i of switch j. As a matter of course, for each switch and for each

Data: $G = (X, A_{(i,j),(i',j')})$: the network graph;
D : the list of all stations;
D' : the network attachment of the different stations;
Result: the vector $R_j =< @MAC, i >$ with $@MAC$ the destination and i the output port to reach $@MAC$ (next hop) from the switch j

```
1 begin
2     Periodically
3         G ⟵ update(G);
4         foreach switch j do
5             foreach @MAC ∈ D do
6                 (i,j') | D'_{i,j'} = @MAC ;
7                 R_j ⟵ Bellman-Ford(j → j', G);
```

Algorithm 1: Reconfiguration algorithm

MAC address in the list D, we can identify on which switch j' is located an end-station (see lines 4-6 in Algorithm 1).

This information and the updated network graph are the inputs of the well-known Bellman-Ford routing algorithm (see line 7 in Algorithm 1). The result of this step is the next hop to reach the destination. Knowing the switch to cross and the physical connectivity (the matrix A), we can deduce the output port to fill in the forwarding table. Of course, if it is concerned by the failure, it is modified (see lines 8-9 in Algorithm 1) in the forwarding table.

III. Experimental Work

Our research laboratory collaborates closely with the CNES to lead R&T activities. In this framework, the objective is to reach a certain level maturity of switched Ethernet technology for the future Ariane launchers. This level can be assessed by the Technology Readiness Level (TRL) [17]. In this work, the TRL 3 is expected and consists to study separately each elements (and problem area) of the technology. It should constitute a "proof-of-concept" without being in an operational environment. As a consequence, a computer network is used to show the feasibility of our algorithm, the reachable interruption time of service and the impact of our algorithm on the number of lost frames. However, a real applicative traffic is considered to perform the laboratory tests and to measure parameters of interest.

The tested architecture is depicted on the Fig. 3. It corresponds to the upper stages (Cryogenic Upper Stage - CASE - and Cryogenic Propulsion stage - EPC - as shown in Fig. 2). In this experiments, the switches are Cisco 2950 series (IOS version: 12.1(22)EA1). In a formal way, this example can be initially described by the matrix X, A, D' and the vector D as can be seen in (1) and (2).

$$X = \begin{pmatrix} 1 & 1 & 1 & 1 \\ 0 & 0 & 0 & 0 \\ \cdot & \cdot & \cdot & \cdot \\ \cdot & \cdot & \cdot & \cdot \\ 0 & 0 & 0 & 0 \\ 1 & 1 & 1 & 1 \\ 1 & 1 & 1 & 1 \\ 1 & 1 & 1 & 1 \end{pmatrix} D = \begin{pmatrix} @MAC1 \\ @MAC2 \\ @MAC3 \\ @MAC4 \\ @MAC5 \\ @MAC6 \\ @MAC7 \\ @MAC8 \\ @MAC9 \\ @MAC10 \\ @MAC11 \\ @MAC12 \\ @MAC13 \end{pmatrix} D' = \begin{pmatrix} @MAC1 & 0 & @MAC8 & 0 \\ @MAC2 & 0 & @MAC9 & 0 \\ @MAC3 & 0 & @MAC10 & 0 \\ @MAC4 & 0 & @MAC11 & 0 \\ @MAC5 & 0 & @MAC12 & 0 \\ @MAC6 & 0 & @MAC13 & 0 \\ @MAC7 & 0 & 0 & 0 \\ 0 & 0 & 0 & 0 \\ \cdot & \cdot & \cdot & \cdot \\ \cdot & \cdot & \cdot & \cdot \\ 0 & 0 & 0 & 0 \end{pmatrix} \quad (1)$$

$$dim(X) = 24 \times 4,\ dim(D) = 13 \times 1\ and\ dim(D') = 24 \times 4$$

$$A = \begin{array}{c} \\ (1,1) \\ \vdots \\ (22,1) \\ (23,1) \\ (24,1) \\ \vdots \\ (22,2) \\ (23,2) \\ (24,2) \\ \vdots \\ (22,3) \\ (23,3) \\ (24,3) \\ \vdots \\ (22,4) \\ (23,4) \\ (24,4) \end{array} \begin{array}{c} \begin{array}{cccccccccccccccccccc} (1,1) & \dots & (22,1) & (23,1) & (24,1) & \dots & (22,2) & (23,2) & (24,2) & \dots & (22,3) & (23,3) & (24,3) & \dots & (22,4) & (23,4) & (24,4) \end{array} \\ \begin{pmatrix} 0 & \dots & 0 & 0 & 0 & \dots & 0 & 0 & 0 & \dots & 0 & 0 & 0 & \dots & 0 & 0 & 0 \\ \vdots & & \vdots & \vdots & \vdots & & \vdots & \vdots & \vdots & & \vdots & \vdots & \vdots & & \vdots & \vdots & \vdots \\ 0 & \dots & 0 & 0 & 0 & \dots & 1 & 0 & 0 & \dots & 0 & 0 & 0 & \dots & 0 & 0 & 0 \\ 0 & \dots & 0 & 0 & 0 & \dots & 0 & 0 & 0 & \dots & 0 & 0 & 0 & \dots & 0 & 1 & 0 \\ 0 & \dots & 0 & 0 & 0 & \dots & 0 & 0 & 0 & \dots & 0 & 0 & 1 & \dots & 0 & 0 & 0 \\ \vdots & & \vdots & \vdots & \vdots & & \vdots & \vdots & \vdots & & \vdots & \vdots & \vdots & & \vdots & \vdots & \vdots \\ 0 & \dots & 1 & 0 & 0 & \dots & 0 & 0 & 0 & \dots & 0 & 0 & 0 & \dots & 0 & 0 & 0 \\ 0 & \dots & 0 & 0 & 0 & \dots & 0 & 0 & 0 & \dots & 0 & 1 & 0 & \dots & 0 & 0 & 0 \\ 0 & \dots & 0 & 0 & 0 & \dots & 0 & 0 & 0 & \dots & 0 & 0 & 0 & \dots & 0 & 0 & 1 \\ \vdots & & \vdots & \vdots & \vdots & & \vdots & \vdots & \vdots & & \vdots & \vdots & \vdots & & \vdots & \vdots & \vdots \\ 0 & \dots & 0 & 0 & 0 & \dots & 0 & 0 & 0 & \dots & 0 & 0 & 0 & \dots & 1 & 0 & 0 \\ 0 & \dots & 0 & 0 & 0 & \dots & 0 & 1 & 0 & \dots & 0 & 0 & 0 & \dots & 0 & 0 & 0 \\ 0 & \dots & 0 & 0 & 1 & \dots & 0 & 0 & 0 & \dots & 0 & 0 & 0 & \dots & 0 & 0 & 0 \\ \vdots & & \vdots & \vdots & \vdots & & \vdots & \vdots & \vdots & & \vdots & \vdots & \vdots & & \vdots & \vdots & \vdots \\ 0 & \dots & 0 & 0 & 0 & \dots & 0 & 0 & 0 & \dots & 1 & 0 & 0 & \dots & 0 & 0 & 0 \\ 0 & \dots & 0 & 1 & 0 & \dots & 0 & 0 & 0 & \dots & 0 & 0 & 0 & \dots & 0 & 0 & 0 \\ 0 & \dots & 0 & 0 & 0 & \dots & 0 & 0 & 1 & \dots & 0 & 0 & 0 & \dots & 0 & 0 & 0 \end{pmatrix} \end{array} \quad (2)$$

In this real scenario, the centralized communication mode is considered: all traffic flows are sent to the destination device 1. The features of these flows are described in the Table I. Each Ethernet frames are stamped and numbered. These two information enable to determine the delay and the inter-arrival time. A failure is simulated by unplugging a network cable at a random time. The application packet loss involves an inter-arrival time superior to the inter-arrival time without loss. It corresponds therefore to a service interruption time (time of non-reception of application frames).

Before considering all traffic flows, a periodic traffic (with a period equals to 1 ms and a size to 72 $bytes$) sent by device 9 to device 1 has been studied. A failure has been simulated on the link connected to the port 24 on the switch $Sw3$. The interruption time has therefore been measured according to a Monte-Carlo scenario (10 first experiments, to be continued) for several monitoring periods: 100 μs, 1 ms, 10 ms and 100 ms. The obtained results are depicted in the Fig. 4.

The Fig. 4 shows that for any period (100 μs, 1 ms, 10 ms and 100 ms), the interruption time is around 200 ms. The variation of the interruption time can be explained by the detection time of "link_loss" which is between 50 ms and 150 ms (defined in the standard 802.3 [18]), plus the reconfiguration time and the update time in the MIB. Among the tested monitoring period, the 100 ms period is the closest to the detection time. That's why, it can be considered a period equals to 100 ms. Moreover, when the frame with the forwarding update is sent, we record this date. We can therefore deduce a (bounded) approximation of the reconfiguration time which is the difference between the end of interruption of service and this date. The reconfiguration time is around 20 ms.

A second test has been leaded on three of the flows which are the flow 1 on the device 13, the flow 2 on the device 9 and the flow 3 on the device 8. These flows are interesting because of their different periods (288 ms, 72 ms and 18 ms). The objective is to highlight the impact of our algorithm on the number of lost frames. The same failure as previously (on the link Sw1-Sw3) is considered. The forwarding table of the switch $Sw3$ is initially configured as shown in Table II.

Consider, for instance, the flows of the device 13 (to device 1) and the link Sw1-Sw3 failure. As the graph is updated periodically (see lines 2-3 of Algorithm 1), the failure will be observed in the matrix X (once the failure is electrically detected *via* the physical link integrity test in the switch and reported in his MIB) as can be seen in 3.

$$X = \begin{pmatrix} 1 & 1 & 1 & 1 \\ 0 & 0 & 0 & 0 \\ \vdots & \vdots & \vdots & \vdots \\ 0 & 0 & 0 & 0 \\ 1 & 1 & 1 & 1 \\ 1 & 1 & 1 & 1 \\ 0 & 1 & 0 & 1 \end{pmatrix} \quad (3)$$

The algorithm calculates (or more precisely it has been offline precalculated as mentioned in II.B) the next hop (the new output port to reach the destination, i.e. device 1 in this example). If we apply the algorithm on this example, for the third switch and the device 1 (which is the destination of the flows of the device 13) with MAC address @MAC1 (lines 4-5 in Algorithm 1), we obtain:

line 6: (i,j') = (1,1)

line 7: the Bellman-Ford algorithm calculate the next hop to reach the switch j'=1 from the switch $j = 3$ according to the current graph G. The Bellman-Ford will have the choice between the ports 23, 24 as next hop because the matrix

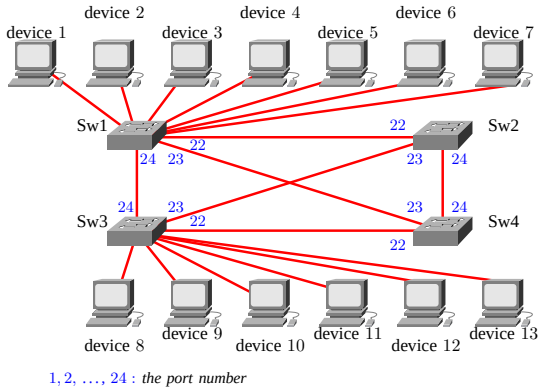

Figure 3. Architecture of case study

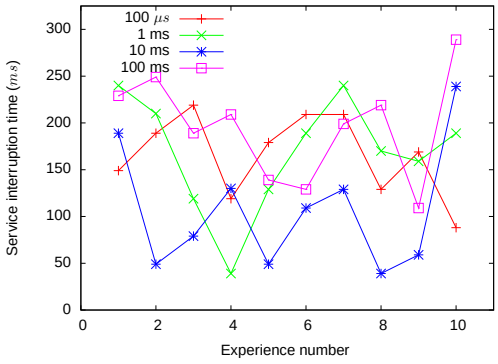

Figure 4. Service interruption time

TABLE I. EXPERIMENTAL TRAFFICS (BYTES, MS)

Device	Flow 1		Flow 2		Flow 3		Flow 4		Flow 5	
	length	period	length	period	length	period	length	period	length	period
2	72	12996	72	12996	-	-	-	-	-	-
3	72	288	72	72	72	144	72	144	72	1152
4	72	1152	72	1152	80	1152	72	1152	80	72
5	72	1152	94	72	72	12996	36	72	-	-
6	72	1620	72	1152	72	1152	72	1552	-	-
7	72	288	-	-	-	-	-	-	-	-
8	72	288	72	288	72	18	72	18	-	-
9	72	72	72	72	-	-	-	-	-	-
10	72	1152	72	1152	72	1152	72	1152	-	-
11	72	72	72	36	-	-	-	-	-	-
12	72	1152	72	72	72	72	72	36	72	1152
13	72	288	-	-	-	-	-	-	-	-

A gives the possible output ports according to the physical connectivity (i.e. ports {22,23,24}) and the matrix X gives the output ports states (i.e. port 21 = 0 so "up", port 23 = 1 so "up" and port 24 = 0 so "down"). Consider the following Bellman-Ford result: next hop = 23. As a result, the vector R_j equals to <@MAC1, 24> (before the failure) is updated to <@MAC1, 23>.

Consequently, the forwarding table of the switch $Sw3$ will be therefore modified as shown in Table III (the parameter $dot1dStaticAllowedToGoTo$ corresponding to the output port becomes 0x00 00 02 (i.e. the port 23). Notice that the forwarding table of the switch $Sw1$ will be also modified (by the algorithm) such a way that the messages of the devices $8, 9, \ldots, 13$ are sent on the output port 22. Moreover, in this example, any modifications will be done on the switch $Sw2$ because its forwarding table is initially configured to send the messages from the devices $8, 9, \ldots, 13$ to the devices $1, 2, \ldots, 7$ *via* the output port 22, and the messages from the devices $1, 2, \ldots, 7$ to the devices $8, 9, \ldots, 13$ *via* the output port 23 (which is the initial Bellman-Ford result).

Table IV shows the number of lost frames in the case of Sw1-Sw3 failure (the cable Sw1-Sw3 is unplugged) by using our solution (measures) or RSTP (the interruption time for RSTP has been considered as being of $1\ s$ [15] for computing the losses). Any flows sent by the devices 2, 3, ..., 8 are lost. Indeed, the failure does not occur on their paths. For the other flows sent by the devices 9, 10, ... 13, the number of lost frames depends on the period of the flow and the interruption time. It is therefore possible to see that there is no loss for all flows with a period of $288\ ms$ (vs. 4 by using RSTP). Only two frames have been lost for the flows with a period of $72\ ms$ (vs. 14 by using RSTP). In the case of flows with a period of $18\ ms$, 14 frames are lost (vs. 56 by using RSTP). However, in the worst case, it could be observed 1 (respectively 3 and 15) loss(es) for the flows with a period of $288\ ms$ (respectively $72\ ms$ and $18\ ms$).

Fig. 5 and 6 show the evolution of the end to end delays. When a failure occurs, the reconfiguration involves a longest path (because the shortest path relatively to the number of hops had been set first). Consequently, the delay increases when the reconfiguration is effective as shown in the two graphs. In this example, the delay growth is equivalent to the switch latency (around only one transmission time because of switching mode: store & forward). However, this growth is proportionally limited (relatively to the service interruption time). Let us note that the zoom on each graph enables to estimate (and retrieve as presented in Table IV) the losses in regard to the interruption time due to the failure.

IV. CONCLUSION AND FUTURE WORK

This paper suggests a novel centralized approach for the physical (meshed) topology and the logical topology reconfiguration. Experimental measurements have shown that the the recovery time has been decreased and the number of losses is lower compared to RSTP (although it is still non-null especially for the flow with a small period).

Finally, the future work will integrate this solution on

TABLE II. INITIAL FORWARDING TABLE OF THE SWITCH SW3

dot1dStatic-Address	*dot1dStatic-ReceivePort*	*dot1dStatic-AllowedToGoTo*	*dot1dStatic-Status*
@MAC1	0	0x00 00 01	3
⋮	⋮	⋮	⋮
@MAC7	0	0x00 00 01	3
@MAC8	0	0x80	3
@MAC9	0	0x40	3
@MAC10	0	0x20	3
@MAC11	0	0x10	3
@MAC12	0	0x08	3
@MAC13	0	0x04	3

TABLE III. FORWARDING TABLE OF THE SWITCH SW3 AFTER RECONFIGURATION

dot1dStatic-Address	*dot1dStatic-ReceivePort*	*dot1dStatic-AllowedToGoTo*	*dot1dStatic-Status*
@MAC1	0	0x00 00 02	3
⋮	⋮	⋮	⋮
@MAC7	0	0x00 00 02	3
@MAC8	0	0x80	3
@MAC9	0	0x40	3
@MAC10	0	0x20	3
@MAC11	0	0x10	3
@MAC12	0	0x08	3
@MAC13	0	0x04	3

 ISBN: 978-1-61208-264-6

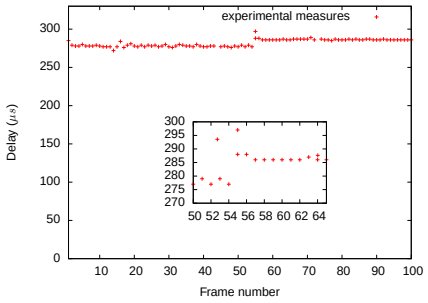

Figure 5. Delay of the flow 1 on device 13 (period: 288 ms)

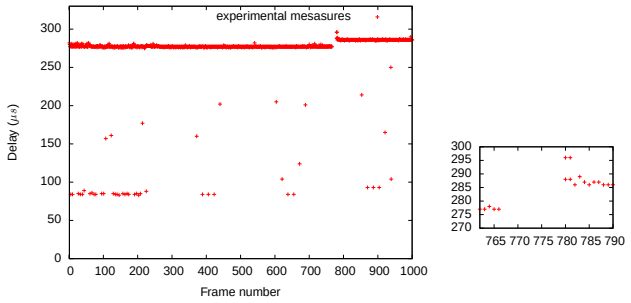

Figure 6. Delay of the flow 3 on device 8 (period: 18 ms)

a laboratory demonstrator (target TRL4) in order to study the impact of this active solution on others QoS parameters (e.g. the consumed bandwidth and its potential impact on the applicative end-to-end delays) and its robustness in embedded environment. Industrial switches will hence be used, which may very well decrease the detection time (and so the interruption time) if the "down state" is instantaneously notified (contrary to the values of "link_loss" in the link integrity test defined in the standard 802.3).

REFERENCES

[1] Department of Defense, "Military standard aircraft internal time division command/response multiplex data bus," MIL-STD-1553B, 1978.

[2] D. Monchaux, P. Gast, and J. Sangare, "Avionic-x : A demonstrator for the next generation launcher avionic," Embedded Real-Time Software and Systems (ERTS^2 12), Feb. 2012.

[3] A. Mifdaoui, F. Frances, and C. Fraboul, "Full duplex switched ethernet for next generation 1553B-based applications," Proc. IEEE Real Time and Embedded Technology and Applications Symposium (RTAS 07), Apr. 2007, pp. 45–56.

[4] J. Sommer, S. Gunreben, F. Feller, M. Kohn, A. Mifdaoui, D. Sass, and J. Scharf, "Ethernet–a survey on its fields of application," IEEE Communications Surveys & Tutorials, vol. 12, Apr. 2010, pp. 263–284.

[5] H. Zinner, J. Noebauer, T. Gallner, J. Seitz, and T. Waas, "Application and realization of gateways between conventional automotive and ip/ethernet-based networks," Proc. ACM Design Automation Conference (DAC 11), Jun. 2011, pp. 1–6.

TABLE IV. LOST FRAMES PER FLOW BY USING OUR SOLUTION (A) OR RSTP (B) IN THE CASE OF THE SW1-SW3 FAILURE

Device	Flow 1		Flow 2		Flow 3		Flow 4		Flow 5	
	A	B	A	B	A	B	A	B	A	B
2	0	0	0	0	-	-	-	-	-	-
3	0	0	0	0	0	0	0	0	0	0
4	0	0	0	0	0	0	0	0	0	0
5	0	0	0	0	0	0	0	0	-	-
6	0	0	0	0	0	0	0	0	-	-
7	0	0	-	-	-	-	-	-	-	-
8	0	4	0	4	14	56	14	56	-	-
9	2	14	2	14	-	-	-	-	-	-
10	0	0	0	0	0	0	0	0	-	-
11	2	14	8	28	-	-	-	-	-	-
12	0	0	2	14	2	14	8	28	0	0
13	0	4	-	-	-	-	-	-	-	-

[6] A. Mifdaoui, F. Frances, and C. Fraboul, "Centralized vs distributed communication scheme on Switched Ethernet for embedded military applications," Proc. IEEE Symposium on Industrial Embedded Systems (SIES 09), Jul. 2009, pp. 201–210.

[7] S. Vitturi, L. Peretti, L. Seno, M. Zigliotto, and C. Zunino, "Real-time ethernet networks for motion control," Computer Standards & Interfaces, vol. 33, Sep. 2011, pp. 465–476.

[8] J. Jasperneite, M. Schumacher, and K. Weber, "Limits of increasing the performance of industrial ethernet protocols," Proc. IEEE Emerging Technology and Factory Automation (ETFA 07), Sep. 2007, pp. 17 – 27.

[9] Grieu, "Analyse et évaluation de techniques de commutation ethernet pour l'interconnexion des systèmes avioniques," Ph.D. dissertation, Sep. 2004.

[10] J.-P. Georges, E. Rondeau, and T. Divoux, "Evaluation of switched ethernet in an industrial context by using the network calculus," Proc. IEEE Workshop on Factory Communication Systems (WFCS 02), Aug. 2002, pp. 19–26.

[11] J. Robert, J. Georges, T. Divoux, P. Miramont, B. Rmili *et al.*, "Ethernet networks for real-time systems: application to launchers," Proc. DAta Systems in Aerospace (DASIA 11), May 2011.

[12] T. Harima, "Introduction of iec activity on digital communication subsystem (overview of iec/sc65c)," Proc. IEEE ICCAS-SICE, Aug. 2009, pp. 1427–1431.

[13] G. Prytz, "Redundancy in industrial ethernet networks," Proc. IEEE Workshop on Factory Communication Systems (WFCS 06), Jun. 2006, pp. 380–385.

[14] M. Felser, "Media redundancy for profinet io," Proc. IEEE Workshop on Factory Communication Systems (WFCS 08), May 2008, pp. 325–330.

[15] M. Huynh, S. Goose, and P. Mohapatra, "Resilience technologies in ethernet," Computer Networks, vol. 54, Jan. 2010, pp. 57–78.

[16] IEEE Computer Society, "IEEE standards for information technology - telecommunications and information exchange between systems - local and metropolitan area networks - common specifications - part 3: Media access control (mac) bridges," ANSI/IEEE Std 802.1D, Dec. 2004.

[17] J. C. Mankins, "Technology readiness levels," NASA white paper, vol. 6, Apr. 1995.

[18] IEEE Computer Society, "IEEE standard for information technology - telecommunications and information exchange between systems - local and metropolitan area networks - specific requirements - part 3: Carrier sense multiple access with collision detection (csma/cd) access method and physical layer specifications," IEEE Std 802.3, Dec. 2008.

 ISBN: 978-1-61208-264-6

Development of Wideband Dual Polarized of Microstrip Antennas for Microwave Remote Sensing

Akbar Eslami, James Lee Jr, Henry Mishoe, Jamiiru Luttamaguzi, Ehsan Sheybani
Department of Technology, Elizabeth City State University
Elizabeth City, NC, U.S.A.
aeslami@mail.ecsu.edu

Manohar Deshpande
NASA Goddard Space Flight Center
Greenbelt, MD, U.S.A.
Manohar.D. Deshpande@nasa.gov

***Abstract*— A novel wideband dual polarized L-band antenna for NASA's microwave remote sensing applications has been designed, fabricated, and validated. The novel antenna structure consists of a rectangular microstrip antenna excited by capacitive coupled four probes. One of the linear polarizations is obtained by feeding two diagonally opposite probes with equal but out of phase signals. Other orthogonal polarization is obtained by feeding other remaining probes with equal but out of phase signals. The novel structure provides the band width in excess of 500 MHz (with the center frequency of 1.3 GHz) and the cross polarization below -40 dB. For validation purpose, two prototype antennas were fabricated and tested. The test results collected show relatively good agreement with simulation results. For achieving wider band width, it is required to use, in our design, the probes with diameter larger than conventional coaxial connector. A novel feed structure using larger size cylindrical via is designed. The new feed structure design is fabricated and validated before its integration with the antenna.**

Keywords- microstrip; L-band antenna; microwave; NASA.

I. INTRODUCTION

Microwave radars/radiometers are often used by NASA and other agencies for remote sensing of the Earth science parameters. The spatial and temporal resolutions obtainable with the microwave radars/radiometer observation depend upon their frequency bandwidth. It is always desirable for high spatial resolution to have radar operating at much higher bandwidth. The current antenna technology offers antenna with 20-50 MHz bandwidth. We proposed to develop a wideband (40%, 500MHz), dual polarized L-band array antenna for the next generation of microwave remote sensing radars and radiometers. The novel wideband antenna configuration will enable the scientists to observe the Earth science parameters with less than meter spatial resolution. In addition, the dual polarization capability with very low cross-polarization coupling (< -50 dB) will allow to measure the Stokes parameters with enhanced accuracy/sensitivity (-50 dB). Accurate measurement of the Stokes parameters will yield better estimates of permafrost and biomass which are critical parameters for development of Earth's carbon cycle model. It has been reported that dual polarization capability will provide biomass estimation with RMSE error of ~ 120 Mg/ha. 500 MHz bandwidth will allow achieving resolution in the range of 50 x 50 cm.

Researchers use different techniques and technology to design and fabricate an antenna. Microstrip has been one of the most popular microwave transmission lines in antenna. However, coplanar waveguide transmission lines have also been used in microwave transmission line as well. They are often selected over high frequency transmission line option such as stripline. John Coonrod has reported differences between microstrip and coplanar waveguide transmission lines to find the best performance applications [1]. Also, antenna size is always something that must be related to the wavelength and thus the frequency. Higher frequencies can utilize smaller antennas. However, the size of the antenna depends to the radiation resistance, the antenna feeding impedance, and radiation pattern [2]. Neil Chamberlain [3] has reported a method to fabricate a single-layer antenna that has application in military and commercial environments. He used a large-diameter center post as its supporting structure that allows for fabrication of a sufficiently rigid antenna element that can survive launch loads.

In this work, we present a procedure to design wideband dual polarized L-band antenna element and its microstrip feed line structure. We also describe a procedure used to fabricate and test these microwave components using the laboratory facility available at Microwave Instrument Technology Branch of NASA Goddard Space Flight Center (NASA-GSFC) in Maryland.

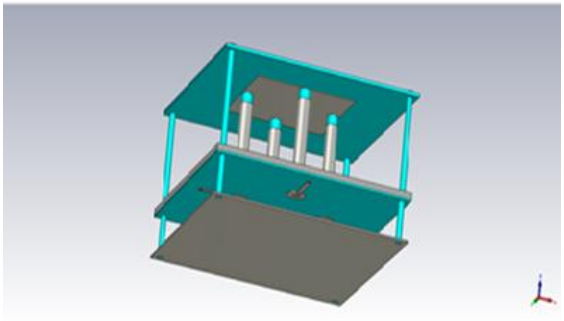

Figure 1. The computer model of L-band antenna

 ISBN: 978-1-61208-264-6

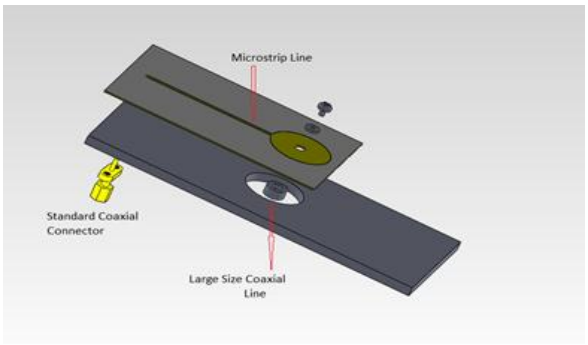

Figure 2. Transition for standard coaxial connector to large size coaxial line

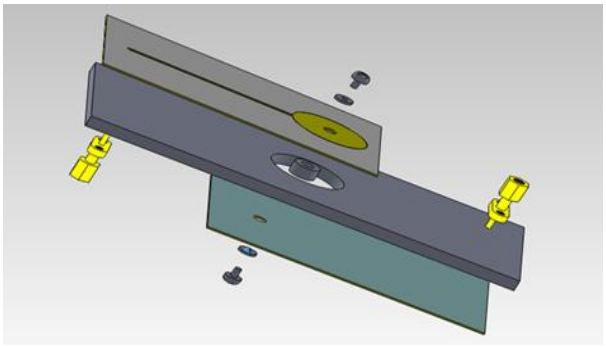

Figure 3. Microstrip feed line using larger size coaxial section

II. DESIGN METHODOLOGY

Two tasks need to be fulfilled to design and build microstrip antenna. Fist task starts with design of microstrip feed line using large size coaxial line. Fig. 1 shows the wideband dual polarized L-band antenna structure to be modeled. Our electromagnetic simulation of this antenna showed that for wideband operation, the four probes need to be of diameter much larger than the diameters of central conductor of a standard coaxial connector. Hence, a perfectly matched transition (as shown in Fig. 2) is required to connect conventional small size coaxial connector to a large size coaxial line. The desired transition has to transfer 100 % of power between the standard coaxial inputs to the larger size coaxial output. However, to test such a transition we would require unconventional large size coaxial connectors. To overcome this difficulty, we used back-to-back transitions (shown in Fig. 2), which results in a structure shown in Fig. 3, and which only require standard coaxial connectors to test the power transfer through a large size coaxial line section. The transition shown in Fig. 3 consists of metal plate of size 43.18 x 17.78 x1.27 cm (17 x 7 x 0.5 inches). On each side of the metal plate a dielectric substrate with dielectric constant of 2.94 and thickness 0.1mm were glued to the metal plate. On the top and bottom surface of these composite layers, a microstrip line having characteristic impedance of 50 Ohms was etched out to form 50 Ohms microstrip lines.

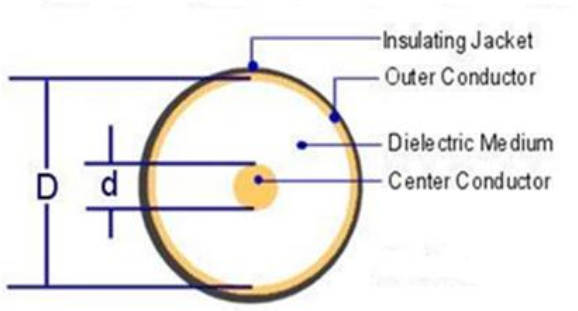

Figure 4. Cross section of coaxial line section

The width of the microstrip lines were calculated using [4]

$$Z_0 = \left(\frac{87}{\sqrt{\varepsilon_r + 1.41}}\right) \ln\left(\frac{5.98h}{0.8w + t}\right) \text{ ohms} \quad (1)$$

In (1), Z_0 = 50Ω is the characteristic impedance, ε_r= 2.94 is dielectric constant of the insulator, h= 0.8 mm is thickness of the dielectric insulator, and t= 0.08 mm is thickness of the copper strip. The width, w, of the microstrip using (1) is found to be 1.7 mm which was rounded to 2.00 mm. The coaxial line section used in the proposed transition has a cross section as shown in Fig 4.

In order to design the larger size coaxial line with characteristic impedance of 50 Ohms, (2) for a coaxial line was used to estimate inner and outer diameter of coaxial line section [5].

$$Z_0 = \left(\frac{138}{\sqrt{\varepsilon_r}}\right) \log\left(\frac{D}{d}\right) \quad \text{ohms} \quad (2)$$

In (2), the D represents the diameter of the hole in

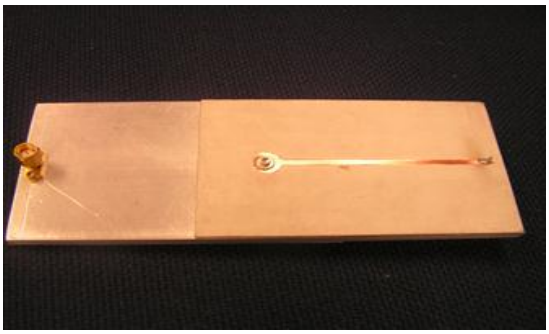

Figure 5. Photo of fabricated transition

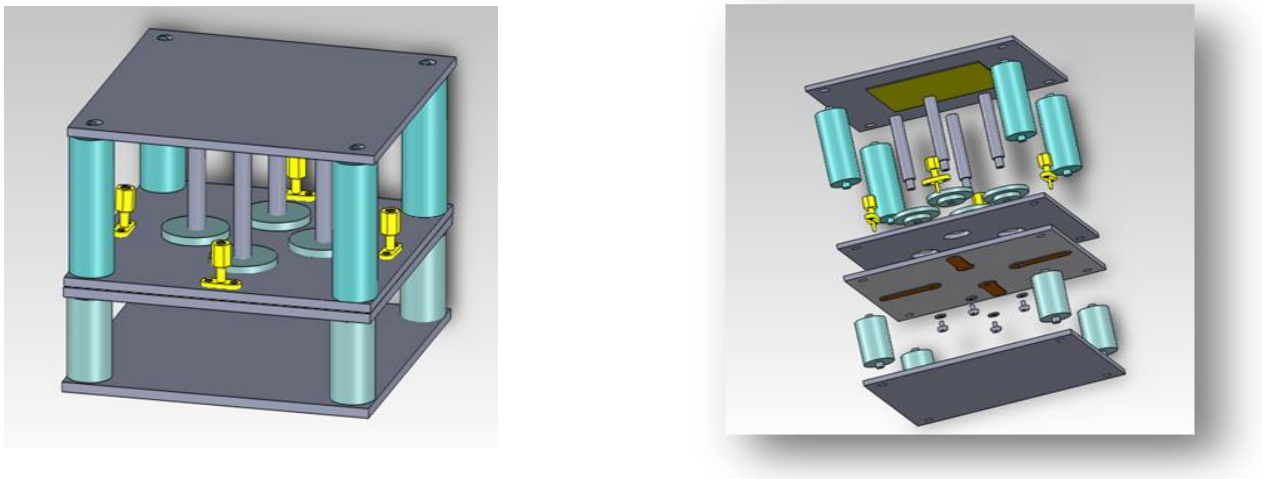

Figure 6. CAD model of different components of a L-band antenna

the aluminum plate, and the *d* represents the diameter of the center conductor pin located at the center of the hole. The ratio of *D/d* can be calculated with assuming the value of Z_0 is 50 ohms and ε_r= 1 for value of air dielectric.

Using the dimensions obtained by these two equations, the transition was fabricated using fabrication facilities available at Microwave Instrument Technology Branch of NASA-GSFC. A photo of fabricated transition is shown in Fig. 5.

The second task starts with design of wideband dual polarized L-band antenna. The simulation model of the proposed L-band antenna is shown in Fig. 1. The critical parameters that control the antenna performance are (1) diameter of probe, (2) rectangular patch size, (3) height of patch from the ground, (4) separation of probes from center. Using the CST Microwave Studio electromagnetic simulation model, the antenna performance was optimized with respect to above parameters [6].

Commercial SolidWorks Computer Aided Design (CAD) software is utilized to draw and design antenna components for fabrication purpose. The geometry of the desired model is given in Fig. 6.

The two different types of L-band antennas were fabricated and tested. The first antenna had a thick substrate, while second antenna had a thin substrate. The L-band antenna consisted of four layers including an aluminum plate at the base, substrate with copper strip in the middle, aluminum ground plate attached to top of the middle substrate, and substrate with copper radiation patch at top. Four radiation poles are connected through ground plate and substrate to four copper transmitting strip lines. The commercial CST Microwave Studio software was used to obtain the desired specifications of the dimensions of the L-band antenna. The antenna was fabricated to the specified dimensions and it is shown in Fig. 7.

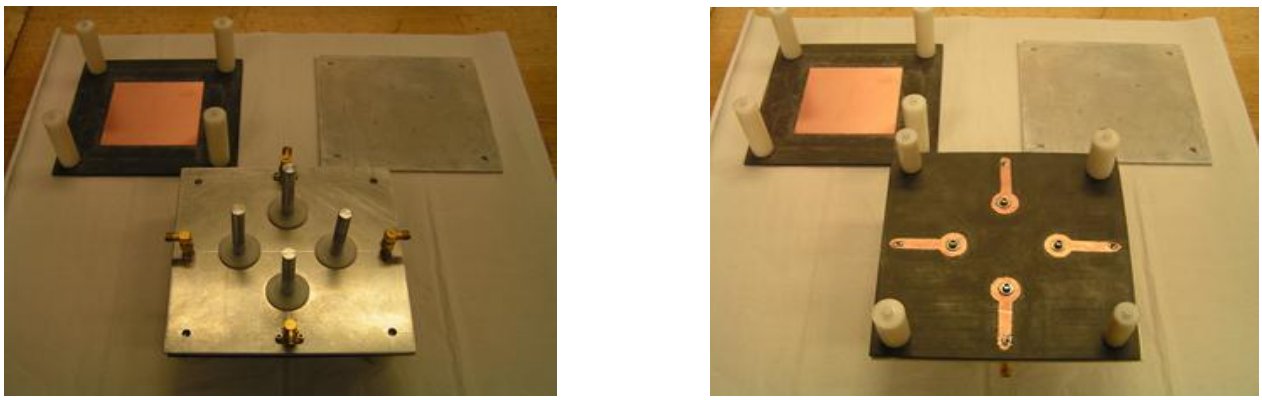

Figure 7. Components of fabricated antenna

 ISBN: 978-1-61208-264-6

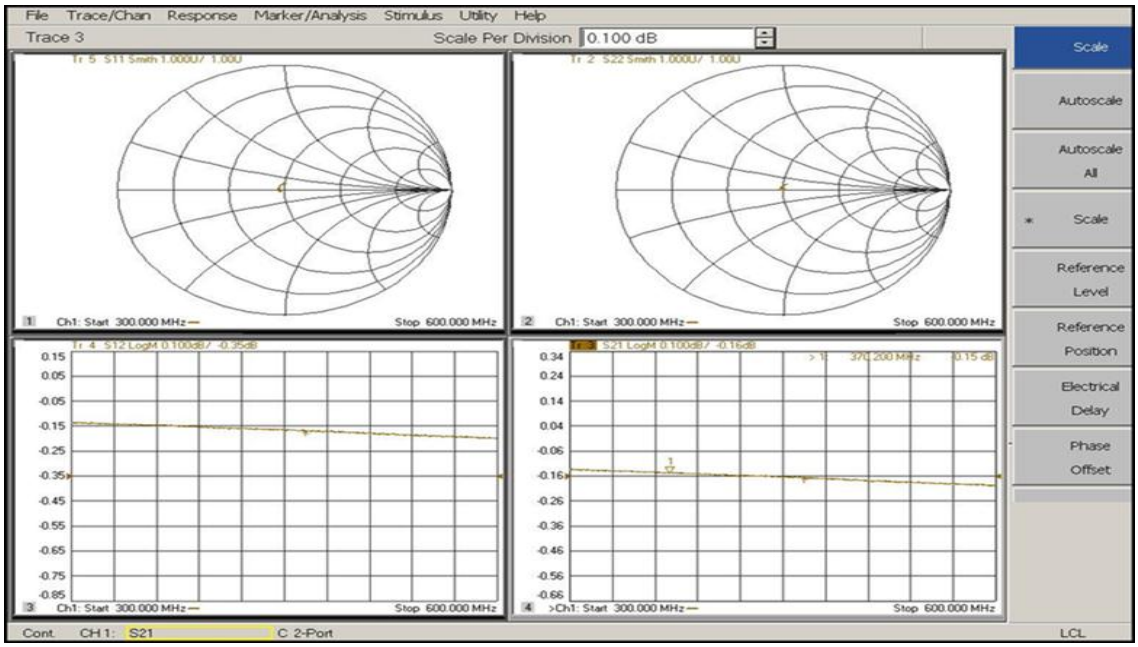

Figure 8. Microstrip test results

The second antenna has same specifications except using different substrate to compare the results.

III. RESULTS

The microstrip and two L-band antennas were tested and reported as following. The fabricated microstrip model shown in Fig. 5 was tested with the PNA analyzer to validate the design specification. The graphs in the results section indicate that the microstrip met the desired design. The results shown in Fig. 8 confirm that there was very low return loss (low S11 and S22) at both ports. The top two smith charts within the graph both represent return loss in ports one and two. The S11 and S22 curves are very minimal and tight to the center as expected. The bottom charts both represent transfer of power through the design structure from one port to the other. The results show about -0.13db of loss of power between the ports one and two. Note that these transitions were fabricated and tested for frequency range of 0.3-0.6 GHz as shown in Fig. 8. An identical approach was used to design a transition for the L-band.

Two samples of antenna shown in Fig. 7 were fabricated and measured. It was found that both samples gave identical performance within the experimental tolerances.

First the L-band dual polarized antenna with thick substrate was tested for its input Voltage Standing Wave Ratio (VSWR) and its impedance matching performance outside the anechoic chamber. It was also tested for its radiation performance inside the electro- magnetic anechoic chamber room. Anechoic means no echoes which imply the room is free of reflections which gives accurate measurements. The antenna has four ports and to perform measurements two ports were terminated into matched load and other two were excited through a 3dB hybrid coupler. Fig. 9 shows input VSWR when two of four ports were excited through a 3dB hybrid coupler and other two ports were terminated into matched loads. Fig. 9 shows both measured and simulated results obtained using CST Microwave Studio software. A good agreement between calculated and measured VSWR is observed. Desired results are lower than -10 db's for entire desired band showing a good impedance match for the antenna.

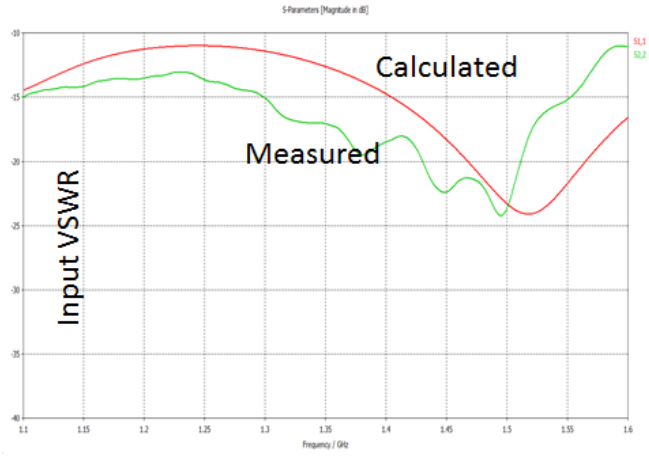

Figure 9. L-band antenna (First model Port1)

 ISBN: 978-1-61208-264-6

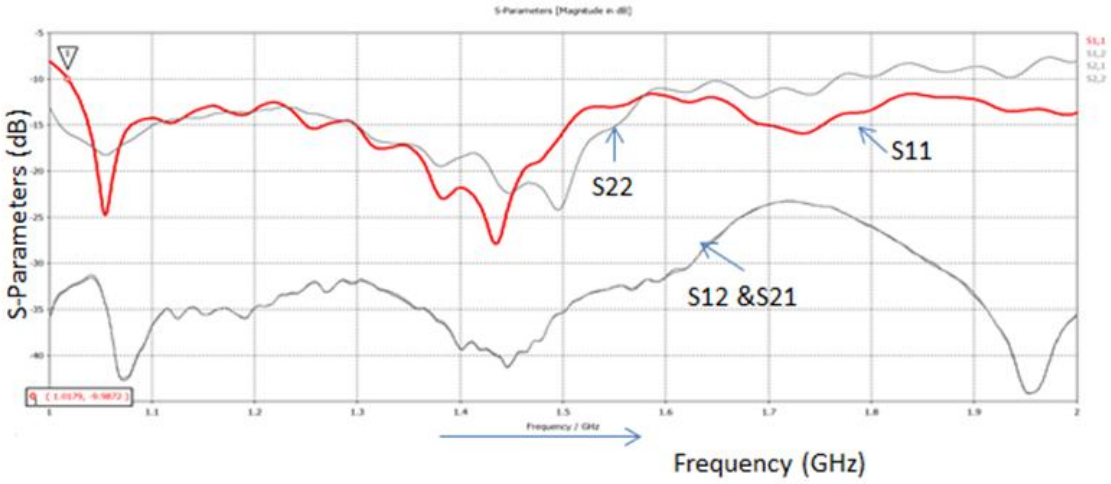

Figure 10. L-band antenna (Second model ports 1, 2)

The next step was to test L-band dual polarized antenna with thin substrate. To configure the four port antenna into a dual polarized two port antenna, pair of two diagonally opposite probes is fed through hybrid couplers. This feeding arrangement converts the four port antenna into two port antenna. S-parameters (S11, S21, S12, and S22) of the dual polarized antenna were measured and shown in Fig. 10. The curves for S11 and S22 show that the antenna is impedance matched over the frequency band covering 1.0 – 1.7 GHz band. The curves for S12 and S21 show that the cross coupling between the two linear polarization is below -30 dB.

IV. CONCLUSION AND FUTURE WORK

In this project, the performance of fabricated microstrip antenna has been evaluated. Both measured and calculated results are presented and found to be in a good agreement. The SolidWorks CAD commercial software is utilized to visualize components for fabrication process. The model has been fabricated in a traditional machine shop and tested several times to collect data from the PNA Analyzer. Despite working with traditional method for fabricating microstrip and antenna, good agreement was achieved between the simulated and measured results. This project was involved extensive research, design, fabrication, constant testing, and troubleshooting. The wideband L-band designed and tested in this work is planned to be used in a large L-band array antenna for NASA's remote sensing.

ACKNOWLEDGMENT

This research is supported by NASA-NSTI grant.

REFERENCES

[1] J. Coonrod and B. Rautio, "Comparing Microstrip and CPW Performance," Microwave Journal, July. 2012, pp. 74-86.

[2] C. Stoij, "Antennas the mm Wave Advantage," Microwave Journal, August. 2012, pp. 84-96.

[3] N. F. Chamberlain, "Single-Layer, All-Metal Patch Antenna Element With Wide Bandwidth," NASA Tech Briefs, June. 2012, pp. 50.

[4] D. Brooks, "Embedded Microstrip," Printed Circuit Design, a Miller Freeman publication, February. 2000.

[5] Wikipedia "Coaxial cable," http://en.wikipedia.org/wiki/Coaxial_cable

[6] "CST Microwave Studio brochure," http://www.cst.com/Content/Documents/Products/cst-studio-suite-2012-brochure-low.pdf

 ISBN: 978-1-61208-264-6

Hybrid Beamformer for TPMS Interference Suppression

Suk-seung Hwang
Dept. of Mechatronics Engineering, College of Engineering
Chosun University
Gwangju, Korea
hwangss@chosun.ac.kr

Cheol Park* and Seong-min Kim¶
Department of Advanced parts and Materials Engineering
Chosun University
Gwangju, Korea
*samasin@nate.com, ¶millionairek@naver.com

***Abstract*—The Tire Pressure Monitoring System (TPMS) is a type of the wireless communication device for vehicles, defined as a safety assist system for enabling drivers to efficiently check and manage tires. In the TPMS communications, external electric and electronic devices may interfere with the exact data transmission. In this paper, we propose a hybrid TPMS beamformer based on a switching beamformer and minimum-variance distortionless–response (MVDR) beamformer for selecting an efficient algorithm depending on circumstances in order to eliminate the interference and to transfer the accurate data to drivers. We also suggest an effective signal decision algorithm based on the signal-to-interference and noise ratio (SINR) in order to ensure the transferred data reliability. The performance of the suggested hybrid TPMS beamformer and the effective signal decision algorithm is identified through a computer simulation example.**

Keywords-Tire Pressure Monitoring System (TPMS); Hybrid Beamformer; Switching Beamformer; Minimum-Variance Distortionless-Response (MVDR); Interference Suppression.

I. INTRODUCTION

The Tire Pressure Monitoring System (TPMS) is a safety assist device for measuring tire temperature and pressure by means of a sensor in each tire of a vehicle, transmitting the measured data to the signal processing unit of the vehicle, and displaying them in the display unit to inform the driver about the tire state information in real time [1]. The TPMS employs various carrier frequencies such as 433.92 MHz in U.S.A and Europe, and 433.92 MHz and 447 MHz in Korea.

Most of TPMSs currently employ the one-way wireless communication technique with low data transmission efficiency and decision reliability. In order to overcome this problem, we suggest a method for deciding the TPMS data reliability of high performance based on the bidirectional communications. An advantage of the bidirectional communications is that it may save the power of the battery in the sensor unit installed in each tire, because it transmits the data when only it is required. Also, since it contains Ack/Nack data which indicates the effectiveness of the transmitted data and E/N data which indicates the condition of a tire, it may efficiently improve the data reliability. Decision of data efficiency by the suggested algorithm is based on the measured signal-to-interference and noise ratio (SINR).

The TPMS employing various frequencies across the globe may experience the serious interference by high-power signals from external electric and electronic devices utilizing the similar frequencies. Researchers have studied switching beamformers [2] and minimum-variance distortionless-response (MVDR) beamformers [3] in order to eliminate the aforementioned interference. Although the switching beamformer has low computational complexity, it has low interference elimination performance. Although the MVDR beamformer has high interference elimination performance, it has extremely high computational complexity due to the calculation of an auto-correlation matrix. In this paper, we propose a hybrid beamformer, which selects one out of the switching beamformer and the MVDR beamformer according to circumstances. Decision of selecting one out of two beamformers is based on the measured SINR. We consider a structure which has a layout of M receiving antennas in a line in the center of a relevant vehicle to use the beamformer for the TPMS. In order to eliminate the interference from other tires and reduce the power consumption of the battery in a sensor unit installed in each tire, we employ the Gold code to each tire.

The rest of this paper is organized as follows. In Section II, we define the received signal model for TPMS and the interference signals in additive white Gaussian noise (AWGN). In Section III, we describe effective signal decision algorithms in signal processing unit and sensor unit, including flow-charts. The hybrid beamformer based on the switching and MVDR beamformer is proposed to effectively suppress interference signals from external devices in Section IV. Computer simulations are provided in Section V to demonstrate the performance of the proposed technique. Finally, conclusions and the future work are outlined in Section VI.

II. RECEIVED SIGNAL MODEL

Fig. 1 shows an example of the structure with a layout of M receiving antennas in the center of a vehicle at given intervals in a line and one transmitting antenna in each tire, for using the hybrid TPMS beamformer. The black devices seen at the car hood and the door in Fig.1 are examples of the external electric or electronic interference sources. At the sample index k, the received signal is given by

$$\mathbf{z}(k) = \sum_{i=1}^{4} \mathbf{a}_i g_i(k) b_i(k) + \mathbf{A}\mathbf{j}(k) + \mathbf{n}(k) \qquad (1)$$

where $\mathbf{a}_i$ is an array response vector (size $M \times 1$) for the i th tire based on the uniform linear array (ULA), $g_i(k)$ is a cyclostationary Gold code (size N) for the i th tire, and $b_i(k)$ is a measured data bit for the i th tire, which remains

 ISBN: 978-1-61208-264-6

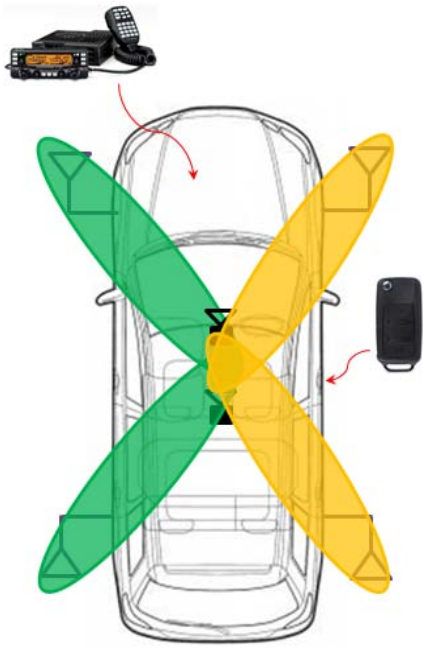

Figure 1. Antenna arrangement inside the vehicle for Hybrid TPMS beamformer

constant over the length of one cycle of the Gold code. The upper limit of the summation in (1) is four, because we assume that the number of tires is four. $\mathbf{A}$ is a $M \times P$ array response matrix, P is the number of interference signals, and $\mathbf{j}(k)$ is an interference signal vector (size P). Also, $\mathbf{n}(k)$ is an AWGN vector composed of independent and identically distributed components, each with zero mean and variance σ^2. The angle-of-arrival (AOA) array response vector uses the equation described in [4,5]. Although we generally assume that the interelement spacing is a half of the wavelength, we are currently investigating the effect for reducing interelement spacing to a quarter or one-eighth of the wavelength. In order to save the length of entire space for the antenna elements, we are studying to employ the rectangular or the circular antenna array structure in the center of a vehicle.

An equation of the received signal SINR [6] for deciding effective signals is given by

$$SINR = 10\log_{10}\left(\frac{S.Power}{N.Power + I.Power}\right) \qquad (2)$$

where $S.Power$ (Signal Power) is the signal power transmitted from each tire, $N.Power$ is the noise power, and $I.Power$ is the interference power. The received signal SINR is measured using preamble data, which a receiver knows beforehand.

III. EFFECTIVE SIGNAL DECISION ALGORITHM

In this section, we propose a TPMS effective signal decision algorithm based on the duplex TPMS data architecture [2].

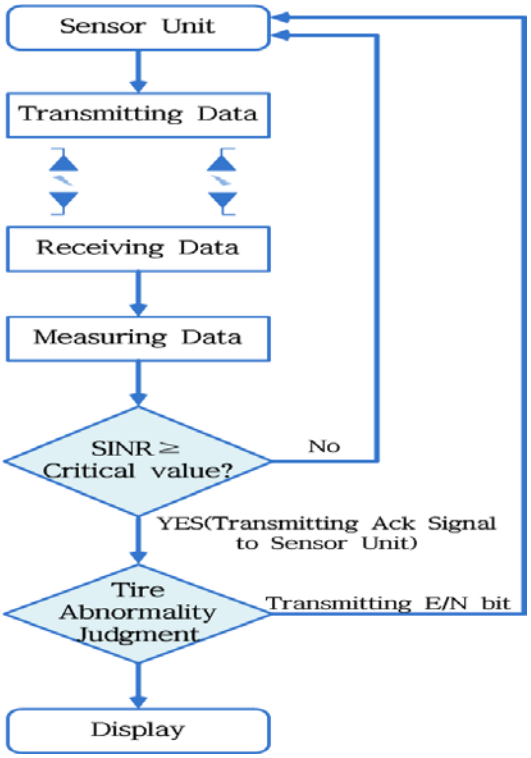

Figure 2. Flow-chart for determining the effective signal, based on the duplex TPMS wireless communication system (signal processing unit)

A. Effective Signal Decision Algorithm in Signal Processing Unit

A flow chart for the effective signal decision in the signal processing unit installed in a vehicle is shown in Fig. 2. The signal processing unit measures SINR of the received signal, compares the measured SINR with a threshold. If the measured SINR is greater than the critical value, it sends the Ack signal, which means that the transmitted signal is effective, to the sensor unit to request transmitting the main data. On the contrary, if the measured SINR is smaller than the critical value, it does not send any signal and the sensor unit recognizes Nack which means that the transmitted signal is not effective. In this case, the sensor unit requests retransmitting the reference data. After receiving the main data, the signal processing unit decides the normal or abnormal state of a tire using the main data. If the tire is decided normal, the signal processing unit transmits N bit (for example, bit 1) which indicates the normal mode, and operates in the normal mode which indicates the normal tire state (for example, receiving data once per minute). On the contrary, if the tire is decided abnormal, the signal processing unit transmits E signal (for example, bit -1) which indicates an emergency mode, and operates in the emergency mode which indicates a dangerous tire state (for example, receiving data once per second). The data processed in the signal processing unit is sent to the display unit to enable a driver to check the tire condition.

 ISBN: 978-1-61208-264-6

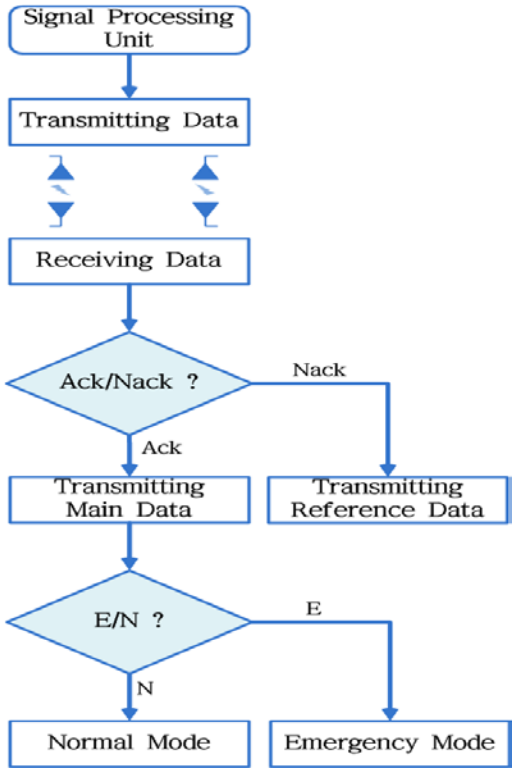

Figure 3. Flow-chart for determining the effective signal, based on the duplex TPMS wireless communication system (sensor unit)

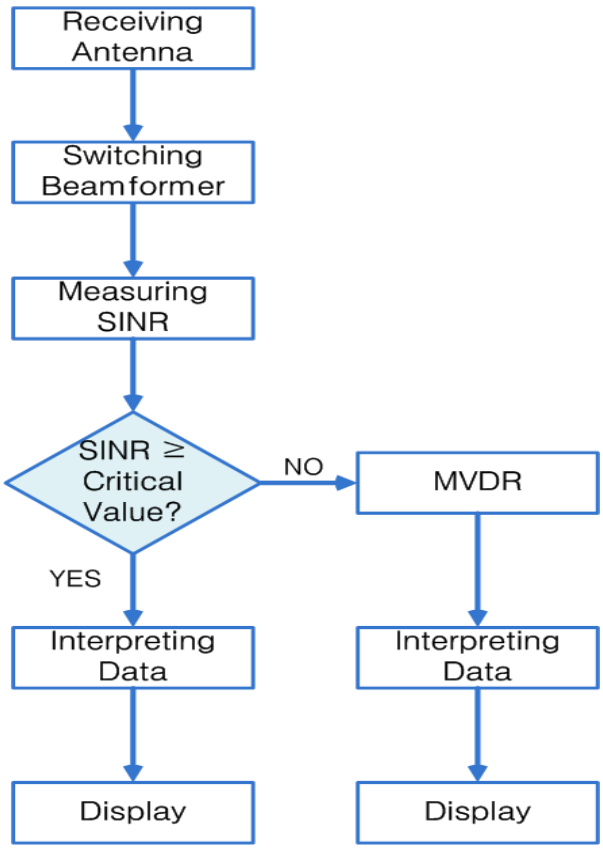

Figure 4. Flow chart of the hybrid TPMS beamformer

B. Effective Signal Decision Algorithm in Sensor Unit

Fig. 3 shows a flow chart for the suggested effective signal decision method based on a duplex TPMS communication system in the sensor unit. The sensor unit receives Ack/Nack and E/N bits from the signal processing unit. If the sensor receives the Ack bit (for example, bit 1), it transmits main data to the signal processing unit. On the contrary, if the sensor unit receives Nack bit (for example, no bit), it retransmits reference data (preamble data) to the signal processing unit. If the signal transmitted from the main data is decided N bit (for example, bit 1), the sensor unit operates in the normal mode (for example, transmitting data once per minute). If it is decided E bit (for example, bit -1), the sensor unit operates in the emergency mode (for example, transmits data once per second).

IV. HYBRID BEAMFORMER

In order to efficiently suppress interference signals from external devices and receive the accurate data from the sensor unit, we propose a hybrid beamformer, which selectively uses the switching beamformer and MVDR beamformer after comparing the measured SINR and the given threshold. The switching beamfomer has obviously low computational complexity comparing with the MVDR beamformer, because it does not require an auto-correlation matrix but the MVDR beamfore requires that. Hybrid beamformer forms beam in a desired direction to receive TPMS data. The received signal includes TPMS signals of each tire, interference from external devices, and noise. The hybrid beamformer basically uses the switching beamformer to weaken interference signals. If the output SINR of the switching beamformer is greater than the threshold, the output signal of the switching beamformer is analyzed to display the data in the display unit and thus to inform a driver about the tire condition. However, if the measured SINR is smaller than the threshold, the hybrid beamformer changes the mode from the switching beamformer to the MVDR beamformer as shown in Fig. 4.

Since the switching beamformer has very low computational complexity and has the relatively good performance of interference suppression, it is used as a basic beamformer of the hybrid beamformer. That is, if the measured SINR is greater than a specific threshold, the hybrid beamformer operates in the switching beamformer mode. However, if the SINR of the switching beamformer output is smaller than the threshold, it results the low ratio of the accurate data reception due to the interference signals. In this case, we employ the MVDR beamformer, which forms beam in the desired direction and nulls in the directions of the interference signals to minimize them, at the same time [7]. The MVDR beamformer has excellent performance of interference elimination, but it needs calculation of an auto-correlation matrix resulted in very high computational complexity. The proposed hybrid beamformer optimizes interference elimination performance and computational

 ISBN: 978-1-61208-264-6

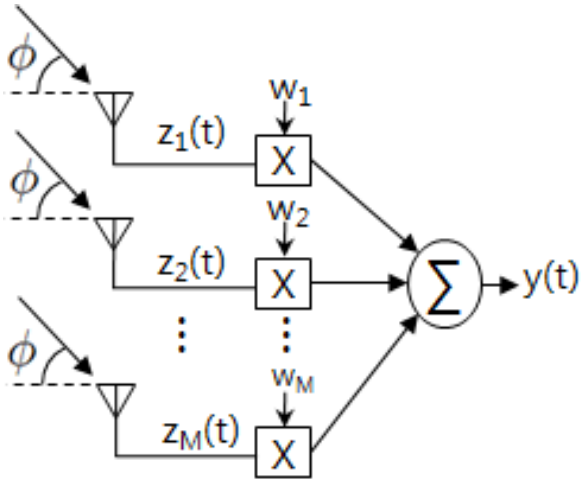

Figure 5. Conventional beamformer structure

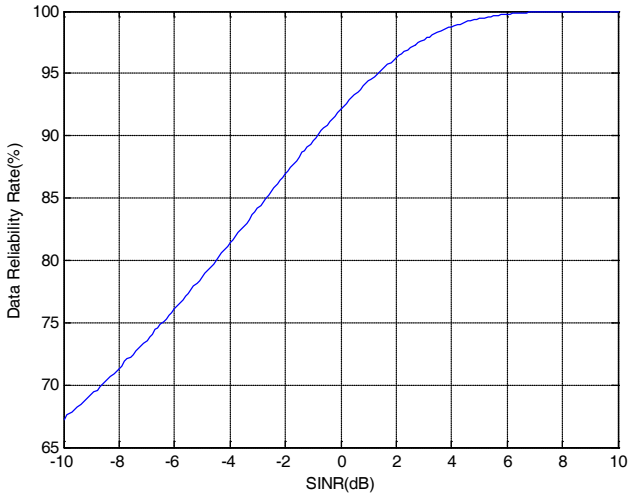

Figure 6. Data reliability rate via SINR

complexity efficiency with two beamformers, which have obvious advantages and disadvantages.

A. Switching beamformer

The switching beamformer is defined as to alternately use more than one weight vectors based on the AOA vector to form beams to directions of interest. The switching beamformer weight vector for i th tire signal with a beamformer architecture shown in Fig. 5 is given by

$$\mathbf{w}_{s_i} = \frac{\mathbf{a}_i}{\sqrt{\mathbf{a}_i^H \mathbf{a}_i}} \tag{3}$$

where ^{H} denotes complex conjugate transpose. The aforementioned weight vector generates a beam factor of size one for the i th tire to receive TPMS signal.

B. MVDR Beamformer

The MVDR beamformer calculates a weight vector for minimizing the power of the beamformer output while maintaining the power of the desired signal. The MVDR weight vector is computed from

$$\min \mathbf{w}^H \mathbf{R}\mathbf{w} \text{ subject to } \mathbf{a}_i^H \mathbf{w} = 1 \tag{4}$$

where $\mathbf{R} = E\left[\mathbf{z}(k)\mathbf{z}^H(k)\right]$ is an auto-correlation matrix of the received signal [8]. The MVDR weight vector [9,10] for the i th tire is given by

$$\mathbf{w}_{MVDR} = \left[\mathbf{a}_i^H \mathbf{R}^{-1} \mathbf{a}_i\right]^{-1} \mathbf{R}^{-1} \mathbf{a}_i . \tag{5}$$

It forms a beam with the factor of size '1' to the direction of the i th tire signals and nulls interference signals to minimize them, at the same time. The hybrid beamformer output for the i th tire is given by

$$y_i(k) = \mathbf{w}_i^H \mathbf{z}(k). \tag{6}$$

This output contains the TPMS signal of the i th tire, noise, and residual interference signal. $\mathbf{w}_i$ selectively uses the weight vector of the switching beamformer or MVDR depending on circumstances. The output of the hybrid beamformer is despreaded using the unique Gold code for the i th tire.

V. COMPUTER SIMULATION

Computer simulation result is described below to identify the performance of SINR threshold decision for an effective data decision method and the hybrid beamforming technology. We use a million received signal data for determining the SINR threshold for the suggested effective data decision method and set the number of antennas as one. Fig. 6 shows data reliability from –10 dB to 10 dB with respect to SINR. From the figure, we observe that increasing SINR results in rising data reliability. This result is utilized to determine the threshold for the proposed hybrid beamformer.

Six receiving antennas are used to identify the performance of the suggested hybrid TPMS interference suppression. It is based on the assumption that the received signal included three interference signals and noise, and a Gold code of $N = 15$ is given to the TPMS signal of each tire. The incident angles of transmitted signals for each tire are assumed 60°, 120°, 240°, and 300°, respectively. The incident angles for 3 interference signals are randomly assumed 89°, 175°, and 340°, respectively. It is identified that the output SINR threshold value, which is a reference of data reliability 99% is about 4.4 dB from Fig. 6. This value is assumed as a threshold in the simulation for evaluating hybrid beamformer performance.

Fig. 7(a) and 7(b) show beampatterns for the switching beamformer which forms beams to direction of incidents angles 60° and 300° with respect to the right-front and right–rear tire TMPS signals and which forms beams to direction of incident angles 120° and 240° with respect to the left-front and left–rear tire TMPS signals, respectively. Fig. 8(a) and 8(b)

 ISBN: 978-1-61208-264-6

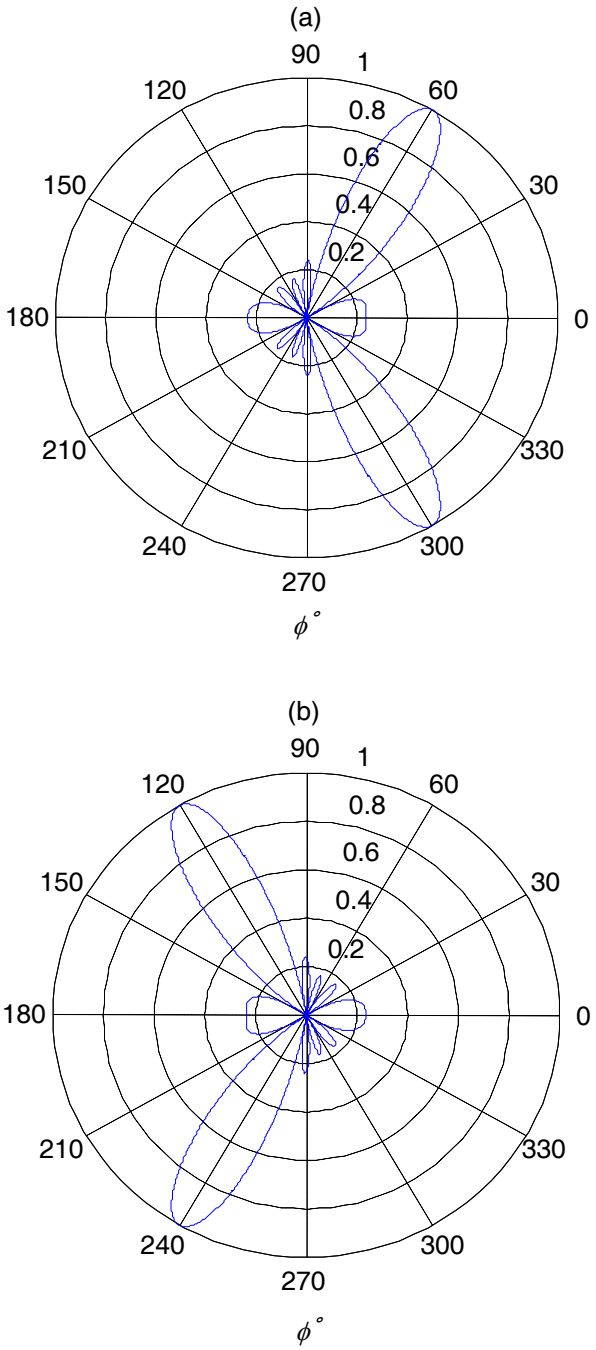

Figure 7. Beam pattern for switching beamformer with six antennas (a) Beam pattern for right tire TPMS signals with 60° and 300° incidence angles, (b) Beam pattern for left tire TPMS signals with 120° and 240° incidence angles

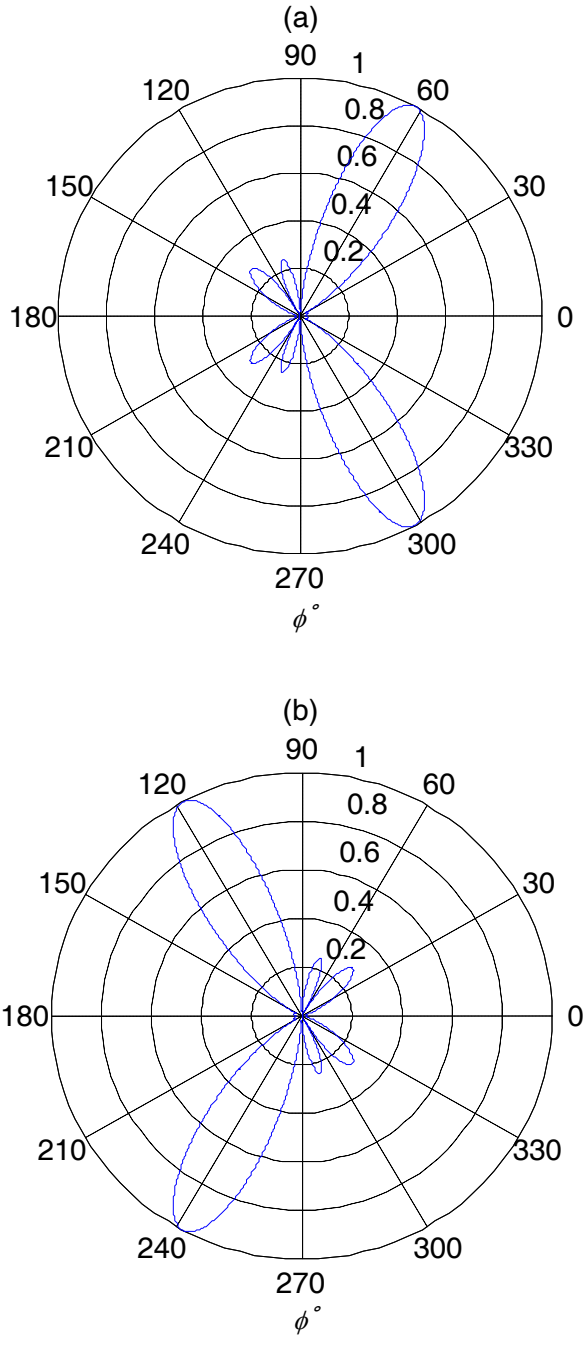

Figure 8. Beam pattern for MVDR beamformer with six antennas (a) Beam pattern for right tire TPMS signals with 60° and 300° incidence angles, (b) Beam pattern for left tire TPMS signals with 120° and 240° incidence angles

show beampatterns for the MVDR beamfomer which forms beams for right and left tire TPMS signals, respectively. Note that the MVDR beamformer forms nulls to incident angles of interference signals, unlike the switching beamfomer. Since the array response vector includes the cosine function, the proposed hybrid beamformer alternately uses two weight vectors (not four weight vectors) for the front tire in the right side and the front tire in the left side to receive the data from all four tires [2].

Fig. 9 shows output SINR curve per signal-to-noise ratio (SNR) for interference-to-signal ratio (ISR) = 3 dB, for 99% data reliability (4.4dB SINR). From the figure, we observe that the switching beamformer is used when the SNR is greater than -4 dB because the output SINR is greater than the threshold. In

 ISBN: 978-1-61208-264-6

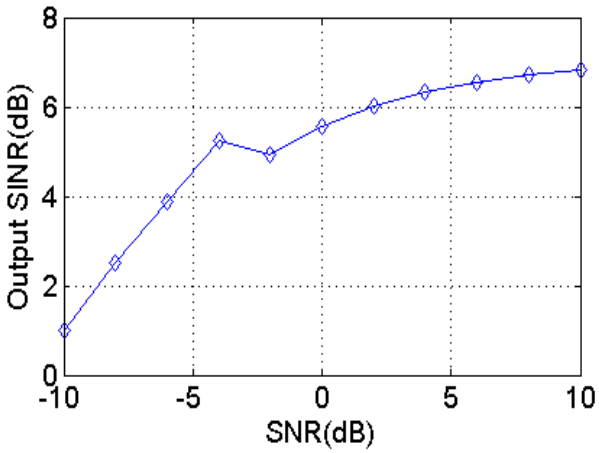

Figure 9. Output SINR per ISR for ISR = 3 dB

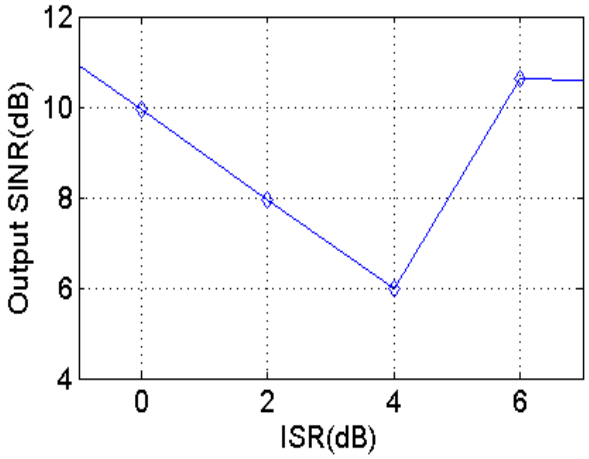

Figure 10. Output SINR per ISR for SNR = 0 dB

the section SNR = -4 dB or lower, the SINR is smaller than the threshold and the switching beamformer mode is converted to the MVDR beamformer mode. Fig. 10 shows the output SINR curve per ISR for SNR = 0 dB, for 99% data reliability (4.4dB SINR). It has a section where SINR decreases and then increases at ISR = 4 dB, which shows the result that the hybrid beamformer operates in the switching beamformer mode and then is converted to the MVDR beamformer mode where SINR is below the threshold.

VI. Conclusion and Future Work

Enactment for compulsory use of TPMS to inform a driver about the tire condition in real time is globally underway in order to prevent serious traffic accidents due to abnormal tires. Since the TPMS employs wireless communication technique, it is essential to ensure the data reliability. For the high TPMS data reliability, we considered the duplex wireless communication technique, which is more developed than the one-way wireless communication method used in the conventional TPMS, and suggested a data reliability decision method according to the threshold based on SINR of received signals. We also proposed a hybrid TPMS beamformer based on the switching beamformer and MVDR beamformer in order to effectively eliminate interference caused from external devices. An optimum algorithm between two beamformers is selected based on the measured SINR according to circumstances for exact data transmission. The unique Gold code is employed to each tire in order to eliminate interference signals from other tires and to reduce the power consumption of a battery in the sensor unit of TPMS. The performance of the proposed hybrid TPMS beamformer was illustrated via the computer simulation example. In the future work, we will consider the effects of the car body and the ground, and the coupling between antennas for TPMS.

Acknowledgment

This research was supported by Basic Science Research Program through the National Research Foundation of Korea (NRF) funded by the Ministry of Education, Science and Technology (No. 2012-0008837)

This research was supported by Basic Science Research Program thorough the National research Foundation of Korea (NRF) funded by the Ministry of Education, Science and Technology (No. 2011-0024811)

References

[1] Q. Zhang, B. Liu, and G. Liu, “Design of tire pressure monitoring system based on resonance frequency method”, IEEE/ASME International Conference on, Advanced Intelligent Mechatronics 2009, AIM 2009, pp. 781-785, July 2009.

[2] S. Hwang, C. Park, S. Kim, G. Kwon, J. Pyun, and S. Shin, “TPMS switching beamformer based on duplex wireless communications for interference suppression”, 2012 IEEE International Conference on Vehicular Electronics and Safety , pp. 228-233, July 24-27, 2012.

[3] S. Hwang, S. Kim, and C. Park, “TPMS interference iuppression based on beamforming”, The Journal of The Korea Institute of Electronic Communication Sciences, Vol. 6, No. 2, pp. 180-185, April 2011.

[4] S. Yoo, S. Kim, D. H. Youn, and C. Lee, “Multipath mitigation technique using null-steering beamformer for positioning system”, IEEE Semiannual, Vehicular Technology Conference, 2003. VTC 2003-Spring, Vol. 1, pp. 602-605, April 2003.

[5] Y. Yang, J. Wang, and Z. Yin, “A new approach for source localization of wideband signals based on matching pursuit”, ICWAPR '07, Vol. 3, pp. 1020-1025, Nov. 2007.

[6] G. Song, K. Stewart, R. Love, X. Zhuang, and Y. Sun, “Asymptotic performance of broadcast services in IEEE 802.16e with CSTD,” Vehicular Technology Conference 2006, Sept. 2006.

[7] E. A. P. Habets, J. Benesty, and P. A. Naylor, “A speech distortion and interference rejection constraint beamformer”, IEEE TRANSACTIONS ON AUDIO, SPEECH, AND LANGUAGE PROCESSING, Vol. 20, No. 3, pp. 854-867, Mar. 2012.

[8] J. Benesty, J. Chen, and Y. Huang, “A generalized MVDR spectrum”, IEEE SIGNAL PROCESSING LETTERS, Vol. 12, No. 12, pp. 827-830, Dec. 2005.

[9] D. Li, Q. Yin, P. Mu, and W. Guo, “Robust MVDR beamforming using the DOA matrix decomposition”, 2011 1st International Symposium on Access Spaces (ISAS), pp. 105-110, June 2011.

 ISBN: 978-1-61208-264-6

Multi-millisecond GNSS Maximum Likelihood Bit Synchronization Method

Gerardo Ludovico Puga, Pedro Agustín Roncagliolo, and Javier Gonzalo García
Laboratorio de Electrónica Industrial, Control e Instrumentación (LEICI),
Dto. Electrotecnia, Facultad de Ingeniería, UNLP, La Plata, Argentina.
Emails: { gerardo.puga, agustinr, jgarcia}@ing.unlp.edu.ar

***Abstract*—This paper introduces a new maximum likelihood bit synchronization algorithm that can be tailored to be used with different types of GNSS signals (GPS, GLONASS). A preliminary version of this work was presented in a previous paper by the same authors. In that paper, it was shown that this method allows to determine the positions of the bit edges in the signal using multiple millisecond correlation values. Using longer correlation times for bit synchronization decreases the peak processor load on embedded GNSS receivers that are based on carrier and code tracking loops for signal tracking, since for this kind of processing, longer correlation times allow for lower tracking loop update rates. In that previous paper it was also shown (through the use of simulations) that this new method presented lower error rates compared to the histogram method for fixed length observation intervals. The present paper extends these results in two ways. First, it generalizes the proposed method to N-millisecond integrations, providing a framework for automatic generation of the Viterbi state machine that drives the synchronization. Second, this paper provides a simple analytical expression that can be used to estimate the synchronization error rate of the algorithm, and identifies its most important design parameters.**

Keywords-GPS; GLONASS; receiver; data modulation

I. INTRODUCTION

Global Navigation Satellite Systems (GNSS) enable any vehicle equipped with a receiver to determine its position and velocity based on the signals transmitted by a constellation of satellites placed in carefully controlled orbits. For each signal present in the antenna the receiver determines a pseudorange measurement, which is a quantity related to the true geometrical range (distance) between the receiver and the transmitting satellite. Using four or more of these measurements, the receiver can determine its spatial coordinates with an error in the order of a few meters. User velocity determination is performed in a similar fashion, using quantities related to the Doppler deviation of the signal carrier frequency.

There are currently two GNSS systems in full operational status: GPS, the GNSS System maintained by the United States Department of Defense (DoD), and its russian counterpart GLONASS. There are other GNSS systems being developed by different national entities, but as of 2012 these are still on the planning stage or have been only partially deployed (COMPASS, Galileo). A detailed description of the signal of GPS and GLONASS can be found in the literature [1][2][3][4].

Both GPS and GLONASS satellites transmit data at 50 bps. GPS encodes the bits using bipolar NRZ pulses, while GLONASS uses Manchester coding. Before being able to decode the data frames transmitted by a satellite, the receiver needs to perform a synchronization process during which the position of the data bit edges is determined.

Because of the structure of the signal, there is only partial uncertainty in the knowledge of the position of the bit edges. GPS and GLONASS signals are spread using a DS-SS (Direct Sequence Spread Spectrum) periodic spreading sequence. This spreading sequence is 1023 chips long for GPS, and 511 chips long for GLONASS. In both cases the spreading sequence repeats itself after 1 ms. Data bit sign transitions are aligned with the start of the new period of the spreading sequence. One data bit pulse extends exactly 20 spreading sequence periods. Since the start of the each period of the spreading sequence is known to the receiver, then there are only 20 different possibilities for the data bit sequence alignment. During bit synchronization, the receiver correlates the signal with the periodic spreading sequence using integration intervals that extend over an integer number of spreading sequence periods, and processes the results in order to detect the position of the data bit edges.

The classic algorithm for GPS data bit synchronization is the histogram method [2][8]. This method searches for sign changes in consecutive 1 ms correlation results. The performance is adequate for carrier-to-noise-density C/N_0 (which is a quantity related to the signal-to-noise ratio) ratios above 30 dB, which is the normal operating condition for most outdoor GNSS receivers. Because of its simplicity, this method has been extensively used for general purpose embedded receivers.

There are other more complex methods that present higher sensitivity, allowing receivers to perform data bit synchronization under extremely low C/N_0 conditions such as those endured by GPS receivers for indoor applications and street level car receivers. These algorithms work by finding the bit edge candidate position that maximizes the recovered average bit energy [6][7][10], which is equivalent to choosing the maximum likelihood candidate [6]. These methods can work with C/N_0 levels down to 12 dB [7].

Slightly modified versions of these algorithms can be used for GLONASS. The modifications are necessary because

 ISBN: 978-1-61208-264-6

GLONASS uses Manchester coding for its data bits instead of bipolar NRZ.

Both the histogram and the energy maximization algorithms need to work on correlation samples obtained using 1 ms integration times in order to determine the bit alignment with millisecond level resolution. This means that the phase and code tracking loops in the receiver must be updated at a rate of 1 kHz in order to determine the correlation parameters (carrier initial phase and frequency, spreading sequence initial phase and chip rate) that need to be configured at the start of each correlation. This update rate is higher than the update rate typically used during later processing stages (100 Hz), but the amount of processing per update is roughly the same in both cases. Thus, the synchronization stage of GNSS receivers that use these algorithms represents an important fraction of the worst-case processor load of the design. This worst-case processor load is an important metric for real-time systems since it determines whether the system will be able to fulfil all of its processing deadlines in due time [5]. Also, since the synchronization stage represents a very small portion of the total processing time of a given GNSS signal, using the histogram, the bit energy maximization, or any other method that works on 1 ms correlation samples can lead to receiver designs with high peak-to-mean processor load ratios.

The worst-case processor load for a given design can be reduced using data bit synchronization algorithms that can achieve millisecond resolution using multi-millisecond correlation samples that require lower tracking loop update rates. This improvement in the worst-case processor load should not come at the expense of a decrease in the reliability of the synchronization algorithm.

In a previous work [11], a 3 ms maximum likelihood bit synchronization algorithm was proposed. The algorithm was simulated and compared against two other methods (histogram and a maximum bit energy algorithm similar to the one shown in [6]) on the grounds of error rates of each method for fixed size observation intervals.

The present paper extends these results in two ways. First, it generalizes the proposed method to N-millisecond correlation samples, providing a set of tools to help the design of the Trellis diagram that guides the synchronization state machine transitions. Second, this paper provides a simple analytical expression that can be used to estimate the synchronization error rate of the algorithm, and identifies its most important design parameters.

It is important to mention that while our previous work was aimed at achieving bit synchronization of 50 bps data signals of GLONASS and GPS, the present paper focuses on bit synchronization of a generic 100 bps bipolar NRZ. This is because both GPS and GLONASS signals can be thought as 100 bps bipolar NRZ signals whose data bits are encoded with a repetition code, and thus this 100 bps synchronization can be used as the first stage of a full 50 bps GPS/GLONASS bit synchronization algorithm. This is the approach used in a dual system GPS/GLONASS receiver that is being developed by the GNSS group in the Facultad de Ingeniería of the Universidad Nacional de La Plata.

The rest of this paper is organized as follows. Section II presents a basic baseband signal model that can be used to work with N-millisecond correlation samples and enunciates a few base assumptions. Later, the fundamental ideas of the maximum likelihood synchronization method are presented. Section III presents several simple rules to automatically build the synchronization Viterbi state machine for any given value of N. These rules were developed in order to code the simulations that were in turn used to validate the analytical expression of the probability of synchronization error that is introduced in Section IV. Simulation results are compared against theoretically calculated values of the probability of synchronization error in Section V. Finally, the conclusion is in Section VI.

II. ALGORITHM

A. N-millisecond Correlation Samples Model

The following sequence $I_1[i]$ can be used as the model of 1 ms correlation values produced by a GNSS receiver when processing a signal with data encoded as a sequence of 100 bps bipolar NRZ symbols.

$$I_1[i] = B[\lfloor (i+m)/10 \rfloor] + n_1[i], \quad (1)$$

where $B[n]$ is a random process that models the random bit sequence ($B[n] = \pm 1$), m is the unknown initial bit alignment (in milliseconds), $n_1[i]$ is random Gaussian random variable, independent for each i, and such that $E\{n_1[i]\} = 0$, $Var\{n_1[i]\} = \sigma_1^2$.

This model assumes that the beginning of the 1 ms correlation intervals are aligned so that they differ from each and every data bit edge by an integer number of milliseconds. This is a safe assumption since typically GNSS receivers are free to arrange the correlation intervals in the most convenient way, and the 1 ms correlation interval duration fits an integer number of times within the bit duration.

The previous model also requires some sort of normalization of the amplitude of the samples so that $E\{|B[n]|\} = 1$.

Samples generated when using N-millisecond correlation times can be modeled as

$$I_N[j] = \sum_{a=0}^{N-1} I_1[N\,j + a]. \quad (2)$$

Based on the definition of $I_1[i]$

$$I_N[j] = S[j] + n_N[j], \quad (3)$$

where $n_N[j] = n_1[Nj] + ... + n_1[Nj + N - 1]$ is also a Gaussian random variable such that $E\{n_N[i]\} = 0$, and $Var\{n_N[i]\} = N\sigma_1^2$. The term $S[j]$ is the integrated value of the data signal during the N-milliseconds interval. It can

 ISBN: 978-1-61208-264-6

be seen that depending on the presence and position of a data bit sign change during the correlation interval, the value of this term will be $S[j] = \pm(N-2k)$, where $k \in [0, N]$ is the position of the data bit sign change in milliseconds, relative to the start of the integration time.

B. Synchronization

In this section, we will skim over the main ideas of the synchronization algorithm since they were already discussed in [11].

Given a data bit sequence $B[n]$ and an alignment m, the sequence of N-millisecond correlation values $S[j]$ that will be observed is completely determined. This is also true the other way around: given a sequence of L observed correlation samples $I_N[j]$, the data bit sequence $\tilde{B}[n]$ during the observation interval and the bit alignment $\tilde{m}$ can be estimated if we find the sequence of expected correlation values $\tilde{S}[j]$ that best matches $I_N[j]$.

Using the Maximum Likelihood criterion it can be shown that the highest probability candidate $\tilde{S}[i]$ is the one that minimizes the log-likelihood index J

$$\tilde{S}[i] = \min_{o} J(I_N, S^{(o)}), \tag{4}$$

which is defined as

$$J(I_N, S^{(o)}) = \sum_{a=0}^{L-1} (I_N[a] - S^{(o)}[a])^2. \tag{5}$$

In order to find the maximum likelihood candidate a Viterbi algorithm is used. One state is defined for each possible alignment of the beginning of the next N-millisecond correlation relative to the start of the current bit interval and for each sign. Since there are 10 possible different alignments and two bit values (± 1), 20 states need to be defined. Notice that the size of the state machine is independent of the length of the correlation interval N.

The state numbering scheme that will be used throughout this paper is shown in Figure 1. While any kind of state naming scheme is possible, this scheme is particularly useful because it allow us to enunciate a few very simple rules to automate the creation of the state machine transitions for any correlation length N.

There are $20+2N$ transitions in this state machine. States that are closer to the start of the bit than a correlation interval length have two possible arrival paths from previous states; the rest is only linked to a single previous state. Figure 2 shows the Trellis diagram for the case when $N = 3$. In Section III, the rules used to automate the creation of this Trellis will be given.

Initially each state has no accumulated quadratic error. For each observed integration value $I_N[j]$, the quadratic errors of the observed values against the expected values along each possible transition within the Trellis are calculated and added to the accumulated quadratic error of the state at the

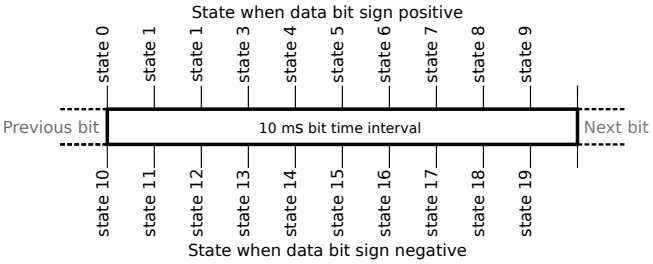

Figure 1. States are defined one for each possible alignment of the beginning of next N-millisecond correlation relative to the start of the current bit interval, and for each possible sign.

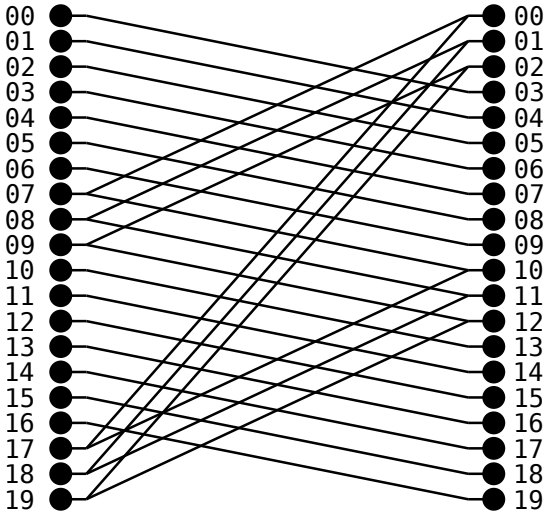

Figure 2. State transition map for $N = 3$.

origin of this transition. If there is a single input path to the destination state of the transition, this updated accumulated quadratic error becomes the accumulated quadratic error of the destination state. If instead there are two possible arrival paths to the destination state, then the path with the highest updated accumulated quadratic error can be safely discarded since it can be anticipated that no matter what the future sequence of observed values is, in the end this candidate sequence will have a total accumulated error higher than at least one other candidate. The surviving path at the merge point then determines the quadratic error of the destination state. This way, at each step $2N$ candidates are eliminated at the merge points in the Trellis, and $2N$ new candidates are created at the fork points. After the last input sample $I_N[j]$ has been processed, the maximum likelihood observed sequence $\tilde{S}[j]$ can be retrieved from the transition history of the candidate with the least accumulated error among the 20 survivors. If only the maximum likelihood alignment estimation is required, all the information needed is in the index number of the state with the least error: if s is the state number with the least error, then at the start of the next correlation interval $mod(s, 10)$ milliseconds will have

 ISBN: 978-1-61208-264-6

passed after the last bit edge position.

III. Trellis Construction Rules

Because of the regularity of the state transitions, the Trellis for any value $N \in [2, 10]$ can be generated using a few very simple rules.

Let *st* be the state number, using the same numbering scheme shown in Figure 1. Each state has at least one input transition that comes from the st_{ss}-*th* state

$$st_{ss} = mod(10 + st - N, 10) + 10\lfloor st/10 \rfloor, \quad (6)$$

where mod is the remainder of the integer division. The expected observed value along this transition is

$$E_{ss} = (-1)^{\lfloor st/10 \rfloor} N. \quad (7)$$

If $mod(st, 10) < N$ there is a second input transition, from the st_{ds}-*th* state

$$st_{ds} = mod(st_{ss} + 10, 20). \quad (8)$$

This transition models the observed correlation value when there is a data bit sign change from the previous bit to the current one. Because of the sign change, the integrated areas at each side of the bit edge partially cancel each other, and thus the expected observed value depends on the alignment the the state relative to the bit start

$$E_{ds} = (2\, mod(st, 10) - N)\,(-1)^{\lfloor st/10 \rfloor}. \quad (9)$$

These rules were used to generate the trellis in Figure 2.

IV. Error expression

Figure 3 shows the values of the final accumulated quadratic errors of the 20 states after having processed a signal with carrier-to-noise-density (C/N_0) ratio of 35 dB using 5 ms integrations ($N = 5$). Each state has an associated candidate correlation value sequence that can be recovered from the history of transitions within the Trellis. Pairs of states s and $s+10$ are both associated to candidates with the same bit alignment. These pairs of states also have similar accumulated quadratic errors because of the way the Viterbi algorithm forks and merges candidates as it moves forward.

The state with the least accumulated quadratic error determines the maximum likelihood bit alignment. Accumulated quadratic errors grow higher the farther away we move from the state with the maximum likelihood solution. The reason for this is that the surviving candidates associated to state numbers close to the one with the least error are not random but are in fact very similar to the maximum likelihood candidate. The farther away from the maximum likelihood candidate that we move, the smaller the amount of likeliness, and thus the higher the accumulated error.

This observation about the likeliness of the surviving candidates is not only qualitative. For high enough signal-to-noise ratios, it can be safely assumed that the second

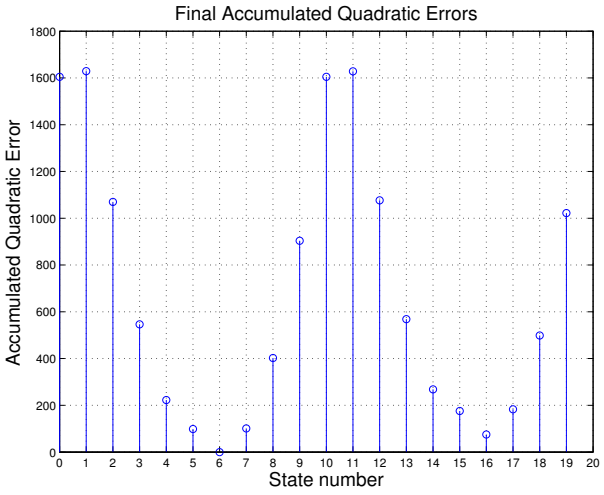

Figure 3. Typical accumulated errors distribution. This plot was generated performing a test run of the simulated algorithm with $N = 5$ and $C/N_o = 35$ dB.

and third most likely alignments are associated to candidate correlation sequences that followed the same bit sequence than the maximum likelihood correlation sequence, but whose bit edges are displaced $\pm$1ms from the true value.

This, in turn, can be used to justify the following statement: the probability of incorrectly identifying the bit edge position using this algorithm is the probability of choosing instead a candidate sequence whose alignment differs by $\pm$1 ms from the correct value.

Let S^α be the correct candidate for the received data bit sequence. Let S^β be the candidate that would have been correct if the data bit sequence was the same, but the bit edges were delayed by 1 ms. The probability of mistakenly choosing S^β over S^α as the maximum likelihood candidate is the probability of the event

$$\begin{aligned} J(I_N, S^\alpha) &> J(I_N, S^\beta) \\ \sum_{a=0}^{L-1} (I_N[a] - S^\alpha[a])^2 &> \sum_{a=0}^{L-1} (I_N[a] - S^\beta[a])^2. \end{aligned} \quad (10)$$

Since the bit sequences that generated S^β and S^α only differ by 1 ms, the sequences S^β and S^α differ only at F sequence values, one for each data bit sign change that occurred (since N $\leq$ 10, there can be at most a single bit sign transition during each correlation interval). Many terms then cancel out, leaving

$$\sum^{F} (I_N[a] - S^\alpha[a])^2 > \sum^{F} (I_N[a] - S^\beta[a])^2. \quad (11)$$

It is easy to see that since the original data bit sequences only differ by a single millisecond, the following equality holds for the remaining terms:

$$S^\alpha[a] - S^\beta[a] = \pm 2, \quad (12)$$

 ISBN: 978-1-61208-264-6

and thus

$$\sum^{F}(I_N[a]-S^{\alpha}[a])^2 \quad > \quad \sum^{F}(I_N[a]-S^{\alpha}[a]\mp 2)^2.$$

Replacing $I_N[a]=S^{\alpha}[a]+n_N[a]$:

$$\begin{aligned}\sum^{F}(n_N[a])^2 &> \sum^{F}(n_N[a]\mp 2)^2\\ 0 &> \sum^{F}(\mp 4n_N[a]+4)\\ \sum^{F}\pm n_N[a] &> F. \end{aligned} \tag{13}$$

$n_N[a]$ are independent gaussian random varibles, thus:

$$P\left\{\sum^{F}\pm n_N[a]>F\right\} \quad = \quad Q\left(\frac{\sqrt{F}}{\sigma_N}\right), \tag{14}$$

where $Q(x)$ is the probability that a Gaussian random variable will obtain a value larger than x standard deviations above the mean.

Finally, since there are two candidates that differ by exactly 1 ms among the surving candidates of the Viterbi processing, the final synchronization error expression is:

$$P_e \quad = \quad 2Q\left(\sqrt{\frac{2\,F\,\frac{C}{N_o}}{1000N}}\right), \tag{15}$$

where in the last expression $\sigma_N^2=N\sigma_1^2$ was replaced by its expression as a function of C/N_0.

It can be seen that the most important parameters in order to determine the synchronization error rate are the number of data bit sign transitions observed F, the length of the correlation interval N and the carrier-to-noise-density C/N_0 ratio of the signal. While the value N is usually imposed by the constraints in other parts of the receiver (e.g. the update rates of the tracking loops), and the C/N_0 ratio is an external constraint imposed on the system by the environment, the designer can choose to increase or decrease the probability of error by choosing the minimum number of bit sign changes that need to be observed during synchronization before deciding the most probable bit alignment of the signal.

Using F as a design variable imposes a compromise between the error rate and the time it takes to perform synchronization. GLONASS signals use Manchester coding, which inserts a forced sign transition during the bit time. Thus it is safe to expect between 50 and 100 bit sign changes each second. GPS, on the other hand, encodes the bits using NRZ; because of this the expected data bit sign changes will be in the range between 0 and 50 each second.

V. Simulations

Figure 4 shows the probability of synchronization error as a function of the correlation integration length N for $N=2,3,5,10$ and the signal carrier-to-noise-density ratio, C/N_0. The values of probability of error calculated using (15) are also shown in the same figure for comparison. For these simulations, random 100 bps BPSK bit sequences were simulated, each one with F bit sign transitions and random initial edge alignments. The value of F was chosen to be 25, which is often taken as the expected number of bit sign transitions during each second for GPS signals (the expected number for GLONASS is 75).

It can be seen that the theoretical values predicted by (15) match the probability of error obtained during simulations for values of C/N_0 higher than 27 dB. This range includes the operating range for most outdoor GNSS receivers. Theoretical and simulated curves start to differ for values below that because, as the signal-to-noise ratio drops, the base hypothesis about the probability of incorrectly identifying the bit edge position being equal to the probability of mistakenly choosing a candidate whose alignment differs by ± 1 ms from the correct value stops being reliable.

VI. Conclusion

This paper introduced a new maximum likelihood bit synchronization algorithm that can be tailored to be used with different types of GNSS signals (GPS, GLONASS). A preliminary version of this work was presented in a previous paper by the same authors. In that paper, it was shown that this method allows to perform bit synchronization using 3 ms correlation interval samples, while at the same time it improves the probability of error compared to the histogram method.

The present paper expands our previous work by exploring the use of different correlation lengths N. As a test case, we work on the bit synchronization of a 100 bps NRZ signal, since that is the kind of synchronization that is used during the first stage of bit edge disambiguation phase of a dual-system GPS/GLONASS receiver being developed in the Facultad de Ingeniería of the Universidad Nacional de La Plata.

An analytical expression to calculate the probability of synchronization errors is also provided in this paper. This expression relates the probability of error to the different parameters of the algorithm, providing the designer with valuable information during the development and testing stage of a receiver. The expression was verified using simulations, and proved to be accurate in typical use scenarios.

It is important to state that the algorithm itself and the results herein presented are in no way limited to the kind of codification and data rate presented in this paper. If a designer found more convenient to use specialized algorithms for each type of signal (50 bps NRZ GPS and 50 bps Manchester coded GLONASS signal) on a dual-system receiver, or in the design of an only GPS or only GLONASS receiver, the results provided in this paper could be reused with only slight modifications, e.g., using larger

 ISBN: 978-1-61208-264-6

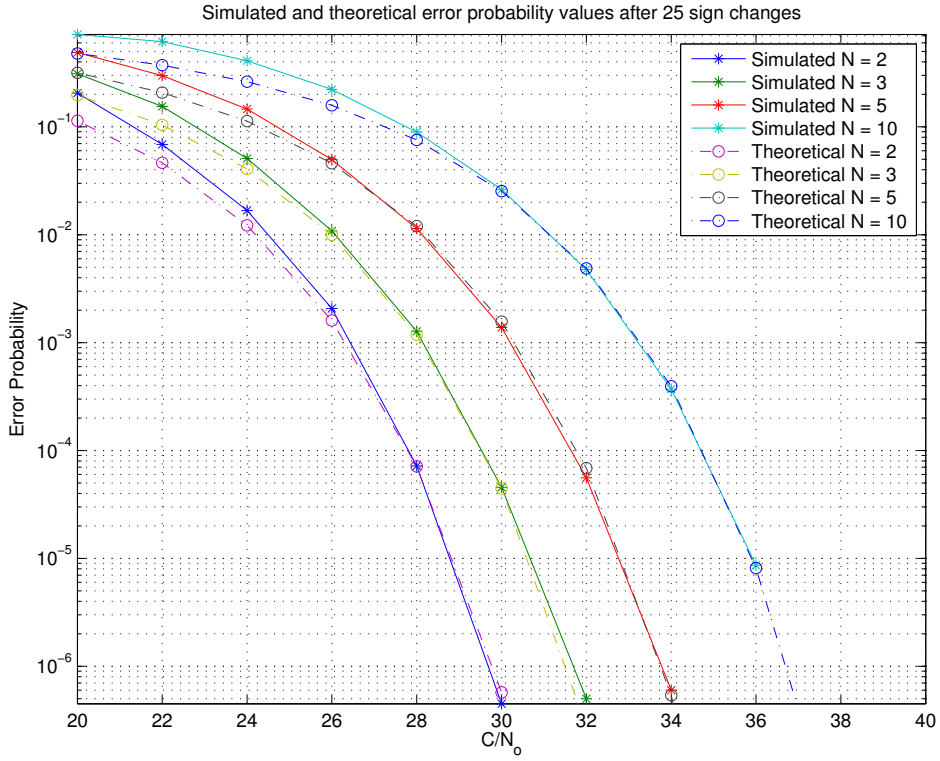

Figure 4. Probability of synchronization error for $F = 25$, and correlation integration lengths $N = 2$, $N = 3$, $N = 5$, $N = 10$. In solid line: simulation results; dashed lines: theoretical values using (15).

state machines (40 states for 50 bps signals) and specialized state machine transitions for each GPS and GLONASS. Such was the approach in our previous work [11].

REFERENCES

[1] E. Kaplan, "Understanding GPS: Principles & Applications". Artech House, 1996.

[2] B. W. Parkinson and J. J. Spilker Jr., "Global Positioning System: Theory and Applications", Volume I. American Institute of Aeronautics and Astronautics (AIAA), 1996.

[3] "NAVSTAR Global Positioning System - Interface Specification IS-GPS-200". NAVSTAR GPS Joint Program Office, 2006.

[4] "Global Navigation Satellite System - GLONASS - Interface Control Document", English edition, version 5.1. Russian Institute of Space Device Engineering, 2008.

[5] C. L. Liu and J. Layland, "Scheduling algorithms for multiprogramming in a hard real-time environment". Journal of the ACM Journal of the ACM (JACM), ACM New York, NY, USA, January 1973, vol. 20, issue 1, pp. 46-61.

[6] M. Kokkonen and S. Pietila, "A New Bit Synchronization Method for a GPS Receiver". In: Position Location and Navigation Symposium, 2002 IEEE, Palm Springs, California, April 2002, pp. 85-90.

[7] Tao Z. and Gannan Y., "A New Bit Synchronization Method for an Ultra-Tightly Integrated GPS Receiver". In: Second International Conference on Information and Computing Science (ICIC '09), Manchester, England, May 2009, vol. 1, pp. 239-242.

[8] Sichao L., Jinhai S., Jinhai L., and Yuepeng Y., "A modified histogram bit synchronization algorithm for GNSS receivers". In: 2nd International Conference on Information Science and Engineering (ICISE), Hangzhou, China, December 2010, pp. 1720-1723.

[9] M. Anghileri, T. Pany, Jong-Hoon W., and G. W. Hein, "An Algorithm for Bit Synchronization and Signal Tracking in Software GNSS Receivers". In: the 19th International Technical Meeting of the Satellite Division (ION GNSS 2006), Institute of Navigation, Fort Worth, Texas, USA, September 2006, pp. 1836-1848.

[10] N. I. Ziedan and J. L. Garrison, "Bit Synchronization and Doppler Frequency Removal at Very Low Carrier to Noise Ratio Using a Combination of the Viterbi Algorithm with an Extended Kalman Filter". In: Proceedings of the 16th International Technical Meeting of the Satellite Division of The Institute of Navigation (ION GPS/GNSS 2003), Portland, Oregon, USA, September 2003, pp. 616-627.

[11] G. L. Puga, P. A. Roncagliolo, and J. G. Garcia, "Low Computational Cost GNSS GPS/GLONASS Maximum Likelihood Bit Synchronization Method". In: Proceedings of the 13th Argentine Symposium on Technology (JAIIO/AST 2012), La Plata, Buenos Aires, Argentina, August 2012, pp. 204-215.

 ISBN: 978-1-61208-264-6

Turbo Decoder VLSI Architecture with Non-Recursive max* Operator for 3GPP LTE Standard

Ashfaq Ahmed, Maurizio Martina, Guido Masera
Department of Electronics & Telecommunication
Politecnico di Torino
Torino, Italy
Email: {ashfaq.ahmed, maurizio.martina, guido.masera}@polito.it

***Abstract*—This paper presents a highly parallel turbo decoder architecture for 3GPP LTE standard with a new non-recursive max* operator. High parallelism is introduced at several levels to achieve high throughput, to meet LTE requirements. The decoder supports all codes specified by LTE and features low complexity, obtained by using the new non-recursive max* operator. The decoder achieves a maximum throughput of 376.4 Mbps at 250 MHz, occupying an area of 1.62 mm^2 on 90-nm Standard Cell ASIC technology . The decoder shows better decoding efficiency (Bits/Cycle/Iterations) and throughput to area ratio (Throughput/mm^2) than many of the previously implemented decoders.**

***Keywords*—3GPP LTE; iterative decoding; parallel turbo decoder; VLSI architecture**

I. INTRODUCTION

Turbo codes [1] have gained huge attention in the last twenty years. Indeed Turbo codes achieve Near Shannon limit capacity, excellent error correction performance, intrinsic parallelism and high coding gain which made them an eligible candidate for a large number of wireless communication standards e.g., WiMax [2], 3GPP LTE [3], UMTS-LTE [4], CCSDS [5]. LTE (Long Term Evolution) is the next step forward in cellular 3G and 4G services. It is designed to meet carrier needs for high speed data and media transport as well as high capacity voice support. The standard specifies data rates up to 100 Mbps in the down-link (two MIMO channels), 50 Mbps in the up-link (single channel) and 20 MHz bandwidth channel.

VLSI implementation of turbo decoders is a challenging task because of high throughput constraints of the standards. A lot of research has been carried out to implement efficient decoders satisfying area, speed and power constraints [6][7][8]. Typically two SISO (Soft Input Soft Output) processors are concatenated in parallel in order to achieve high throughput. Parallelism can be introduced in the decoding process at several levels to improve decoding speed [9] e.g., using multiple processors, exploiting the trellis representation parallelism to decode a set of bits, internal parallelization by using multiple windows in each processing element [10], which eventually reduces the latency. However, highly parallel architectures introduce high complexity in terms of hardware and logic. In the proposed decoder architecture, several of previously mentioned methods have been adopted to improve throughput, along with a novel implementation of non-recursive max* operator [11]. In the non-recursive max* implementation the complexity and overhead of the operator is reduced by computing the *n*-input max* as a whole instead of recursively applying the 2-input max* operation. In the low complexity max* operator, the two maximums are calculated and using the two outputs, the final maximum is found.

The remainder of the paper is organized as follows. Section II describes the code adopted in LTE. In this section the explanation of BCJR algorithm, that is the core of turbo decoding, is given. Section III details the proposed architecture including the overview of the main modules, focusing on the novelty in the architecture i.e., the non-recursive max*. The implementation results along with the comparisons are shown in Section IV. Finally, the whole architecture is concluded in Section V.

II. LTE TURBO CODES AND DECODING ALGORITHM

The 3GPP LTE turbo codes are based on the parallel concatenation of two 8-state Convolutional Codes (CCs) and one Quadratic Polynomial Permutation (QPP) interleaver [12]. The constituent code used in 3GPP LTE is a single binary systematic CC. The generated input frame is fed into the convolutional encoder of rate 1/3. An information sequence $\underline{u}$ is encoded by a convolutional encoder, and an interleaved version of u is encoded by a second convolutional encoder. The initial values of the shift registers of the 8-state constituent encoders are all zeros. After encoding of the current frame, termination is performed: during the last three cycles of the frame, values are input into the encoder to force it to the zero state. The total number of output bits generated by the encoder is $L = 3 \cdot K + 12$, where $40 \leq K \leq 6144$ is the frame length. The last 12 bits are the trellis termination bits.

A. Decoder

The main processing elements inside each decoder are the Soft-In–Soft-Out (SISO) modules [13] which executes the Bahl–Cocke–Jelinek–Raviv (BCJR) algorithm [14], usually in its logarithmic form [15]. The SISO module processes the intrinsic log-likelihood ratios (LLRs), received from the channel, of a coded symbol c and calculates the extrinsic information for the information bits u. The LLRs are exchanged by the SISO modules through the interleaving/deinterleaving permutation laws Π /Π^{-1}. The output extrinsic LLR of symbol u at the kth step is computed as

 ISBN: 978-1-61208-264-6

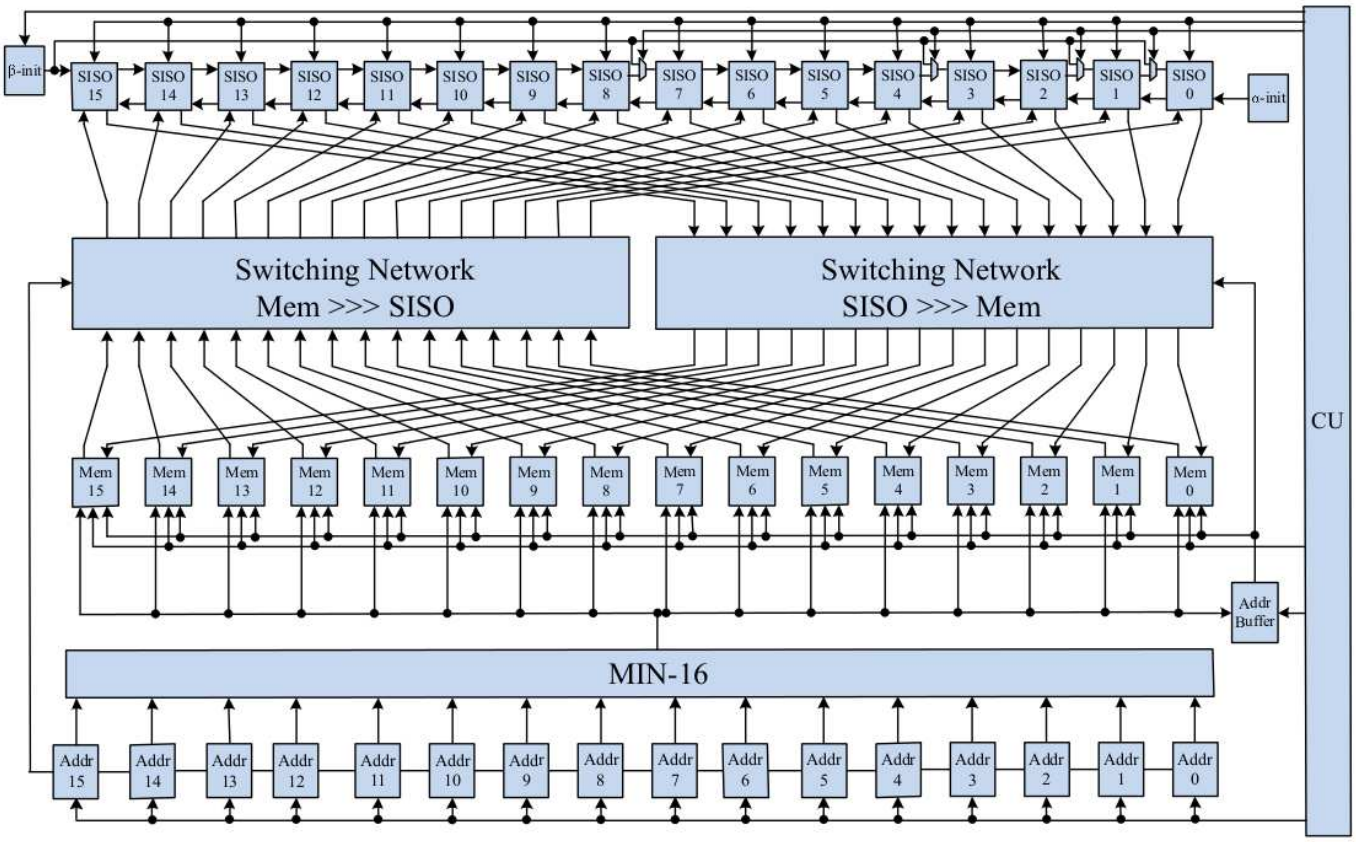

Figure 1. Complete Turbo Decoder

$$\lambda_k^{ext} = \delta \left(\max_{R_1}^{*} \{b\} - \max_{R_0}^{*} \{b\} - \lambda_k^{apr} \right) \quad (1)$$

where $\delta = 0.75$ is a scaling factor [16]. The trellis transition for input equal to '0' is represented by R_o, whereas the trellis transition due to input equal to '1' is represented by R_1. The $\max_{R_x}^{*}$ finds transitions with maximum probability w.r.t. input equal to x, where $x \in \{1,0\}$. λ_k^{apr} is the a-priori information received from the other SISO module, whereas λ_k^{ext} is the extrinsic information generated by the SISO at trellis step k and it is transferred to the other SISO module by means of the interleaver memory. b is defined as,

$$b(k) = \alpha_{k-1}(s) + \gamma_k \left(s, s' \right) + \beta_{k-1} \left(s' \right) \quad (2)$$

$$\alpha_k \left(s' \right) = \max_{s}^{*} \left(\alpha_{k-1}(s) + \gamma_k \left(s, s' \right) \right) \quad (3)$$

$$\beta_{k-1}(s) = \max_{s}^{*} \left(\beta_k \left(s' \right) + \gamma_k \left(s, s' \right) \right) \quad (4)$$

$$\gamma_k \left(s, s' \right) = y_k^s + \lambda_k^{apr} + y_k^p \quad (5)$$

where α and β are known as forward and backward state metrics and are calculated during forward and backward recursions, while γ is the branch metric and is calculated for each transition. SISO takes the following steps to calculate extrinsics and the output bits:

1) It calculates γ for the trellis section k using the systematic and parity channel LLRs and the a-priori information coming from the other SISO, as in (5).
2) From the calculated γ, it computes α by adding the previous α to the corresponding γ. So (3) can be expanded as,

$$\alpha_k = \max^{*} \left(\alpha_{k-1}^1 + \gamma_1, \alpha_{k-1}^2 + \gamma_2 \right) \quad (6)$$

3) β is calculated in the same way like α, but in this case the recursion is in reverse direction (see (4)).
4) After calculating α, β and γ, the final step is to calculate the extrinsic information and the decoded bit value, as in (1) and (2). The calculated extrinsics are passed to the other SISO by means of interleaver memory, while the decoded bit is stored in the decoded bits memory after a certain number of iterations.

III. Proposed Architecture

The current 3GPP LTE standard features native code rate of 1/3, while higher code rates can also be achieved through external rate matching. All the block sizes are even numbers and are divisible by both 4 and 8 , besides all the block sizes greater than 512, 1024 and 2048 are also divisible by 16, 32 and 64 respectively [17]. The complete architecture is shown in Fig. 1.

The major modules of the decoder are: (i) the 16 SISO processors, which execute the BCJR algorithm, (ii) the 16 memories storing the extrinsic values, (iii) two 16x16 switching

 ISBN: 978-1-61208-264-6

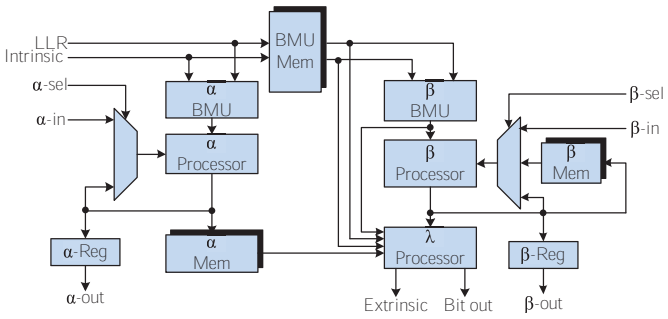

(a) SISO Processor

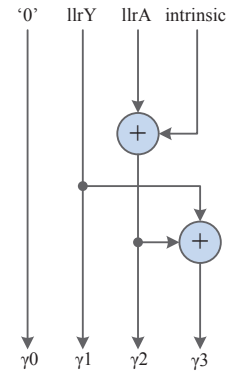

(b) α or β Branch Metric Unit (BMU)

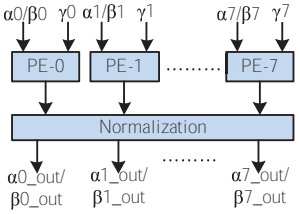

(c) α and β State Metric Unit

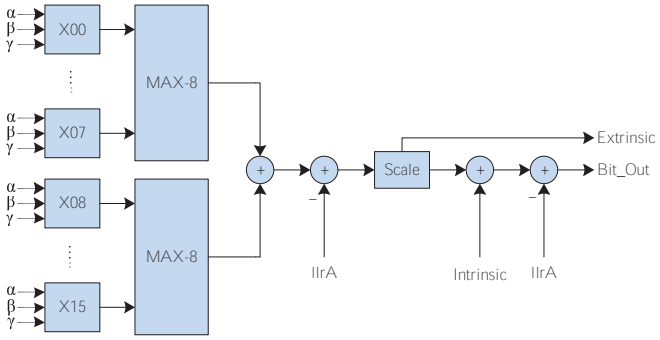

(d) λ-Processor

Figure 2. SISO Processors and Its Major Modules

networks for data transfer from processors to memories and from memories to processors, (iv) the address generator which generates addresses using (7) and (v) the control unit. 3GPP LTE standard uses QPP (Quadratic Permutation Polynomial) [12], which has been proved to be contention free. The QPP interleaver of size N can be expressed as,

$$f(x_o) = \left(f_1 \cdot x_o + f_2 \cdot x_o^2\right) \bmod N \qquad (7)$$

The details of the interleaver are shown in [18], where all the addresses are generated on-the fly for any parallelism factor and f_1 and f_2 are given in the standard and their value depends on the block size N [17]. The decoder is designed to support the maximum code length i.e., N=6144. The maximum depth of the extrinsic memories is N/P, where N=6144 and P=16. On each clock cycle the address generators output 16

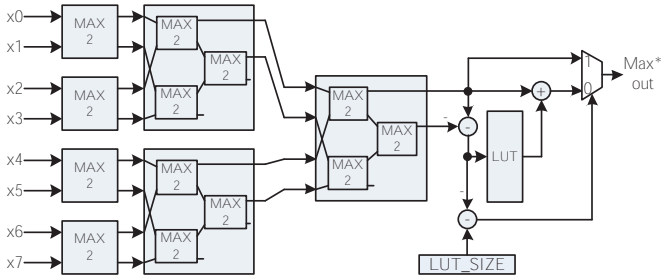

Figure 3. Non-recursive max* module with 8 inputs

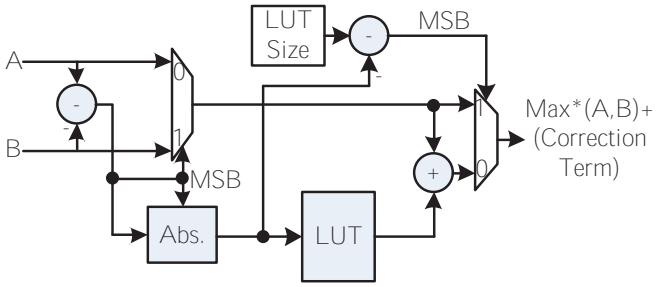

Figure 4. Non-recursive max* module with 2 inputs

addresses and the minimum of these 16 address is calculated through MIN-16 block, which is the effective address for each extrinsic memory. During the forward recursion, all generated addresses are also stored in the *AddrBuffer*, which is a LIFO of W height, where W is the maximum window length. After forward recursion through one complete window, the backward recursion is started and also on the same time the SISO produces the extrinsics, which are passed to the memories through the switching matrix. The address for the write operation (in the extrinsic memories) is always taken from the *AddrBuffer.*

α-init and β-init modules calculate and hold the initial values of α and β. The encoder always starts from all-zero state, which implies that α-init is a pre-computed value, while for β, three tail bits are used with a backward recursion to calculate the value of β at $N-1$ state.

The batcher sorters [19] are used to manage the switching data from SISO to memory and from memory to SISO [20]. The switching matrix takes the data, coming from a memory bank, and the address, generated by the corresponding *Addr* generator, and it sorts the data w.r.t. the addresses. Two switching matrix are used in order to have parallel read and write operations.

There are 16 SISO processors, where each processor passes the α and β to the neighboring SISO, as suggested in [6]. The β-in for the first, second, fourth and eights is multiplexed with either the β-out of the neighboring SISO or from the β-init module. The SISO processors will be discussed in detail in the next section.

The control unit enables the decoder to work for different code lengths. Each code length is associated to a parallelism degree that can be 1,2,4,8 and 16. For example, it enables only 1 SISO processor and only one address generator when the smallest block size is selected. Similarly, the select signals for

 ISBN: 978-1-61208-264-6

Table I. QUANTIZATION

	No. of bits
Channel LLRs λ^s, λ^p	6
Ext./Intrinsics $\lambda^{int.}$	8
Branch metrics γ	12
State Metrics α, β	12

the multiplexers at the inputs of α and β processors are sent by the control signal, in order to pass the correct $\alpha's$ and $\beta's$ to the processors at the end of one N/P bits and $N/(P/NWP)$ bits respectively. Similarly, the control unit is adaptive enough to generate control signal for the data path in order to have correct operation scheduling.

A. SISO processor

The SISO, shown in Fig. 2, is the main processing unit in turbo decoding. In this work, 16 parallel SISO processors are employed, each of which implements (1) to (5) to calculate the extrinsic values and the output bits. The complete architecture of the SISO unit is shown in Fig. 2. Each SISO gets channel LLRs i.e., systematic and parity, the apriori information from memories and the starting state metrics for α and β recursions from other SISOs. The incoming frame is divided in *P* input buffers, where *P* is the number of SISOs. Each SISO decodes the corresponding input bits. So each SISO works on $\frac{N}{P}$ bits, where *N* is the block size. According to Fig. 2, the SISO performs the following decoding operations:

1) The α-BMU (Branch Metric Unit) calculates the γs' (branch metrics) combining the LLRs and the apriori information using (5). At the same time, the BMU-MEM stores all the incoming LLRs and the intrinsic information. BMU-MEM is a LIFO memory. The architecture of the BMU is shown in Fig. 2b.
2) After each calculation of α-BMU, the α-processor calculates the 8 new αs' using previous α and the γ coming from BMU. Eight processing elements (PE-0 ... PE-7) execute in parallel following (3). The new αs' are normalized subtracting the maximum from each of them. Finally the calculated αs' are stored in the α-MEM, which is a LIFO memory as well. The architecture of α-processor is shown in Fig. 2c.
3) When the αs' for a complete window are calculated, the β-BMU and the β-processor start calculating the the $\gamma s'$ and βs' respectively, in the backward direction using (5) and (4).
4) The λ-processor executes in parallel with the β-processor. So after each calculation of a β, the λ-processor calculates the extrinsic, using (1), and also estimates the output bit. The architecture is shown in Fig. 2d.

Each SISO uses three different memories i.e., α-MEM, BMU-MEM and the β-MEM. The α-MEM stores the αs' while traversing the trellis in the forward direction and the BMU-MEM stores the incoming intrinsic and the a-priori LLRs. In Table I, the number of bits required to represent each data managed by the decoder is shown. Table II shows the total memory utilization in the architecture.

Table II. MEMORIES USED IN THE ARCHITECTURE

Unit	Size (kbit)
α−MEM	36.864
BMU-MEM	9.216
β−local-MEM	24.576
Addr. LIFO	0.216
Addr. Init	114.56
Input Buff.	110.592
Output Buff.	6.144
Extrinsic Mem.	49.152
Total	351.32

B. Non-recursive max* operator

The λ-processor executes (1) and (2). In (1), the non-recursive max* operator [11] is used to find the maximum from all the inputs. In general the max* operator is recursive in nature, where on each recursion it finds the maximum from 2 inputs and then the result is compared with the third one and so on. In recursive max* for *n* input values the max* operator is applied recursively *n*–1 times, From (8) it is evident that the max* operator having *n* input values can be computed non-recursively as it requires only knowledge of the maximum among *n* values and an additive correction term depending on the second maximum value among *n* values. The non-recursive max* is implemented to find the two maximum from the 8 inputs using a simple maximum finding tree and a small look-up table (LUT), as shown in Fig. 3. Fig. 4 shows the max* implementation with 2 inputs, which is used in calculation of (3) and (4). The max* operator can be given as

$$\overset{*}{\max_{i=1:n}}(x_i) \simeq \max_{i=1:n}(x_i) + \log\{[1+\exp(-\delta)]\} \tag{8}$$

The $\log\{[1+\exp(-\delta)]\}$ in (8) is the correction term, which is pre-computed and is stored in a small LUT. The difference between the first maximum and the second maximum , namely δ, becomes the address for the LUT. The data from the LUT is then added to the first maximum to find the max* output.

IV. RESULTS

To decrease the amount of memory and to increase the throughput, large number of windows are used for large code lengths. Each SISO processor works with up to 16 windows. In this case, each SISO is decoding 384 bits. The window is 24 bit long. So at each clock cycle, the address generators produce 16 addresses. The data from the memory and the corresponding addresses from the address generators are fed into the permutation network and finally based on the sorting of addresses, the data reaches its destinations [18].

The throughput of the decoder is calculated as in [23]:

$$Throughput = \frac{N \times F}{2.I\left(\frac{N}{P}+W\right)} \tag{9}$$

where *N* is the number of decoded bits, *F* is the clock frequency at which the decoder is synthesized, *I* is the number of iterations, *P* is the number of SISO processors, and *W* is the window length. The BER and FER results, shown in Fig. 5 and Fig. 6 respectively, are obtained with 5 and 9 iterations for code length 6144. Stopping the decoding after 5 iterations

 ISBN: 978-1-61208-264-6

Table III. RESULTS COMPARISONS: Radix/Processor (Rdx/Proc.), CMOS Technology Process (Tech.), Iterations (Iter.), Clock Frequency (Freq.), Memory (Mem), Active Area (Area), Normalized Area (N.A.), Throughput (TP.), Throughput to Area Ratio (TAR = Mbps/mm), Decoding Efficiency (DE = Bits/Cycle/Iterations)

Design	**Proposed**	**[6]**	[7]	[8]	[17]	**[20]**	[18]	[21]	[22]
Standard	LTE	LTE,WiMAX	LTE	LTE	LTE	LTE	LTE	LTE	LTE,WiMAX, DVB-RCS
Rdx./Proc.	2/16	4/8	2/8	2/8	2/64	4/8	2/16	2/32	4/2
Tech (nm)	90	130	90	90	65	130	90	90	65
Iter.	5	8	8	8	6	5.5	5	5.5	6
Freq.	250	250	275	275	400	300	200	486	520
Mem (Kb)	351.32	N/A	N/A	N/A	N/A	129	413.35	N/A	N/A
Area (mm^2)	1.62	10.7	2.10	2.10	8.3	3.57	2.10	13.82	0.644
N.A. (mm^2)	1.62	5.12	2.10	2.10	15.91	1.71	2.10	13.82	1.234
TP. (Mbps)	376.47	187.5	130	129	1310.72	390.6	284.4	1138	170
TAR	232.39	36.62	61.90	61.42	82.83	228.42	135.43	82.34	137.76
DE	7.53	6	3.78	3.75	19.66	7.16	7.11	12.88	1.96

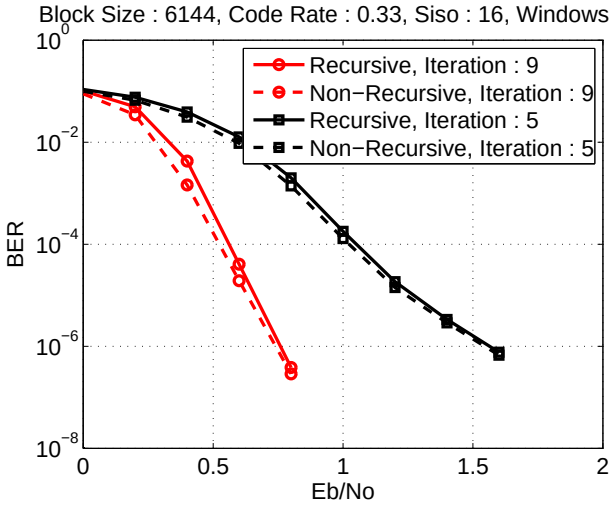

Figure 5. Bit Error Rate (BER), code rate 1/3

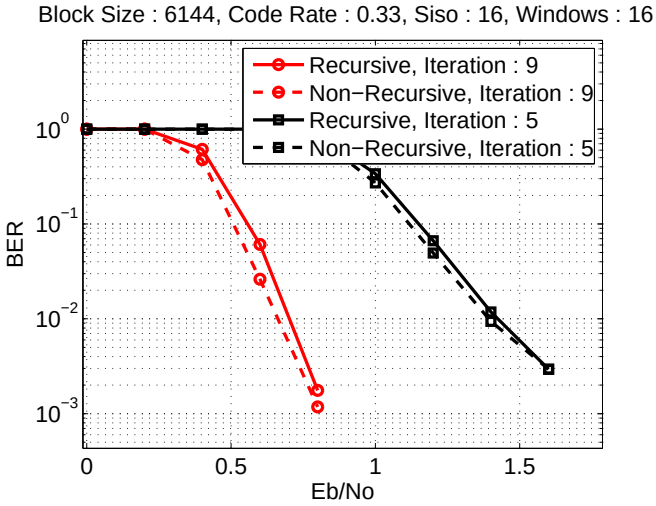

Figure 6. Frame Error Rate (BER), code rate 1/3

instead of 9 introduces a penalty of about 0.5 dB at BER level 10^{-4}, but offers increased throughput and reduced energy dissipation.. It is also shown in Fig. 5 and 6 that the non-recursive max* achieves slight gain over the recursive one.

The synthesis is carried out on Synopsys Design Vision with 90 nm standard cell technology at a clock frequency of 250 MHz. The proposed architecture achieves a maximum throughput of 376.4 Mbps, occupying an area of 1.62 mm^2.

Table III shows the comparison of the proposed architecture with some already published decoders. The comparison is carried out in terms of implementation technology, supported codes and decoded modes, maximum achieved throughput, internal parallelism and occupied area. The area of each implementation is scaled up to 90 nm process technology for fair comparison. The scaling factors of $(\frac{90}{130})^2$ and $(\frac{90}{65})^2$ are used for 130 nm and 65 nm technologies, respectively. A parameter called Throughput to Area Ratio (TAR) [24] is used to evaluate the area efficiency of the designed decoder. Another metric used for comparison purposes is Decoding Efficiency (DE), defined as the number of decoded bits per clock cycle per iteration. DE evaluates the degree of parallelism actually offered by the decoder architecture. As shown in Table III, the proposed architecture achieves better TAR than the other implementations. The DE is better than [6], [7], [8], [20], [18] and [22], whereas [17] and [21] achieve better DE, but they are very expensive architectures, with huge area occupation. So the proposed architecture achieves more than sufficient throughput for 3GPP LTE standard at the cost of lower occupied area than required for most of the alternate solutions.

V. Conclusion

In this paper, an already developed parallel turbo decoder for 3GPP LTE standard is modified with a new architecture of non-recursive max* operator. The analysis shows that with the new max* operator, significant area can be saved and throughput enough to meet the standard requirement can be achieved. The new max* operator is implemented with a very simple logic i.e., by finding just the two maximums and then adding them with a correction term, taken from a LUT.

References

[1] C. Berrou, A. Glavieux, and P. Thitimajshima. "Near Shannon Limit Error-Correcting Coding and Decoding: Turbo-Codes. 1". In *Communications, 1993. ICC '93 Geneva. Technical Program, Conference Record, IEEE International Conference on*, volume 2, page 1064, May 1993.

 ISBN: 978-1-61208-264-6

[2] "IEEE Standard for Local and Metropolitan Area Networks Part 16: Air Interface for Fixed and Mobile Broadband Wireless Access Systems Amendment 2: Physical and Medium Access Control Layers for Combined Fixed and Mobile Operation in Licensed Bands and Corrigendum 1". *IEEE Std 802.16e-2005 and IEEE Std 802.16-2004/Cor 1-2005 (Amendment and Corrigendum to IEEE Std 802.16-2004)*, 2006.

[3] "3GPP TS 36.212 v8.0.0: Multiplexing and Channel Coding". *3rd Generation Partnership Project*, 2007-2009.

[4] "UMTS : Universal Mobile Telecommunications System". http://www.3gpp.org/Technologies/Keywords-Acronyms/article/umts.

[5] "Consultive Committee for Space Data Systems Recommendation for Space Data System Standards TM Synchronization and Channel Coding CCSDS 121.0-B-2", Sep. 2003.

[6] J. H. Kim and I. C. Park. "A Unified Parallel Radix-4 Turbo Decoder for Mobile WiMAX and 3GPP-LTE". In *Custom Integrated Circuits Conference, 2009. CICC '09. IEEE*, page 487, Sept. 2009.

[7] C. C. Wong and H. C. Chang. "Reconfigurable Turbo Decoder With Parallel Architecture for 3GPP LTE System". *Circuits and Systems II: Express Briefs, IEEE Transactions on*, 57(7):566, July 2010.

[8] C. C. Wong, Y. Y. Lee, and H. C. Chang. "A 188-size 2.1mm^2 Reconfigurable Turbo Decoder Chip with Parallel Architecture for 3GPP LTE System". In *VLSI Circuits, 2009 Symposium on*, page 288, June 2009.

[9] G. Masera. "VLSI for Turbo Codes". In Keattisak Sripimanwat, editor, *Turbo Code Applications*, page 347. Springer Netherlands, 2005.

[10] O. Muller, A. Baghdadi, and M. Jezequel. "Exploring Parallel Processing Levels for Convolutional Turbo Decoding". In *Information and Communication Technologies, 2006. ICTTA '06. 2nd*, volume 2, page 2353, April 2006.

[11] S. Papaharalabos, P. T. Mathiopoulos, G. Masera, and M. Maurizio. "Non-Recursive max* Operator with Reduced Implementation Complexity for Turbo Decoding". *Communications, IET*, 6(7):702, May 2012.

[12] "Multiplexing and Channel Coding, 3GPP TS 36.212 Version 8.4.0, September 2008".

[13] S. Benedetto, G. Montorsi, D. Divsalar, and F. Pollara. "Soft-Input Soft-Output Modules for the Construction and Distributed Iterative Decoding of Code Networks". *European Transactions on Telecommunications*, 9(2):155, Sep. 1998.

[14] L. Bahl, J. Cocke, F. Jelinek, and J. Raviv. "Optimal Decoding of Linear Codes for Minimizing Symbol Error Rate (Corresp.)". *Information Theory, IEEE Transactions on*, 20(2):284, Mar. 1974.

[15] P. Robertson, E. Villebrun, and P. Hoeher. "A Comparison of Optimal and Sub-Optimal MAP Decoding Algorithms Operating in the Log Domain". In *Communications, 1995. ICC '95 Seattle, 'Gateway to Globalization', 1995 IEEE International Conference on*, volume 2, page 1009, Jun 1995.

[16] S. Papaharalabos, P. T. Mathiopoulos, G. Masera, and M. Maurizio. "On Optimal and Near-Optimal Turbo Decoding using Generalized max Operator". *Communications Letters, IEEE*, 13(7):522, July 2009.

[17] Y. Sun and J. R. Cavallaro. "Efficient Hardware Implementation of a Highly-Parallel 3GPP LTE/LTE-Advance Turbo Decoder". *Integration, the VLSI Journal*, 44(4):305, July 2010.

[18] A. Ahmed, M. Awais, A. ur Rehman, M. Maurizio, and G. Masera. "A High Throughput Turbo Decoder VLSI Architecture for 3GPP LTE Standard". In *Multitopic Conference (INMIC), 2011 IEEE 14th International*, page 340, 2011.

[19] K. E. Batcher. "Sorting Networks and their Applications". In *Proceedings of the April 30–May 2, 1968, spring joint computer conference*, AFIPS '68 (Spring), page 307, New York, NY, USA, May 1968. ACM.

[20] C. Studer, C. Benkeser, S. Belfanti, and Q. Huang. "Design and Implementation of a Parallel Turbo-Decoder ASIC for 3GPP-LTE". *Solid-State Circuits, IEEE Journal of*, 46(1):8, Jan. 2011.

[21] S. M. Karim and I. Chakrabarti. "High-Throughput Turbo Decoder using Pipelined Parallel Architecture and Collision-Free Interleaver". *Communications, IET*, 6(11):1416, July 2012.

[22] R. Al-Khayat, A. Baghdadi, and M. Jezequel. "Architecture Efficiency of Application-Specific Processors: A 170Mbit/s 0.644mm^2 Multi-Standard Turbo Decoder". In *System on Chip (SoC), 2012 International Symposium on*, page 1, Oct. 2012.

[23] M. Maurizio, M. Nicola, and G. Masera. "VLSI Implementation of Wimax Convolutional Turbo Code Encoder and Decoder". *Journal of Circuits, Systems and Computers*, 18(03):535, Sep. 2009.

[24] G. Masera, F. Quaglio, and F. Vacca. "Implementation of a Flexible LDPC Decoder". *Circuits and Systems II: Express Briefs, IEEE Transactions on*, 54(6):542, June 2007.

 ISBN: 978-1-61208-264-6

A Novel Range-spread Target Detection Algorithm Based on Waveform Entropy for Missile-borne Radar

Bo Liu, Wenge Chang, Xiangyang Li
School of Electronic Science and Engineering, National University of Defense Technology
Changsha, 410073, P.R.China
liubo19830120@163.com, changwenge@nudt.edu.cn, lxyniu@sina.com

***Abstract*—A novel range-spread target detection algorithm in white Gaussian clutter for missile-borne radars is presented. For missile-borne radars, range migration of the target echoes during a coherent processing interval (CPI) is serious, which disperses the echo energy of the target and increases the difficulty of target detection. In this paper, range alignment for target echoes is accomplished in the frequency domain during the process of digital pulse compression. Then a range-spread detection algorithm based on the waveform entropy (WE) of the average combination of high range resolution profiles (HRRP) is addressed, which has the property of constant false-alarm rate (CFAR). Finally, the detection performance is assessed by Monte-Carlo simulation, and the results indicate that the detection performance of the proposed detector is superior to the traditional energy integrator and is robust for different HRRPs of the target.**

Keywords-high range resolution; range-spread; waveform entropy; target detection; CFAR.

I. INTRODUCTION

High range resolution (HRR) radars are widely used in precision guidance in recent years [1], for the echoes of HRR radars involve abundant target information and can be used for target recognition and accurate tracking [2]. For HRR radars, a relatively large target can be assumed to be the composition of multiple physical scatterers which distribute in different range cells in radar echo, so is called a range-spread target [3]. Consequently, traditional point-like target detection schemes for low range resolution (LRR) radars may fail for HRR radars [4]. Many achievements have been made in range-spread target detection during the past decades [5-9] (and references therein). Precisely, range-spread targets detection in white Gaussian noise of a known spectral density level is addressed in [5-6]. In [7], constant false-alarm rate (CFAR) detectors based on a generalized likelihood ratio test (GLRT) for range-spread targets are derived. Adaptive detection of distributed targets has been addressed in [8], with reference to Gaussian disturbance clutter. In [9], CFAR detection of distributed targets in non-Gaussian disturbance modelled as a compound-Gaussian process is studied. Nevertheless, the detection algorithms above do not consider the relative motion between the radar and the target, so they are not applicable in the scenario of moving range-spread target detection. In addition, some of them consume so much computation that they are difficult to implement in engineering.

In this paper, we propose a novel range-spread target detection algorithm for anti-ship terminal guidance HRR radars. Firstly, the range-spread target echo model of a missile-borne HRR chirp radar is established and the range alignment of HRRP is accomplished in the frequency domain. Secondly, the range-spread target detection method based on the waveform (WE) of the radar echo after coherent integration is addressed. Finally, the simulation indicates that the detection algorithm is superior to the traditional energy integrator detector and is robust for different HRRPs of the target. It should be pointed out that the proposed detector based on waveform entropy needs not to estimate the parameters of the clutter, which is a must for many traditional detection algorithms. Moreover, the computational complexity of the detector makes it suitable for missile-borne radar signal processing.

The paper is organized as follows. In Section II, we build and analyze the echo model of a range-spread target for missile-borne HRR radar. In Section III , range alignment of the target echoes is accomplished in the frequency domain. We address the range-spread target detection algorithm in Section IV. And the performance of the proposed method is assessed in Section V. At last, in Section VI, some conclusions are given.

II. RADAR ECHO MODEL

The transmitted signal of a chirp radar is expressed as:

$$s(\hat{t},t_s)=rect\left(\frac{\hat{t}}{T_p}\right)\cdot\exp(j\pi\mu\hat{t}^2)\cdot\exp(j2\pi f_c t)\cdot \qquad (1)$$

where $\hat{t}$ represents fast time; $t_s=mT_r$ is slow time, $m=0,1,...,M-1$, M is the number of pulses for coherent integration, T_r is the pulse repetition interval; $t=\hat{t}+t_s$ is the absolute time; $\mu=B/T_p$ is the frequency slope of chirp pulse, B is the signal's bandwidth, T_p is the pulse width; f_c is the carrier frequency.

According to the radar theory, the echo of a target is the convolution of the transmitted signal with the target range-scattering function. The range-scattering function of a static point-like target at the range of R_0 can be written as [3]:

$$CF_0(t)=a_0\cdot e^{j2\pi\varphi_0}\cdot\delta(t-2R_0/c)\,. \qquad (2)$$

where a_0 is the amplitude, φ_0 is the initial phase, and c is the velocity of light. Thus the range-scattering function of a static range-spread target can be expressed as:

$$CF(t)=\sum_{k=1}^{k=K}a_k\cdot e^{j2\pi\varphi_k}\cdot\delta(t-\tau_k)\cdot \qquad (3)$$

where K is the number of scattering centers of the range-spread target, a_k , φ_k and τ_k are the amplitude, initial phase and delay of the k-th physical scatterer of the range-spread target in range cell, respectively.

 ISBN: 978-1-61208-264-6

Assuming that the radar is working on tracking condition and moving towards the target at sea, and the radial velocity between the radar and the target remains constant during a coherent processing interval (CPI). Accordingly, the instantaneous range between the radar and the target is:

$$R_k(t_s) = R_{k0} - v \cdot t_s, k = 1, 2, ...K. \quad (4)$$

where $R_k(\cdot)$ represents the instantaneous range of the k-th scatterer of the range-spread target, R_{k0} is the initial range of the k-th scatterer and v is the radial velocity between the radar and the target. Substituting (4) into (3), the instantaneous range-scattering function of a range-spread target is obtained:

$$\begin{aligned} CF(t, t_s) &= \sum_{k=1}^{k=K} a_k \cdot \mathrm{e}^{j2\pi\varphi_k} \cdot \delta\left[t - \frac{2R_k(t_s)}{c} \right] \\ &= \sum_{k=1}^{k=K} a_k \cdot \mathrm{e}^{j2\pi\varphi_k} \cdot \delta\left[t - \frac{2(R_{k0} - v \cdot t_s)}{c} \right]. \end{aligned} \quad (5)$$

Therefore, the radar echo of the range-spread target is expressed as:

$$\begin{aligned} r(\hat{t}, t_s) = \sum_{k=1}^{k=K} a_k \cdot \mathrm{e}^{j2\pi\varphi_k} \cdot rect\left[\frac{\hat{t} - 2(R_{k0} - v \cdot t_s)/c}{T_p} \right] \\ \cdot \exp\left\{ j\pi\mu\left[\hat{t} - 2(R_{k0} - v \cdot t_s)/c \right]^2 \right\} \\ \cdot \exp\left\{ j2\pi(f_c + f_d)\left[t - (R_{k0} - v \cdot t_s)/c \right] \right\}. \end{aligned} \quad (6)$$

where $f_d = 2vf_c / c$ is the Doppler frequency. After mixing and low-pass filtering, the baseband target echo is written as:

$$\begin{aligned} r_{baseband}(\hat{t}, t_s) = \sum_{k=1}^{k=K} a_k \cdot \mathrm{e}^{j2\pi\varphi_k} \cdot rect\left[\frac{\hat{t} - 2(R_{k0} - v \cdot t_s)/c}{T_p} \right] \\ \cdot \exp\left\{ j\pi\mu\left[\hat{t} - 2(R_{k0} - v \cdot t_s)/c \right]^2 + \underbrace{j2\pi f_d t}_{\text{time-frequency coupling}} \right\} \\ \cdot \exp\left\{ -j4\pi f_c (R_{k0} - v \cdot t_s)/c \right\}. \end{aligned} \quad (7)$$

From (7), it can be seen that the relative radial velocity between the radar and the target produces time-frequency coupling to the chirp signal [10], which results in mismatching between the target echo and the matched filter. After matched filtering, HRRPs of the range-spread target can be written as:

$$\begin{aligned} y(\hat{t}, t_s) = \sum_{k=1}^{k=K} a_k \sqrt{\mu T_p^{\,2}} \cdot rect\left[\frac{\hat{t} - 2(R_{k0} - v \cdot t_s)/c}{T_p} \right] \\ \cdot \frac{sin\left\{ \pi B_c \left[\hat{t} - \frac{2(R_{k0} - v \cdot t_s)}{c} - \frac{f_d}{\mu} \right] \cdot \left[1 - \frac{\left| \hat{t} - 2(R_{k0} - v \cdot t_s)/c \right|}{T_p} \right] \right\}}{\pi B_c \left[\hat{t} - \frac{2(R_{k0} - v \cdot t_s)}{c} - \frac{f_d}{\mu} \right]} \\ \cdot \exp\left[j2\pi(\varphi_k + \frac{1}{8}) \right] \cdot \exp\left(-j4\pi f_c \cdot \frac{R_{k0} - v \cdot t_s}{c} \right) \\ \cdot \exp\left\{ -j\pi\mu\left[\hat{t} - \frac{2(R_{k0} - v \cdot t_s)}{c} \right] \right\}. \end{aligned} \quad (8)$$

Due to mismatching, envelops of the pulse compression results in (8) are not sinc functions any more. According to [10], the amplitude loss in (8) is negligible, while the time shift resulting from the time-frequency coupling of chirp signal is significant and will affect range measurement accuracy. From (8), the time shift of the target resulting from the time-frequency coupling of the chirp signal is:

$$\Delta t = f_d / \mu. \quad (9)$$

Additionally, the radial velocity v between the radar and the target produces range migration during a CPI. From (8), the migration time between the adjacent pulses is expressed as:

$$t_m = 2vT_r / c. \quad (10)$$

The range migration factor P is defined as:

$$P = B(M-1)t_m = 2Bv(M-1)T_r / c. \quad (11)$$

The range migration factor P represents the number of the range resolution cells that the target echo spreads during the CPI.

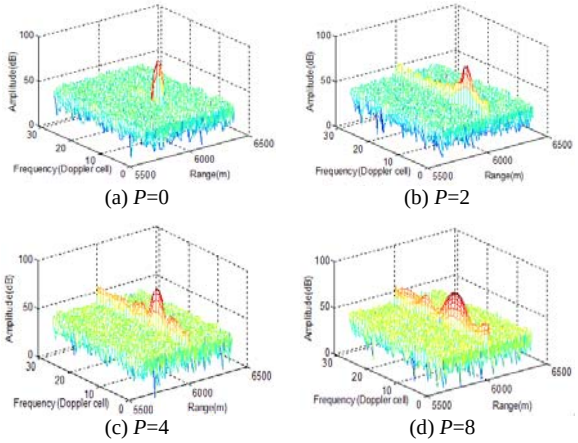

(a) P=0 (b) P=2 (c) P=4 (d) P=8

Figure 1. Range migration effects on coherent integration results. Simulation parameters: $B = 80MHz$, $M = 32$, $T_p = 20\mu s$, $T_r = 250\mu s$, sampling rate $f_s = 120MHz$.

Coherent integration is widely adopted to enhance the signal-to-noise ratio (SNR) of radar echo [11], which improves the target detection performance of the radar system. But when there is high speed relative motion between the radar and the target, the range migration will affect the result of coherent integration. Fig. 1 shows the range migration effects on coherent integration results of a point-like target with range migration factor P=0, 2, 4 and 8, respectively. It can be seen that the range migration disperses the echo energy of the target in coherent integration and so makes it more difficult to target detection.

Assuming it is required that the range migration during the CPI should be no more than half of the range resolution cell [12], according to (11), the radial velocity between the radar and the target should satisfy the following equation:

$$|v| < \frac{c}{4B(M-1)T_r}. \quad (12)$$

III. RANGE ALIGNMENT

For missile-borne radar, equation (12) usually can not be satisfied. Therefore it is necessary to correct the range migration between the HRRPs before coherent integration. Supposing the velocity of the missile v_m can be obtained by the missile-borne inertial navigation system (INS) [13], the velocity measurement error is Δv_m. If we adopt v_m as an estimation of the radial velocity between the radar and the target, the estimation error is:

$$\varepsilon = \Delta v_m + v_t. \quad (13)$$

where v_t is the radial velocity of the target ship. For the time being, the radial velocity estimation error ε generally satisfies (12) and so v_m can be employed to correct the range migration between the HRRPs during a CPI.

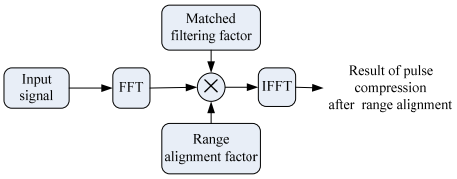

Figure 2. Range alignment during the digital pulse compression

By utilizing the time-frequency symmetry properties of the Fourier transform, range alignment can be accomplished in the frequency domain. Firstly, transform the pulse compression results in (8) to the frequency domain by the Fourier transform (FT) in the fast time dimension. Then multiply them by the corresponding the frequency domain phase terms related to the radial velocity estimation v_m. Finally, transform the products to the time domain by the inverse Fourier transform (IFT) and the result of range alignment is obtained:

$$y'(\hat{t},t_s)=IFT\left\{y(f,t_s)\cdot\exp\left[j4\pi v_m\frac{(f_c/\mu-t_s)\cdot f}{c}\right]\right\}$$
$$\approx\sum_{k=1}^{k=K}a_k\sqrt{\mu T_p{}^2}\cdot rect\left[\frac{\hat{t}+f_d/\mu-2R_{k0}/c}{T_p}\right]\cdot sinc\left[\pi B(\hat{t}-\frac{2R_{k0}}{c})\right]$$
$$\cdot\exp\left[j2\pi(\varphi_k+\frac{1}{8})\right]\cdot\exp\left(-j4\pi f_c\cdot\frac{R_{k0}-v\cdot t_s}{c}\right)$$
$$\cdot\exp\left[-j\pi\mu\left(\hat{t}-2R_{k0}/c+f_d/\mu\right)\right]\cdot \qquad (14)$$

where $y'(\hat{t},t_s)$ is the HRRPs after range alignment, $y(f,t_s)=FT\left[y(\hat{t},t_s)\right]$, f is the natural frequency. Although the process of the range alignment above needs abundant computation, it does not take much additional time in the signal processing, because it could be accomplished concurrently with digital pulse compression. Fig. 2 is the flow chart of the range alignment scheme during the pulse compression with a digital matched filter.

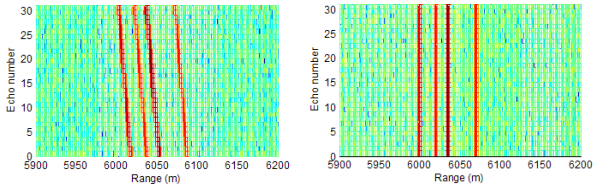

(a) Without range alignment, P=8.27 (b) After range alignment, P=0.041

Figure 3. Top view of target echoes after pulse compression. Radar parameters: $B=80MHz$, $M=32$, $T_p=20\mu s$, $T_r=250\mu s$.

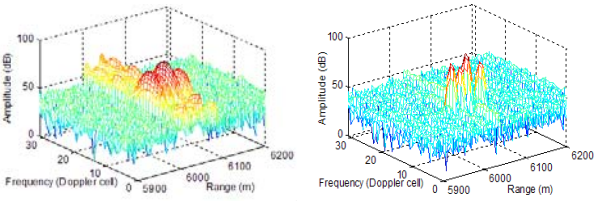

(a) Without range alignment (b) After range alignment.

Figure 4. Coherent integration results of the echoes shown in Fig. 3.

Supposing the velocity of the missile v_m provided by the INS is 2000 m/s, the real radial velocity between the missile and the target v = 2020 m/s, the error of the coarse estimation of the radial velocity ε = 20 m/s. The echoes of a range-spread target with four scattering centers are shown in Fig. 3, the horizontal is the range axis, and the ordinate is the Doppler frequency axis, where Fig. 3 (a) shows the echoes without range alignment, Fig. 3 (b) shows the echoes after range alignment. Fig. 4 shows the coherent integration results of the target echoes before and after range alignment. It can be seen, compared with the coherent integration result without range alignment, the echo energy of the target has been effectively gathered after range alignment.

IV. TARGET DETECTION

After Range alignment and coherent integration, the echo energy of the range-spread target is accumulated effectively. Denoting the data after coherent integration by matrix $Z\{M\times N\}$, where N is the maximum of the range cells number that the desired target spreads. The detection problem can be formulated in terms of the following binary hypotheses test:

$$\begin{cases}H_0: z_m=w_m\\ H_1: z_m=x_m+w_m\end{cases},m=0,1,...,M-1. \qquad (15)$$

where z_m, w_m, x_m are the received signal vector, sea clutter vector, and HRRP of the desired target, respectively. All of them are row vectors with length N, and w_m is assumed to be zero-mean complex white Gaussian noise.

In practical applications, to restraint the side lobe of the Doppler [14], a weighting function is generally adopted during coherent integration, which expands the Doppler of the target echo. Moreover, the target ship may corner sometimes, which expands the Doppler as well. Nevertheless, the maximum number of Doppler cells that the target echo spreads in Doppler axis usually can be known in advance. Setting a sliding-window of width $M_0\cdot r_d$ on the Doppler axis, where M_0 is the max number of the Doppler cell that the target echo may take up, $M_0\le M$, and r_d is the Doppler resolution cell of the radar system. The echo energy within the window is integrated, whichever makes the integrated value of the largest window is chosen as the target detection window, denoted by W. The detection problem can be redescribed as the following binary hypothesis test:

$$\begin{cases}H_0: z_m(n)=w_m(n)\\ H_1: z_m(n)=x_m(n)+w_m(n)\end{cases} \qquad (16)$$
$$m=m_0,m_0+1,...,m_0+M_0-1,n=0,1,...,N-1.$$

where m_0 is the starting Doppler cell number of the target in W. Envelops of the M_0 HRRPs are high correlated, which can be utilised to construct the detector. An average combination of the radar echo within the detection window W is defined by:

$$A(n)=\frac{1}{M_0}\sum_{m=m_0}^{m_0+M_0-1}z_m{}^2(n),n=0,1,...,N-1. \qquad (17)$$

In fact, the average combination defined in the above equation can be seen as incoherent integration of the M_0 echoes. Because of the independence of the clutter for

different echoes, $A(n)$ has higher signal-to-clutter (SCR) than single echo. In other words, $A(n)$ is much sparser than the single echo owing to incoherent integration. Here, the entropy concept is introduced to measure the sparseness of the waveform of $A(n)$, which is named as the waveform entropy (WE) [15]. Entropy is a measure of the uncertainty of random variables [16], in order to adopt the concept of entropy, setting:

$$\begin{cases} p(n) = |A(n)| / \|A\| \\ \|A\| = \sum_{n=0}^{N-1} |A(n)| \end{cases}, n = 0,1,...,N-1. \quad (18)$$

the WE of $A(n)$ is defined as:

$$WE[A(n)] = -\sum_{n=0}^{N-1} p(n) \cdot \log_2 p(n) \cdot \quad (19)$$

According to the definition above, the waveform entropy has the following properties:

(1) $E[A(n)] \to 0$, when $p(n) \to 0$. The sparser $A(n)$ is, the smaller $WE[A(n)]$ is.

(2) $E[A(n)] \le \log_2 N$, the equation comes into existence when $p(n) = 1/N, \forall n = 0,1,...,N-1$. The more homogeneous the distribution of $A(n)$'s energy is, the larger $WE[A(n)]$ will be.

Accordingly, if the energy of a waveform distributes uniformly along its parametric axis, the WE reaches the maximum. On the contrary, if the energy concentrates only on single sampling point of the waveform, the WE is the minimum.

For the average combination of the radar echo $A(n)$, when the target is absent, the energy of the Gaussian clutter echo distributes uniformly, which results in a larger value of $WE[A(n)]$. Whereas, when the target is present, the energy of the target echo appears in a number of isolated range cells, the sparseness of $A(n)$ corresponds to a low value of $WE[A(n)]$. Therefore, the WE of $A(n)$ can distinguish the clutter sequences and target plus clutter sequences effectively. Fig. 5 shows the waveform entropies of $A(n)$ while the target is absent and present, respectively. The horizontal is the trail number, and the ordinate is the waveform entropy.

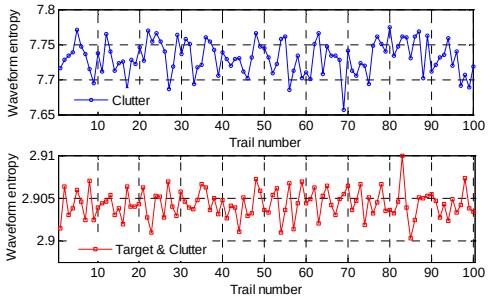

Figure 5. Waveform entropies of $A(n)$ when the target is absent (above) and present (below). Simulation parameters: $M = 32, M_0 = 4, N = 256, SCR = 30dB$.

Thus, the detection statistic of the detector is defined as:

$$R = WE[A(n)] = WE\left[\frac{1}{M_0}\sum_{m=m_0}^{m_0+M_0-1} z_m^2(n)\right] \underset{H_0}{\overset{H_1}{\lessgtr}} T \cdot \quad (20)$$

where T is the detection threshold, $n = 0,1,...,N-1$.

Under the H_0 hypothesis in (16), the detection statistic is written as:

$$R = WE\left[\frac{1}{M_0}\sum_{m=m_0}^{m_0+M_0-1} w_m^2(n)\right], n = 0,1,...,N-1. \quad (21)$$

Setting:

$$q(n) = \frac{\sum_{m=m_0}^{m_0+M_0-1} w_m^2(n)}{\sum_{n=0}^{N-1}\sum_{m=m_0}^{m_0+M_0-1} w_m^2(n)}, n = 0,1,...,N-1. \quad (22)$$

Then, the detection statistic under the H_0 hypothesis is expressed as:

$$R = -\sum_{n=0}^{N-1} q(n) \cdot \log_2 q(n) \cdot \quad (23)$$

Here, we assume the variance of $w_m(n)$ is σ^2. Then, $\frac{1}{\sigma^2} w_m^2(n)$ is in chi-square distribution with freedom 2, namely,

$$\frac{1}{\sigma^2} w_m^2(n) \sim \chi^2(2) \cdot \quad (24)$$

where $\chi^2(l)$ denotes a chi-square distribution with freedom l. Similarly,

$$\frac{1}{\sigma^2}\sum_{m=m_0}^{m_0+M_0-1} w_m^2(n) \sim \chi^2(2M_0), n = 0,1,...,N-1. \quad (25)$$

and,

$$\frac{1}{\sigma^2}\sum_{n=0}^{N-1}\sum_{m=m_0}^{m_0+M_0-1} w_m^2(n) \sim \chi^2(2M_0N) \cdot \quad (26)$$

From (22), (25) and (26), we can obtain:

$$N \cdot q(n) \sim F(2M_0, 2M_0N), \quad n = 0,1,...,N-1. \quad (27)$$

So the probability distribution function (PDF) of $q(n)$ is independent of the clutter variance σ^2. Therefore, from (23), we can find that the detection statistic R under the H_0 hypothesis is also independent of σ^2. Thus, the false alarm probability is independent of the external clutter environment, which implies that the proposed detector in (20) is a CFAR detector.

The Neyman-Pearson criterion is employed to make the judgement. Although the closed-form expression for the false-alarm probability (p_{fa}) is difficult to derive, the threshold for a special false-alarm probability can be obtained by the widely used Monte-Carlo method. While the detection statistic is smaller than the threshold, H_1 hypothesis is selected.

V. PERFORMANCE ASSESSMENT

In this section, we assess the performance of the waveform entropy detector given by (20) resorting to Monte-Carlo simulations. The simulation parameters of the radar are listed in table 1, which are assumed according to the principle in [1].

 ISBN: 978-1-61208-264-6

Fig. 6 shows the HRRPs of two range-spread targets simulated by the computer, where HRRPs of target 1 and target 2 are shown in Fig. 6(a) and Fig. 6(b), respectively. Each of the two targets has four scattering centers, while the distributions of the scattering centers are different.

TABLE I. PARAMETERS OF A HRR CHIRP RADAR

B	T_r	T_p	M	f_s
80 *MHz*	250 μs	20 μs	32	120*MHz*

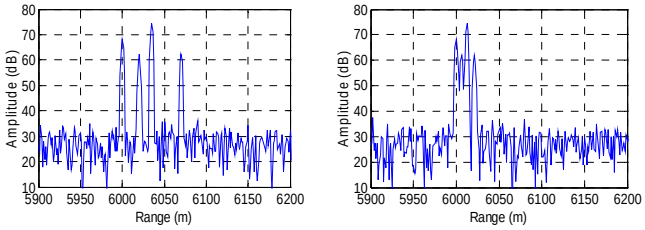

(a) HRRP of target 1 (b) HRRP of target 2

Figure 6. HRRPs of two targets simulated by computer

In the following we compare the performance of the proposed detector based on waveform entropy with the integrator detector [5]. Gaussian clutter is generated by computer, while the variance is adjusted to SCR. Taking the computational complexity into account, we assumed $p_{fa} = 0.0001$, and 1000 independent trials are carried out at each SCR.

Fig. 7 shows the detection performance of the proposed detector based on waveform entropy and the integrator detector. Simulations for target 1 and target 2 are shown in Fig. 7(a) and Fig. 7(b), respectively. It can be seen that the detection performance of the proposed detector is superior to the integrator detector.

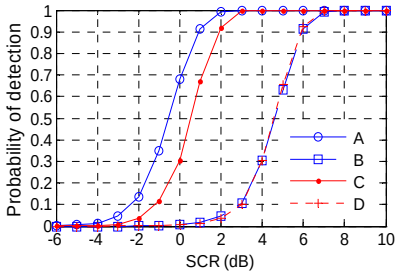

(a) Detection performances for target 1

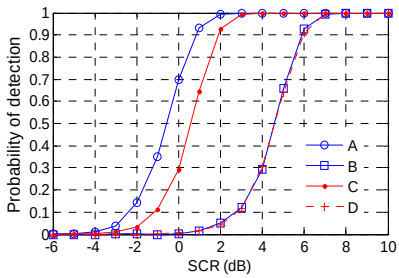

(b) Detection performances for target 2

Figure 7. Detection performance of two detectors for target 1 and target 2. ($p_{fa} = 0.0001, M = 32, N = 256$. A: The proposed detector, $M_0 = 4$; B: The integrator detector, $M_0 = 4$; C: The proposed detector, $M_0 = 8$; D: The integrator detector, $M_0 = 8$.)

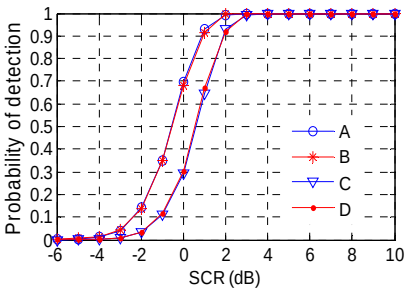

Figure 8. Detection performance of the proposed detector based on waveform entropy for the two targets. ($p_{fa} = 0.0001, M = 32, N = 256$. A: Target 1, $M_0 = 4$; B: Target 2, $M_0 = 4$; C: Target 1, $M_0 = 8$; D: Target 2, $M_0 = 8$.)

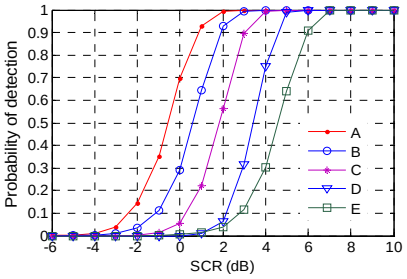

Figure 9. Detection performance for target 2 with different M_0. ($p_{fa} = 0.0001, M = 32, N = 256$. A: The proposed detector, $M_0 = 4$ B: The proposed detector, $M_0 = 8$; C: The proposed detector, $M_0 = 16$; D: The proposed detector, $M_0 = 32$; E: The integrator detector.)

The detection performance of the proposed detector for target 1 and target 2 with different Doppler distributions (M_0) is shown in Fig. 8. From Fig. 8, we can see that the detection performance of the proposed detection method is robust to the HRRP of the desired target, and yet is connected with the Doppler distribution of the target. Fig. 9 illustrates the relationship between the detection performance of the proposed detector and the Doppler distribution of the target echo. As can be seen, the detection performance of the proposed detector decreases while the Doppler of the target spreads. In this simulation, the detection performance of the proposed detector decreases 1 dB while M_0 doubles. In spite of this, the detection performance of the proposed detector is superior to the integrator detector even when $M_0 = M$.

VI. CONCLUSION AND FUTURE WORK

HRR radars are widely used in precision guidance in recent years, for the echoes of HRR radars involve abundant target information and can be used for target recognition and accurate tracking. This paper presents a novel range-spread target detection algorithm for missile-borne HRR radars. Firstly, the range-spread target echo model of missile-borne HRR chirp radar is established and the range alignment of HRRP is accomplished in the frequency domain. Then a CFAR range-spread detection algorithm based on the WE of the average combination of the HRRPs is addressed. The simulation indicates that the detection algorithm is superior to the traditional energy integrator and is robust for different

 ISBN: 978-1-61208-264-6

HRRPs of the target. The proposed detector based on WE needs not to estimate the parameters of the clutter, and the computational complexity of the detector makes it suitable for missile-borne radar signal processing. Future work will focus on the practical application of the proposed algorithm, and the target detection performance will be further tested by using the measured data.

REFERENCES

[1] Wehner, D.R., High-Resolution Radar, Boston: Artech House, 1995, Ch.p4-Ch.p5.

[2] B. Liu and W. Chang, "A novel range-spread target detection approach for frequency stepped chirp radar," Progress In Electromagnetics Research, vol. 131, 2012, pp. 275-292. doi:10.2528/PIER.12062510.

[3] L. Du, H. W. Liu, and Z. Bao, "Radar HRRP target recognition based on higher-order spectra," IEEE Trans. Signal Process., vol. 53(7), 2005, pp. 2359-2368

[4] Gerard A. Van. Der. Spek, "Detection of a distributed target," IEEE Transactions on Aerospace and Electronics Systems, vol. AES-7(5) , 1971, pp. 922-931.

[5] P. K. Hughes II., "A high-resolution radar detection strategy," IEEE Transactions on Aerospace and Electronics Systems, vol. AES-19(5), 1983, pp. 663-667.

[6] Karl Gerlach, Michael Steiner, and F. C. Lin, "Detection of a spatially distributed target in white noise," IEEE Signal Processing Letters, vol. 4(7), 1997, pp. 198-200.

[7] E. Conte, A. De. Maio, and G. Ricci, "GLRT-based detection algorithms for range-spread targets," IEEE Transactions on Signal Processing, vol.49(7), 2001, pp. 1336–1348.

[8] Karl Gerlach and M. J. Steiner, "Adaptive detection of range distributed targets," IEEE Transactions on Signal Processing, vol. 47(7), 1999, pp. 1844-1851.

[9] E. Conte and A. De. Maio, "Distributed targets detection in compound-Gaussian noise with Rao and Wald tests," IEEE Transactions on Aerospace and Electronic Systems, vol. 51, Apr, 2003, pp. 568-582.

ACKNOWLEDGMENT

The authors wish to thank the editors, reviewer 1, reviewer 2, reviewer 3, reviewer 4, and reviewer 5, whose comments and suggestions helped to improve the contents of the paper.

[10] Xiaofeng Song, "Effect of Doppler Frequency Shift on Linear Frequency Modulation Signal Pulse Compression," Electronic Science and Technology, vol. 22 (4), 2009, pp. 42-44.

[11] David K. Barton and Sergey A. Leonov, Radar Technology Encyclopedia (Electronic Edition), Boston: Artech House, 1998, pp. 217-222.

[12] Huixia Sun, Zheng Liu, and Yunhe Cao, "Estimation of a high-velocity target's motion parameters for a modulated frequency stepped radar," Journal of Xidian University, vol. 38(1), 2011, pp. 136–141.

[13] T.A. Moore et. al., "Use of the GPS Aided Inertial Navigation System in the Navy Standard Missile for the BMDO/Navy LEAP Technology Demonstration Program", Proceedings of ION GPS-95, Palm Springs, CA, September 12-15, 1995.

[14] George W. Stimson, "Introduction to Airborne Radar" (Second Edition), Raleigh: SciTech Publishing, Inc, 1998, Ch.p18-Ch.p19.

[15] S. Xu, P. Shui, and X. Yan, "CFAR detection of range-spread target in white Gaussian noise using waveform entropy," Electronics Letters, vol. 46(9), 2010, pp. 647-u69.

[16] L.M. Martyushev and V.D. Seleznev, "Maximum entropy production principle in physics, chemistry and biology," Physics Reports, 426, 2006, pp. 1-45.

 ISBN: 978-1-61208-264-6

A Brief Analysis of the Motion Compensation for FMCW SAR

Jia Gaowei
School of Electronic Science and Engineering
National University of Defense Technology
Changsha, China
jiagaoweinudt@gmail.com

Chang Wenge, Li Xiangyang and Zhao Zhiyong
School of Electronic Science and Engineering
National University of Defense Technology
Changsha, China
changwenge@nudt.edu.cn, lxyniu@sina.com,
zhaozhiyong.1983@gmail.com

***Abstract*—The combination of frequency modulated continuous wave (FMCW) and SAR (synthetic aperture radar) , is one of the most important and dynamic research around the world. For FMCW SAR, traditional approximation of stop-go is invalid, hence the traditional motion compensation method is no longer suitable for FMCW SAR. The signal model of FMCW SAR in the presence of motion error is derived in the paper, as well as the difference introduced by inter-pulse motion errors. Then a new motion compensation method is proposed. Simulated and experimental FMCW SAR data is generated and the well-focused image shows the proposed method is available.**

Keywords-Frequency Module Continuous Wave; Synthetic Aperture Radar; Motion Compensation; Line of Sight; intra-pulse; inter-pulse.

I. INTRODUCTION

Being a kind of advanced imaging sensor, SAR has been assembled with a variety of platforms, like airplane, airship, helicopter, missile, UAV (unmanned airplane vehicle), even the satellites. Most of these airborne platforms would be disturbed by the air current and are going to move on a non-ideal trajectory, accordingly, declines the quality of SAR imagery, even leads to a failure of imaging.

Airplane is a popular platform for SAR system, in the background of the glorious boom of UAVs, the combination of SAR and UAV, leads to a significant development for both the SAR sensor and UAVs. For one thing, it expands the application of SAR, for another, UAVs could have a stronger power of observation. However, the limited load of UAV could not satisfy the big, heavy and high-power pulsed SARs. Fortunately, the technology of FMCW could make the SAR smaller, low power and low-weight. It is the reason why FMCW SAR has been one of the most important and dynamic research in the field of radar around the world [1-5].

In FMCW SAR Systems，due to the fact that the transmitted wave is continuous and the length is in milliseconds, traditional approximation of stop-go in SAR theory is no longer valid. The motion during inter-pulse could not be ignored and the original method of motion compensation is not available either. But the error motion could still be separated into two terms: range error along the LOS and velocity error along track. Resampling the raw data along the track or transmitting the pseudo-continuous wave whose duty cycle is approximately to 1 then adjusting the PRF online are alternative for the elimination of velocity error. Thus the processing of eliminating velocity error could be seen as the preparation for imaging. However, it becomes complicated when dealing with the range error. A new method which is available for compensating the range error is proposed in this paper. In addition, a laboratorial FMCW SAR system is built-up, based on which the presented approach could be validated.

In Section II, the SAR system geometry and signal in presence of trajectory deviation is addressed. In Section III, difference phenomenon introduced by inter-pulse motion error is presented while the related approach is presented too. The proposed method is verified with the simulated and experimental data in Section IV. Finally, the conclusion is pointed out in Section V.

II. SIGNAL MODEL OF FMCW SAR IN NON-IDEAL CASE

Let us refer to Fig.1, in which the SAR system geometry in the presence of the 3-D motion error is presented. The real trajectory is shown as the dotted line, while the straight line along X denotes the ideal trajectory. O means the origin of the coordinates and β is the off-nadir angle. $P_e(X(t),Y(t),Z(t))$ are the azimuth, range and height position of the antenna phase center (APC), while $\Delta X(t),\Delta Y(t),\Delta Z(t)$ are the instantaneous 3-D error. $R(t,R_B)$ denotes the instantaneous range target-to-antenna distance and t is the time variable within time axis. It could be expressed as $t=\hat{t}+t_m$, in which $\hat{t}$ is the fast time and t_m is the slow time.

Assuming the static target T in the scene, whose position is $[X_n,Y_n,Z_n]$, then the instantaneous range between T and APC is

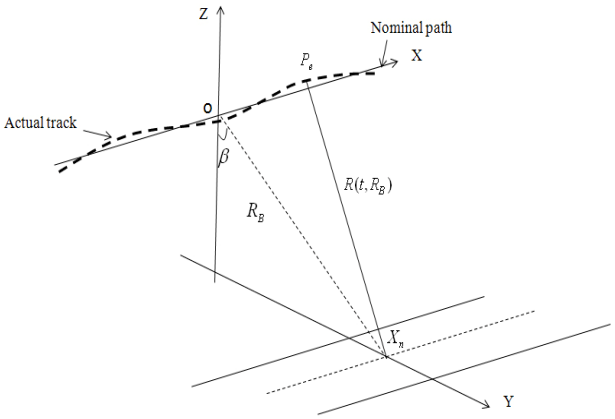

Figure.1. FMCW SAR system geometry in presence of trajectory deviation

 ISBN: 978-1-61208-264-6

$$R(t,R_B)=\sqrt{(X(t)-X_n)^2+(\Delta Y(t)-Y_n)^2+(\Delta Z(t)-Z_n)^2} \quad (1)$$

Correspondingly, $R(t,R_B)$ would be expressed in ideal case as

$$R(t,R_B)=\sqrt{(Vt-X_n)^2+Y_n^2+Z_n^2}=\sqrt{(Vt-X_n)^2+R_B^2} \quad (2)$$

where V means the ideal velocity, and $R_B=\sqrt{Y_n^2+Z_n^2}$ denotes the distance of closest approach. The expression shown in (2) reveals that the varied points at the same range have the same closest distance and they will have a similar signal form. It is known as invariance of azimuth and made the range cell migration compensation more convenient and quick. Unfortunately, the motion error destroys the invariance and convenience.

As $|\Delta Y(t)\sin\beta+\Delta Z(t)\cos\beta|<<\sqrt{(X(t)-X_n)^2+R_B^2}$, (1) could be expressed after the Taylor expansion as

$$\begin{aligned}R(t,R_B)&=\sqrt{(X(t)-X_n)^2+R_B^2-2\Delta Y(t)R_B\sin\beta-2\Delta Z(t)R_B\cos\beta+\Delta Y^2(t)+\Delta Z^2(t)}\\&\approx\sqrt{(X(t)-X_n)^2+R_B^2-2\Delta Y(t)R_B\sin\beta-2\Delta Z(t)R_B\cos\beta}\\&=\sqrt{(X(t)-X_n)^2+R_B^2}\cdot\sqrt{1-\frac{2R_B[\Delta Y(t)\sin\beta+\Delta Z(t)\cos\beta]}{(V_xt-X_n)^2+R_B^2}}\\&\approx\sqrt{(X(t)-X_n)^2+R_B^2}-\frac{R_B}{\sqrt{(V_xt-X_n)^2+R_B^2}}[\Delta Y(t)\sin\beta+\Delta Z(t)\cos\beta]\\&=\sqrt{(X(t)-X_n)^2+R_B^2}-\Delta r(t,R_B)\cos\theta\end{aligned} \quad (3)$$

where

$$\cos\theta=\frac{R_B}{\sqrt{(V_xt-X_n)^2+R_B^2}}\approx\frac{R_B}{\sqrt{(V_xt_m-X_n)^2+R_B^2}},$$ θ is the instantaneous squint angle between APC and scatter T. The first approximation in (3) is derived from the situation that $\max\{\Delta Y(t),\Delta Z(t)\}<<R_B$ and the second approximation benefit from the ignorance of the second and senior order term, most importantly, these approximations are available generally.

In (3) it is denoted that the 3-D motion error has been separated into cross-track and along-track motion error. (3) Could be expressed as follows in the case that ignoring the inter-pulse motion, exactly for the pulsed SAR,

$$R(t_m,R_B)=\sqrt{(X(t_m)-X_n)^2+R_B^2}-\Delta r(t_m,R_B)\cdot\cos\theta \quad (4)$$

in which t_m denotes the slow time, being a sample of the whole time t. $X(t_m)$ is the azimuth location of platform for pulsed SAR. $\Delta r(t_m,R_B)=\Delta Y(t_m)\sin\beta+\Delta Z(t_m)\cos\beta$. Intuitively, (4) could be obtained by exchanging t with t_m and the process is shown in Fig.2.

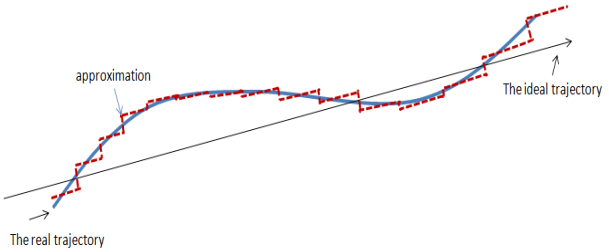

Figure.2. The real and sampled result of trajectory. The black thin straight line means the ideal trajectory and the thick line denotes the real trajectory while the dotted line is the sampled result, using PRI as the interval.

The sampled line is suitable for pulsed SAR but unavailable for FMCW SAR due to the fact that the inter-pulse motion error could not be ignored.

For FMCW SAR, assuming the period of the transmitted LFM is T_r, which is on the order of $10^{-4}s$. It is reasonable to consider the velocity contains same during T_r, shown as $V(t_m+\hat{t})=V(t_m),V_r(t_m+\hat{t})=V_r(t_m)\ \ \hat{t}\in[0,T_r]$, in which V_r means the velocity of platform along LOS. Consequently, (3) is separated as

$$\begin{aligned}R(t,R_B)&=\sqrt{(X(t)-X_n)^2+R_B^2}-\Delta r(t,R_B)\cos\theta\\&\approx\sqrt{(X(t)-X_n)^2+R_B^2}-\Delta r(t_m,R_B)\cos\theta\\&\quad-(V_y(t_m)\sin\beta\cdot\hat{t}+V_z(t_m)\cos\beta\cdot\hat{t})\cos\theta\\&\approx\sqrt{(X(t)-X_n)^2+R_B^2}-\Delta r(t_m,R_B)-\xi_{t_m}\cdot\hat{t}\end{aligned} \quad (5)$$

where $\xi_{t_m}=V_y(t_m)\sin\beta+V_z(t_m)\cos\beta$, the first approximation is available in the case of $\Delta Y(t)\approx\Delta Y(t_m)+V_y(t_m)\hat{t}$, $\Delta Z(t)\approx\Delta Z(t_m)+V_z(t_m)\hat{t}$ while the second one is $\cos\theta\approx1$, especially satisfied for high-band SAR.

The raw echo of FMCW SAR in the ideal case is [2-3]

$$\begin{aligned}s(\hat{t},t_m)&=w_r[\hat{t}-\frac{2R(t)}{c}]w_a[t_m]\exp(-j\frac{4\pi}{\lambda}R(t,R_B))\\&\quad\exp(-j\frac{4\pi k}{c}\hat{t}\cdot R(t,R_B))\exp(j\frac{4\pi kR^2(t,R_B)}{c^2})\end{aligned} \quad (6)$$

(6) is approximated usually as

$$\begin{aligned}s(\hat{t},t_m)&=\{w_r[\hat{t}]w_a[t_m]\exp(-j\frac{4\pi}{\lambda}R(t,R_B))\exp(-j\frac{4\pi k}{c}\hat{t}\cdot R(t,R_B))\\&\quad\}\otimes\exp(-j\pi k\hat{t}^2)\end{aligned} \quad (7)$$

where $w_r[\hat{t}],w_a[t_m]$ are the rectangle envelopes of echo in range and azimuth dimension respectively (ignoring the inference of antenna's weight). Substituting (5) into (6), the signal model of FMCW SAR which is in the presence of motion errors is derived. Since the range error has a negligible effects on the envelop, same to the inter-pulse motion error on RVP term, the finally echo is

$$
\begin{aligned}
s(\hat{t},t_m) = {} & w_r[\hat{t}-\frac{2R(t)}{c}]w_a[t_m]\exp(-j\frac{4\pi}{\lambda}R_1(t,R_B))\exp(j\frac{4\pi}{\lambda}\Delta r(t_m,R_B)) \\
& \exp(j\frac{4\pi}{\lambda}\xi_{t_m}\cdot\hat{t})\exp(-j\frac{4\pi k}{c}\hat{t}\cdot R_1(t,R_B))\exp(j\frac{4\pi k}{c}\hat{t}\cdot\Delta r(t_m,R_B)) \\
& \exp(j\frac{4\pi k}{c}\xi_{t_m}\cdot\hat{t}^2)\exp(j\frac{4\pi k R_1^2(t_m,R_B)}{c^2}) \\
& \exp(j\frac{8\pi k R_1(t_m,R_B)}{c^2}\cdot\Delta r(t_m,R_B))\exp(j\frac{4\pi k\Delta r^2(t_m,R_B)}{c^2})
\end{aligned} \tag{8}
$$

where $R_1(t,R_B)=\sqrt{(X(t)-X_n)^2+R_B^2}$, $R_1(t_m,R_B)=\sqrt{(X(t_m)-X_n)^2+R_B^2}$ and (8) is the basic of motion compensation for FMCW SAR.

III. THE DIFFERENCE INTRODUCED BY INTER-PULSE MOTION

Since the motion error along track could be eliminated respectively, this paper is concentrated on method of how to deal with the cross-track error. It is reasonable to believe that the along track error has been eliminated here. Ignoring tiny terms $\exp(j\frac{4\pi k}{c}\xi_{t_m}\cdot\hat{t}^2)$ and $\exp(j\frac{4\pi k\Delta r^2(t_m,R_B)}{c^2})$, (8) is simplified as

$$
\begin{aligned}
s_1(\hat{t},t_m) = {} & w_r[\hat{t}-\frac{2R(t)}{c}]w_a[t_m]\exp(-j\frac{4\pi}{\lambda}R_0(t,R_B))\exp(j\frac{4\pi}{\lambda}\Delta r(t_m,R_B)) \\
& \exp(j\frac{4\pi}{\lambda}\xi_{t_m}\cdot\hat{t})\exp(-j\frac{4\pi k}{c}\hat{t}\cdot R_0(t,R_B))\exp(j\frac{4\pi k}{c}\hat{t}\cdot\Delta r(t_m,R_B)) \\
& \exp(j\frac{4\pi k R_0^2(t_m,R_B)}{c^2})\exp(j\frac{8\pi k R_0(t_m,R_B)}{c^2}\cdot\Delta r(t_m,R_B))
\end{aligned} \tag{9}
$$

where $R_0(t,R_B)=\sqrt{(Vt-X_n)^2+R_B^2}$, $R_0(t_m,R_B)=\sqrt{(Vt_m-X_n)^2+R_B^2}$.

After a simplification and approximation, (9) changes to

$$
\begin{aligned}
s_1(\hat{t},t_m) \approx {} & \{w_r[\hat{t}]w_a[t_m]\exp(-j\frac{4\pi}{\lambda}R_1(t,R_B))\exp(-j\frac{4\pi k}{c}\hat{t}\cdot R_1(t,R_B)) \\
& \exp(j\frac{4\pi}{\lambda}\Delta r_R(t_m,R_B))\exp(j\frac{4\pi k}{c}\hat{t}\Delta r_R(t_m,R_B)) \\
& \exp(j\frac{4\pi}{\lambda}\xi_{t_m}\cdot\hat{t})\}\otimes\exp(-j\pi k\hat{t}^2)
\end{aligned} \tag{10}
$$

The convolution term outsides the bracket represents the RVP and envelop oblique terms, introduced by the de-chirp processing, which shall be eliminated in the process of imaging. Referring to (10), it is known that the errors due to range error along LOS is

$$
H_{los}=\exp(j\frac{4\pi}{\lambda}\Delta r_R(t_m,R_B))\exp(j\frac{4\pi k}{c}\hat{t}\Delta r_R(t_m,R_B))\exp(j\frac{4\pi}{\lambda}\xi_{t_m}\cdot\hat{t}) \tag{11}
$$

Specifically, the first two terms are introduced by intra-pulse motion and the last one is derived from the inter-pulse motion. The traditional approach could handle the former terms but be unavailable for the latter. The complete expression of $\exp(j\frac{4\pi}{\lambda}\xi_{t_m}\cdot\hat{t})$ is

$$
H_{\xi}=\exp(j\frac{4\pi}{\lambda}\xi_{t_m}\cdot\hat{t})=\exp\{j\frac{4\pi}{\lambda}[V_y(t_m)\sin\beta+V_z(t_m)\cos\beta]\cdot\hat{t}\} \tag{12}
$$

(12) is a function of $\hat{t}$ and be linear with it, whose influence is to introduce new range cell migration, expressed as

$$
\Delta Rcm=\frac{c}{2k}\cdot\frac{2}{\lambda}[V_y(t_m)\sin\beta+V_z(t_m)\cos\beta] \tag{13}
$$

where c represents the speed of light, k denotes the chirp rate. Since $V_y(t_m)$, $V_z(t_m)$ and β vary along azimuth and range respectively, so ΔRcm is changing in two-dimensional, increasing the difficulty to compensate quickly and completely. Fortunately, $V_y(t_m)$ and $V_z(t_m)$ are not very large, then a substituted method is compensating the whole scene with the range cell migration calculated in the center of scene, which is

$$
\Delta Rcm(t_m,R_c)=\frac{c}{2k}\cdot\frac{2}{\lambda}[V_y(t_m)\sin\beta_c+V_z(t_m)\cos\beta_c] \tag{14}
$$

where β_c denotes the off-nadir angle according to the center of scene.

As for the real-time processing of SAR, the approach of motion compensation and imaging are merged to pursuit the maximum efficiency. Due to the fact that range doppler (RD) algorithm is effectively and easy to realize, an available approach of motion compensation which is based on RDA is proposed in this paper, and the flow chart is shown in Fig. 3:

The flow chart of imaging process with motion compensation is similar with pulsed SAR exception for

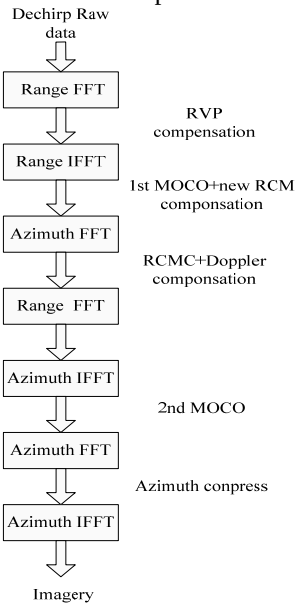

Figure.3. The flow chart of imaging process

TABLE.1: PARTIAL PARAMETERS OF SIMULATION

Range bandwidth	600MHz	altitude	700m
Maximum range	1120m	Minimum range	910m
Pulse duration	800us	velocity	30m/s

the terms of new RCM compensation, and the compensation of Doppler factor. The form of first and second ordered motion compensation could quote from [6][8], the two-step motion compensation method is used widely in data focusing. It's necessary to point out that the Doppler factor is derived from the continuous move inter-pulse and be considered as the main difference between pulsed SAR and FMCW SAR.

IV. THE RESULTS OF SIMULATION AND EXPERIMENT

It is common for airplane to be disturbed by the air current, especially, severe and high-frequency jitter would made the velocity error obvious and increase the difficulty for compensation. Firstly, partial parameters of simulation are settled in Table 1.

Assuming the location error in Y dimension obey a sine wave whose amplitude and period are 3m and 5s, while the location error in Z dimension obey a cosine wave whose amplitude and period are 4m/s and 5s. Then the velocity error could be calculated by the difference of location error. Both of them are shown in Fig. 4.

Based on (13) and the parameters in Table 1, we could calculate the new RCM introduced by inter-pulse motion errors, shown in Fig. 5.

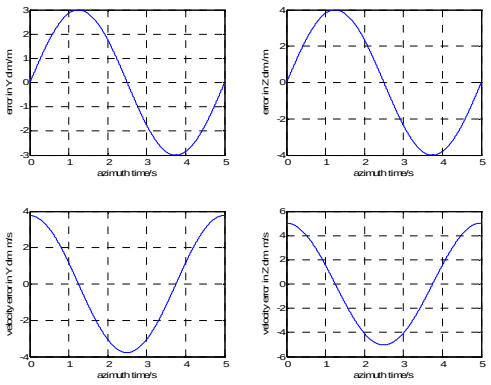

Figure.4 Location and velocity errors in Y and Z dimensions

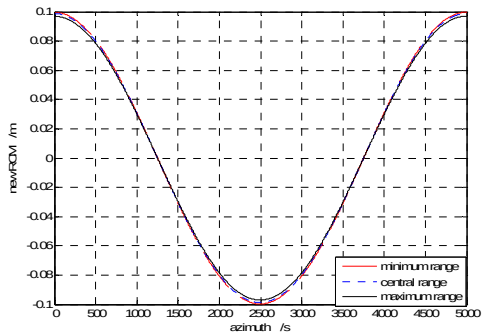

Figure.5. the new RCMs introduced by inter-pulse motion error

There are two conclusions can be derived from Fig. 5; for one thing, the absolute value of new RCM is about 0.2m which will has a obvious influence to imagery when the range resolution is less than 0.2m. For the other, referring to the parameter in Table.1, the difference of new RCM from minimum range or maximum range to central range are tiny, hence compensating the whole scene with (14) is available.

Fig.6 shows the result of an analysis of simulated FMCW SAR data. Fig.6 (a) shows the distribution of scatters. Fig.6 (b) shows the motion correction result using traditional compensation method, whereas Fig.6 (c) shows the motion correction result using the proposed compensation method. An array of point targets is used for the qualitative analysis, especially for the points located in the margin and center of scene. The proposed motion compensation is compared to traditional motion correction method in the presence of severe motion error. The better results performed by proposed method represent the better applicability for FMCW SAR.

From the theoretical analysis and simulated result, it has been seen that the proposed method is valid to compensate the motion errors when the resolution is very high and the motion error is severe. Although when the resolution is low and the trajectory is better, new range migration derived from (13) is less than half of range resolution, the new range migration derived from inter-pulse motion error could be ignored.

The experiment was also carried out with our designed FMCW SAR system, in which the SAR system is fixed on the roof of a sport utility vehicle (SUV), the LFM bandwidth is 600MHz, some corner reflectors were placed

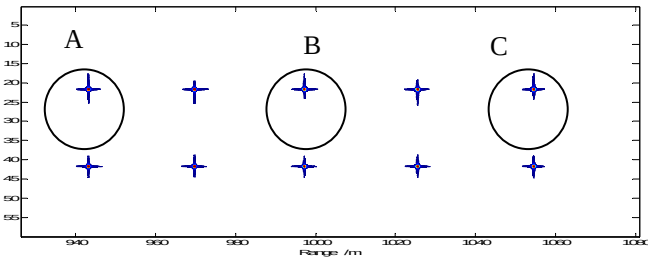

(a) The image of scatters

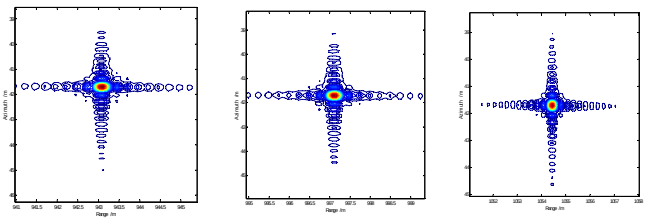

(b) From left to right are A, B, C point.

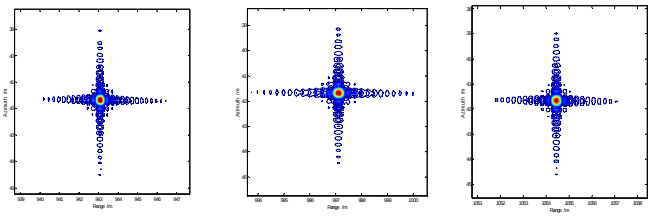

(c) From left to right are A, B, C point.

Figure.6. Simulated FMCW SAR data of an array of point targets and different results are compared with two methods.

 ISBN: 978-1-61208-264-6

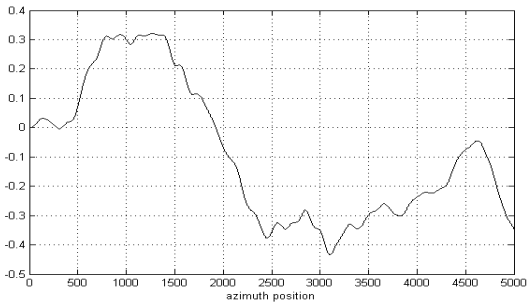

(a) Measured displacement from the ideal path along LOS (meters)

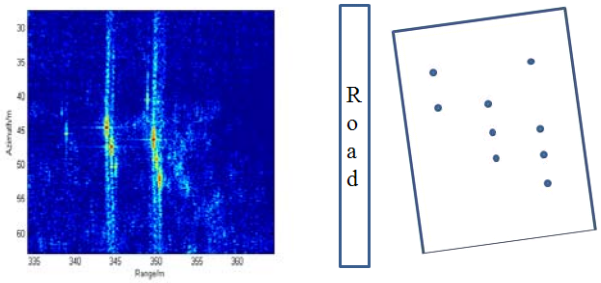

(b) SAR imaging result with motion corrected and schematic diagram of corner reflectors

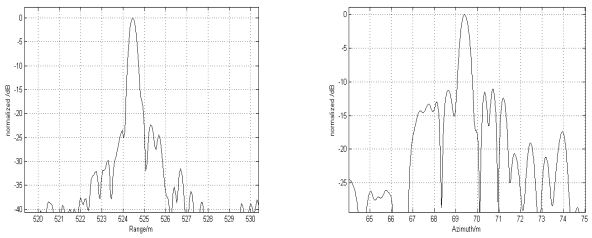

(c) The range and azimuth profile comparison

Figure.7. The processed SAR image with a 600-MHz bandwidth FMCW SAR on a SUV.

in the scene. With the imaging process chart shown in Fig.3, we obtained the results shown in Fig.7. From the above to down: (a) the measured motion error calculated from the GPS data. (b) the focused image after applying the proposed compensation scheme and the schematic diagram of corner reflectors.(c) the range and azimuth profile.

From Fig.7, it is obvious that the corner reflector is well focused. The amplitude is various because the off-nadir angle is approximate to zero so the variance of corner reflectors' placement has a significant influence on the radar cross section (RCS). In addition, the integrated side lobe rate of azimuth compression is higher than the ideal case, since the motion error contains high-frequency component which is hard to compensation based on GPS data. However, some autofocus approaches, such as PGA [9]-[10] and PACE [11] could improve the result of compression.

From the simulated and experimental result shown in Fig. 6, Fig. 7 and Fig. 8, it is obvious that the SAR is well focused, further, the proposed approach is valid. While more high-precise high-resolution large scene airborne based FMCW SAR data focusing is ongoing. It is confident that the high resolution SAR imagery will have a vast application in kinds of fields. Like remote sensing, monitor, cartography, disaster estimation, environment survey.etc.

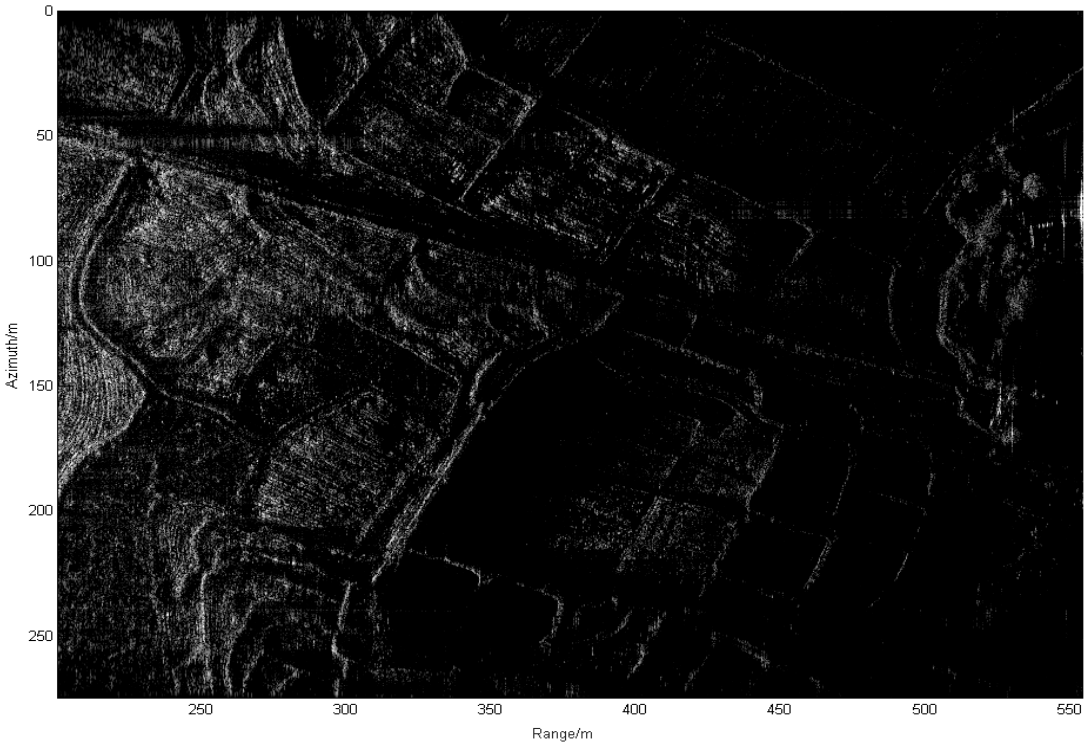

Figure.8. Focused FMCW SAR imagery processed with the proposed method. The scene is a paddy field, it is seen that the ridge and the alley of field are clear. In addition, the texture of reaped rice field is clear too.

V. CONCLUSION AND FUTURE WORK

The main difference between pulsed SAR and FMCW SAR is the approximation stop-go is invalid and the motion during inter-pulse should be considered. Hence the traditional motion compensation method which is suitable for pulsed SAR will no longer available for FMCW SAR. An available method for FMCW SAR motion compensation is proposed in this paper. The geometry and signal model of FMCW SAR in the presence of 3-D motion error is built; the influence introduced by inter-pulse motion error is analyzed while the accordingly approach is presented too. Simulated FMCW SAR data is generated and the proposed method is compared to traditional method. Simulation shows the proposed method results are much better than those of traditional method and the proposed method is particularly available for FMCM SAR. Eventually, the proposed approach is adopted on a laboratorial FMCW SAR system. Well-focused experimental data confirm the effectiveness of the presented method.

REFERENCES

[1] A. META. “Signal Processing of FMCW Synthetic Aperture Radar Data”. Delft University of Technology, Ph.D.thesis, 2005.

[2] A. META, P. Hoogeboom and L.P. Ligthart. “Signal Processing for FMCW SAR”. IEEE Trans on GRS.vol. 45.2007, pp. 3519 -3532.

[3] R. Wang, O. Loffeld, and H. Nies. “Focus FMCW SAR Data Using the Wave number Domain Algorithm ”. IEEE Trans on GRS. Vol. 48. 2010, pp. 2109 – 2118.

[4] J.J.M.deWit, A. Meta, and P.Hoogeboom. “Modified Range-Doppler Processing for FMCW Synthetic Aperture Radar ”. IEEE GRS Letters,vol. 3. 2006, pp.83-87.

[5] A.Ribalta. “Time-Domain Reconstruction Algorithms for FMCW-SAR ”. IEEE GRS Letters.vol. 8. 2011, pp.396-400.

[6] G.FORNARO. “Trajectory Deviations in Airborne SAR: Analysis and Compensation ”.IEEE Trans on AES.vol. 35.1999, pp. 997 - 1009.

[7] A. META, P.Hoogeboom, and L.P. Ligthart. “Non-linear Frequency Scaling Algorithm for FMCW SAR Data”. Proceedings of the 3rd European Radar Conference.2006, pp.9-12.

[8] E. C. Zaugg and D. G. Long. “Theory and Application of Motion Compensation for LFM-CW SAR”. IEEE Trans on GRS. vol. 46. 2008, pp.2990-2998.

[9] H.L.Chan and T.S.Yeo. “Noniterative Quality Phase Gradient Autofocus (QPGA) Algorithm for Spotlight SAR Imagery”. IEEE Trans on GRS. vol. 36. 1998, pp.1531-1539.

[10] W.L.Van Rossum and M .P.G. Otten. “Extended PGA for Range Migration Algorithms”. IEEE Trans on AES, Vol. 42. APRIL2006, pp.478-488.

[11] J.Kolman. “PACE: an autofocus algorithm for SAR”. Virginia, USA, 2005, pp.310-314.

 ISBN: 978-1-61208-264-6

A Novel DDS-PLL Hybrid Structure to Generate the LFM Signal

Zhao Zhiyong, Li Xiangyang, Chang Wenge, Jia Gaowei
School of Electronic Science and Engineering
National University of Defense Technique
Changsha, Hunan, China
E-mail: zhaozhiyong.1983@gmail.com, lxyniu@sina.com, changwenge@nudt.edu.cn, jiagaoweinudt@gmail.com

***Abstract*—The signal generator with Direct Digital Synthesizer Phase Locked Loop (DDS-PLL) Hybrid structure generates the signal with the qualities of the wide bandwidth and high frequency resolution. The long acquisition time in the PLL limits its applications. A novel generator structure is proposed by adding the sweeping voltage circuitry to the classical DDS-PLL Hybrid in order to accelerate the acquisition speed. A test circuitry is designed to testify the novel structure. The measured results indicate that the acquisition time is reduced to be 2.175μs and 1.032μs corresponding to 1MHz and 2MHz loop bandwidth respectively; the pulse compression result is very good where the main lobe width remains as ideal, Peak Side Lobe Ratio (PSLR) is better than -38dB, and the Integrated Side Lobe Ratio (ISLR) is better than -9.5dB.**

Keywords:* *DDS-PLL Hybrid; Frequency Sweeping; Fast-locking.

I. INTRODUCTION

With the developments of radar application, the requirements of fast frequency hopping increase. It has considerable benefits to improve the radar performances and reduce the difficulties in signal processing if the signal has large bandwidth, good frequency linearity and low harmonics [1].

Generally, a signal can be generated in three ways: Phase Locked Loop (PLL) [2], Direct Digital Frequency Synthesizer (DDFS) [3] and Direct Digital Waveform Synthesizer (DDWS) [4]. DDFS is named DDS for short usually. The PLL technique operates from audio frequencies up to millimeter waves and the bandwidth is large, it also has some drawbacks: poor linearity in the frequency modulation rate, long acquisition time, and large phase error. The DDS and DDWS both operate in digital way. Although they has the advantages of fine resolution, fast switching and continuous phase, the disadvantages of serious spur and harmonics and small bandwidth are obvious. For the most advanced commercial DDS circuit, the bandwidth is less than 1.4GHz, the phase noise is better than -128dBc/Hz, and the frequency resolution is 190pHz [5]. The system speed limitation causes the bandwidth of the signal generated by the DDWS to be relatively narrow, only 400MHz most [6].

In the DDS-PLL Hybrid structure, the DDS generates the narrow-band Intermediate Frequency (IF) signal with low intermediate frequency. The PLL up converts the IF to the required RF signal and expands the bandwidth. This structure has the benefits both from the DDS and PLL.

The acquisition time is the most serious problem in the DDS-PLL Hybrid structure. In the paper, we propose a novel structure by adding a sweeping voltage circuitry to the classical DDS-PLL Hybrid structure. It brings in the benefits of shortening the acquisition time. Meanwhile, the predistortion is employed to depress the static phase error and improve the pulse compression qualities.

The remaining sections of this paper are arranged as follows. Section II analyzes the acquisition process. The novel structure is introduced in section III. Section IV lists the measurements to the signals generated by the test system in the fields of acquisition time and pulse compression. This conclusion and future work are in Section V.

II. ACQUISITION ANALYSIS

The classical DDS-PLL Hybrid structure is depicted in Figure 1. In the structure, the BPF is band-pass filter, the PD is Phase Detector, and the LF is low-pass filter. The DDS generates the signal, used as the PLL reference, with the frequency f_c. The frequency of the system clock is f_r. The PLL outputs the signal with the frequency f_0. The inherent filter in the PLL depresses the harmonics in the DDS output. The PLL multiplies the reference frequency by N to get the signal with the high radio frequency and large bandwidth [7][8][9].

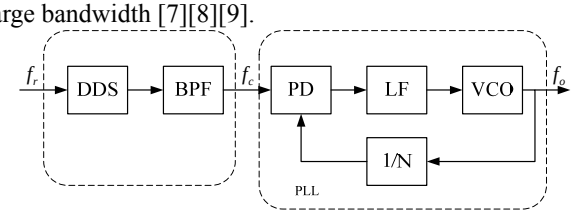

Figure 1. The Classical DDS-PLL Hybrid Structure

The process of bringing a loop into lock is called acquisition. In Charge-Pump Phase-Locked Loops (CPPLL), the process of acquisition is divided to two parts, frequency pull-in process and phase acquisition process. Pull-in tends to be slow and often unreliable. When the signal was applied, a beat note at frequency $\Delta\omega$ appears. The frequency pull-in process initiates and the beat note decreases. After the frequency pull-in process, the beat note reaches the pull-in limitation, and phase acquisition process starts. The time from unlocked state to locked state is named acquisition time. It is also divided into be frequency pull-in time and phase acquisition time. In theory, they are defined as follows for a 2nd order type 2 PLL, respectively [10].

$$T_f = \frac{\omega_r}{2\pi\omega_n^2} + \frac{2\xi}{\omega_n} \quad (1)$$

 ISBN: 978-1-61208-264-6

$$T_\theta = \frac{5}{\xi \omega_n} \quad (2)$$

Where ω_r is the phase detecting frequency, ω_n is the nature frequency, and ξ is the loop damping ratio. For example, when the phase detecting frequency is 20MHz, the loop damping ratio is 0.707, and the natural frequency is 500 kHz, then the frequency pull-in time and phase acquisition time are 2.48μs and 2.25μs respectively. In general, the phase acquisition process is faster than the frequency pull-in process.

III. FAST ACQUISITION

There are some drawbacks in the classical hybrid structure namely large phase error in the steady state and long acquisition time. We propose a novel structure by adding sweeping voltage controlling circuitry to the classical structure. The novel structure is shown in Figure 2.

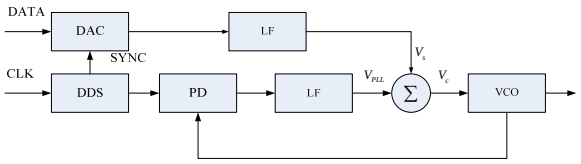

Figure 2. The block diagram of the novel topology

The CLK is the system clock. The VCO controlling voltage V_c is a sum of the sweeping voltage V_s from Digital-to-Analog Converter (DAC) and the fine-tuned voltage V_{PLL} from the PLL. The sum is realized by a voltage summer.

$$\begin{aligned} f_o(t) &= K_{VCO} \cdot V_c(t) \\ &= K_{VCO} \cdot (V_s(t) + V_{PLL}(t)) \\ &= K_{VCO} \cdot V_s(t) + K_{VCO} \cdot V_{PLL}(t) \\ &= K_{VCO} \cdot k \cdot t + K_{VCO} \cdot V_{PLL}(t) \end{aligned} \quad (3)$$

From (3), we know that the sweeping voltage is a linear function of time. A short pull-in time can be achieved since the output frequency is directly set by the controlling voltage V_c, therefore, the beat note between the divided output and reference input is smaller than the pull-in limitation $\Delta\omega_p$. The sweeping voltage takes the role of frequency setting. The phase acquisition is accomplished by the PLL. The ideal sweeping voltage curve is shown in Figure 3(a) where the sweeping voltage increases from 1.6V to 9.1V in 100μs as a straight line, and decreases to 1.6V abruptly at the end of the signal pulse. The fine-tuned voltage output by PFD is shown in Figure 3 (b) where the fine-tuned voltage varies fast in a small range of -0.1V~0.1V. Obviously, two oscillations occur in Figure 3 (b). The first one is the tracking process of the Linearity Frequency Modulation (LFM) signal from 0μs to 100μs. The second one is the process of tracking the falling frequency corresponding to the voltage falling at 100μs in Figure 3 (a). Although the instantaneous frequency migration is very large, thanks to the sweeping voltage which sets the output frequency of VCO primarily, the fine-tuned voltage converges to zero smoothly.

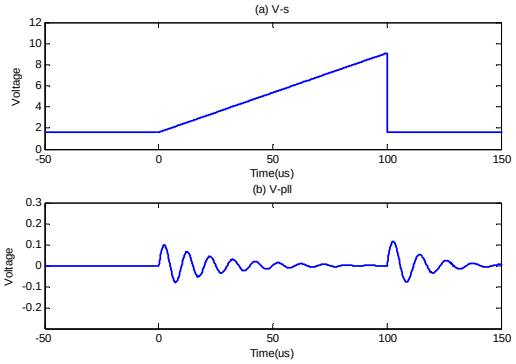

Figure 3. Simulated transient settling behavior

However, the actual voltage–frequency characteristic is nonlinear in practice. For instance, the VCO characteristic curve of ROS-2800-719+ is shown in Figure 4.

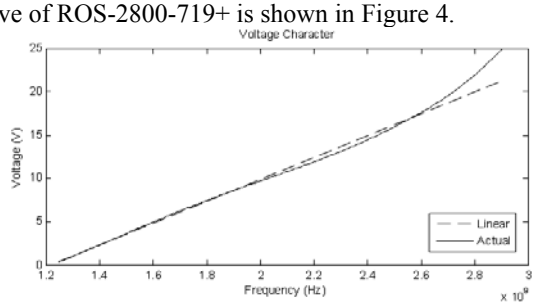

Figure 4. Characteristic of VCO

The dashed curve shows the ideal characteristic. The solid line figures out the actual VCO voltage–frequency characteristic. It approximates to a straight line in the range of 1V to 25V. The nonlinearity is serious when the voltage beyond 25V. We must note that the range with good linearity should be used when generating signals with the device ROS-2800-719+.

To sweep with the actual voltage characteristic we need to sample the actual controlling voltage and store them in the memory. The actual sweeping voltage is generated by DAC with the sample data. Synchronization of the sweeping voltage and the reference is most important. For this reason, the controlling signal SYNC is introduced as shown in Figure 2.

In the novel structure, the sweeping voltage takes the original beat note between the down-scaled frequency and the reference frequency into the pull-in limitation $\Delta\omega_p$. The frequency pull-in time is reduced to be sufficient small that we can neglect it as compared to the phase acquisition time. So there is phase acquisition time only. The acquisition speed is increased substantially.

The loop filter and summer are shown in Figure 5. The in-phase follower and RC devices in the dash frame compose the active loop filter. The PLL is 3rd order type 2. Different from the ideal 2nd order type 2 PLL, there is an

 ISBN: 978-1-61208-264-6

adding high frequency pole. The influence to the transient induced by the additional pole is small. The PLL approximates an ideal 2nd order type 2. The current I_p output by the PFD is imported into inverter phase adder across the in-phase follower with the sweeping voltage across the RC filter. The summer outputs the final control voltage V_c.

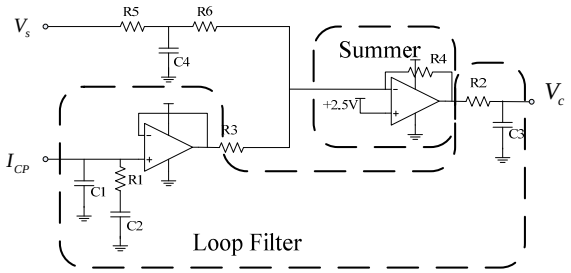

Figure 5. The loop filter and summer

The values of the components in the loop filter are listed in Table . The software ADIsimPLL provided by ADI can be used to calculate the acquisition time based on listed values.

IV. MEASUREMENT

We test the novel structure with four modules on hand. They are the DDS module, the DAC module, the filter and summer module, the PFD and VCO module. The connections and the actual circuit are shown in Figure 6.

- The DDS module: The DDS we used is AD9910 with 1GSPS internal clock speed and up to 400 MHz analog outputs. There is an integrated RAM which can be used as the storage of the phase predistortion data;
- The DAC module: The DAC5675 gets 14-bits data widths, up to 400MSPS updating speed. When the SYNC comes, voltage sample data is read out from the storage, and delivered to DAC to generate the sweeping voltage;
- The filter and summer module: This module contains an active filter and an inverse summer. The circuit is as in Figure 6. The amplifiers in the filter and summer are OP1177 and AD823 respectively;
- The PFD and VCO module: The PFD is ADF4113 with the features of 0.2GHz ~4.0GHz RF input frequency, 200MHz phase detect frequency, and max 5mA current output. VCO is ROS-2800-719+ with 1.4GHz~2.8GHz output.

By changing the RC values in the loop filter, we build PLLs with 1MHz and 2MHz loop bandwidth respectively. The signal is generated with 600MHz bandwidth, 100μs pulse width, and 6MHz/μs FM rate. And the output signal is in the range of 1350MHz~1950MHz, the frequency resolution is 5.82Hz. We record the waveform by the oscillograph of DPO71254 with 6.25GHz sample rate.

The measurement of the acquisition time is difficult because the lock-in point is not easy to be determined. In this paper, we fix the lock-in point with the phase error. If the phase error falls into the range of ±10°, starts to oscillate in a small range, and diminishes, we define the loop is locked in. Based on this assumption, the phase errors of the loop with 1MHz and 2MHz bandwidth are drawn in Figure 7 and Figure 8. The red one is the phase error of the waveform, and the black one is the high-order polynomial curve. We zoom in on the starting part in Figure 7 (a) and Figure 8 (a) and show in Figure 7 (b) and Figure 8 (b).

Table I. VALUE OF COMPONENTS IN THE LOOP FILTER

Loop bandwidth	R1(Ω)	R2(Ω)	R3(Ω)	R4(Ω)	R5(Ω)	R6(Ω)	C1(F)	C2(F)	C3(F)	C4(F)
2MHz	164	1k	500	1k	500	500	50.4p	1.36n	28.4p	28.4p
1MHz	81.9	1k	500	1k	500	500	2.2p	5.45n	56.8p	56.8p
500kHz	40.9	1k	500	1k	500	500	8.7n	21.8n	114p	114p

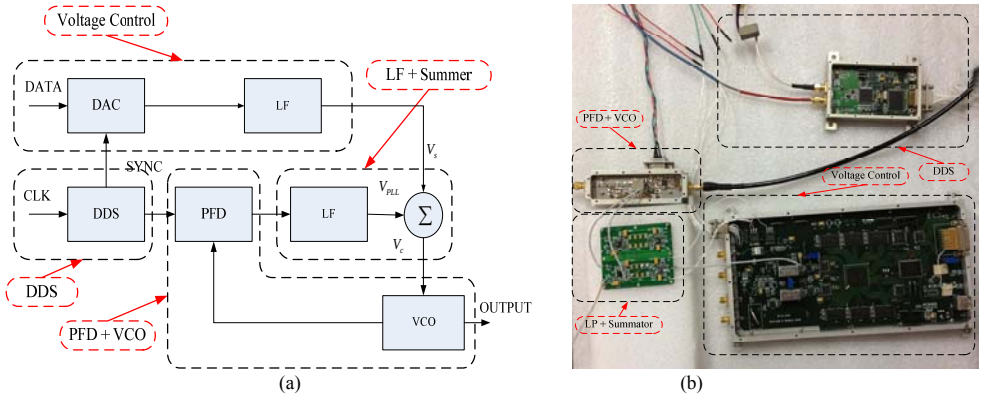

(a) (b)

Figure 6. The test circuitry

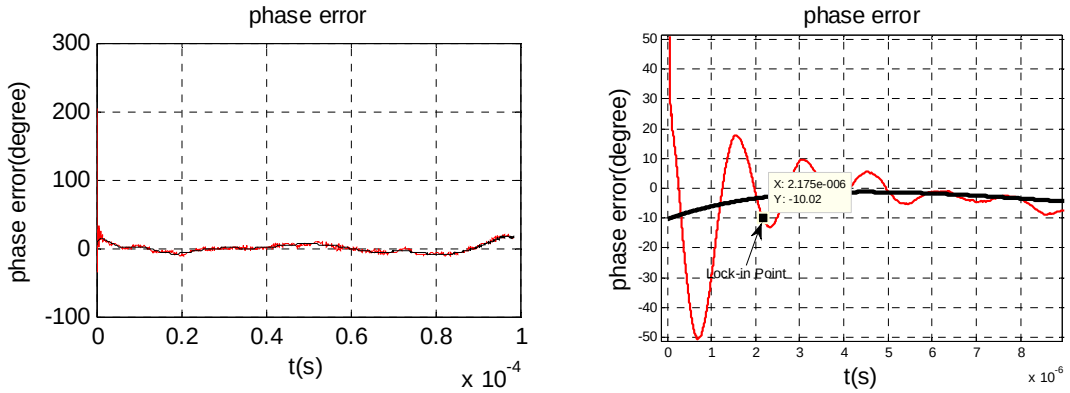

(a) (b)

Figure 7. Locking-in time in 1MHz loop

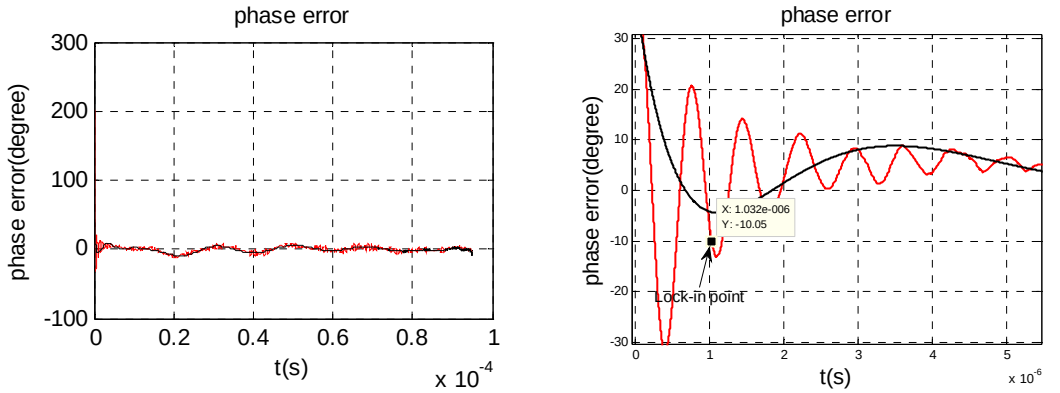

(a) (b)

Figure 8. Locking-in time in 2MHz loop

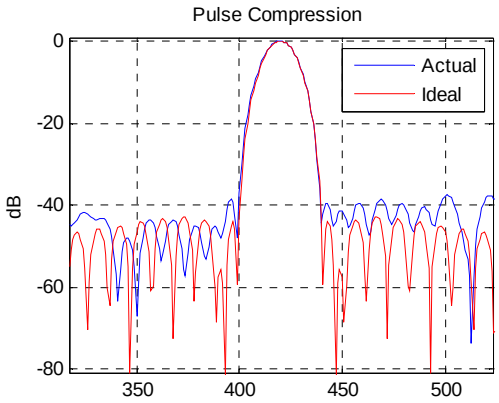

Figure 9. Compression result

In the figures, the phase error is very large at the beginning, and then diminishes quickly. We find the lock-in point and mark it in Figure 7 (b) and Figure 8 (b). The acquisition times can be read out from the figures: 2.175μs and 1.032μs for the two loops of different bandwidth respectively. We calculate the acquisition time for the classical structure using ADIsimPLL. The phase acquisition time and frequency pull-in time are 3.43μs and 2.32μs for the loop of 1MHz bandwidth. And they are 2.175μs and 1.032μs for the loop of 2MHz bandwidth. Obviously, the total acquisition time is decreased to approach phase acquisition time. The novel structure proposed in this paper is effective to reduce the frequency pull-in time.

The pulse compression with Hamming weight is shown in Figure 9. The red curve is the pulse compression with ideal signal; the blue curve is the pulse compression with the actual signal. It has perfect

 ISBN: 978-1-61208-264-6

performance. The main-lobe width of the actual signal is the same as the ideal one, the PLSR is better than -38dB, and the ISLR is -9.5dB towards -9.9dB for the ideal.

V. Conclusion and Future Work

A structure of fast locking signal generator is proposed in this paper, with adding sweeping voltage circuitry to the classic DDS-PLL Hybrid. Great decrease of the frequency pull-in time is achieved because the PLL is brought in the pull-in range by the sweeping voltage. To validate the structure, a test system is built to generate a LFM signal with 600MHz bandwidth, 100μs pulse width and 6MHz/μs FM rate. The acquisition time is reduced to be 2.175μs and 1.032μs with 1MHz and 2MHz loop bandwidth respectively. Based on this novel structure, signals with wider bandwidth and longer duration are expected to be generated to improve the qualities of radar.

References

[1] Woo J-C., Lim B-G., and Kim Y-S., “Modulation of the Recursive Side lobe Minimization Technique for the Range-Doppler Algorithm of SAR Imaging”, Journal of Electromagnetic Wave and Applications, Vol.25, No.13, pp:1783-1794, 2011.

[2] Pichler Markus, Stelzer Andreas, Gulden Peter, Seisenberger Claus, and Vossiek Martin, “Phase-error measurement and compensation in PLL frequency synthesizers for FMCW sensors - II: Theory”, IEEE Transactions on Circuits and Systems I-Regular Papers, Vol. 54, No. 6, pp. 1224-1235, Jun 2007.

[3] Kroupa VF, Cizek V, Stursa J, and Svandova H, “Spurious signals in direct digital frequency synthesizers due to the phase truncation” IEEE Transactions on Ultrasonics Ferroelectrics and Frequency Control, Vol. 47, No. 5, pp: 1166-1172, Sep 2000.

[4] Zhao Zhiyong, Chang Wenge, and Li Xiangyang, Yan, Feifei, “Design and realization of wideband radar signal simulator”, 6th International Conference on Radar, RADAR 2011, RADAR 2011, pp. 1280-1283, Chengdu, China, October 24, 2011 - October 27, 2011.

[5] “3.5 GSPS Direct Digital Synthesizer with 12-Bit DAC AD9914”, Rev. A, Analog Devices, Inc. 2012.

[6] Zhao Zhiyong, Chang Wenge, and Li Xiangyang, Tu, Ruibin, “Pre-distortion for DDWS system”, 13th International Radar Symposium, IRS-2012, pp. 345-349, Warsaw, Poland, May 23, 2012 - May 25, 2012.

[7] Wu Yi-Da, Lai Chang-Ming, Lee Chao-Cheng, and Huang Po-Chiun, “A Quantization Error Minimization Method Using DDS-DAC for Wideband Fractional-N Frequency Synthesizer”, IEEE Journal of Solid-State Circuits, Vol. 45, No. 11, pp. 2283-2291, Nov 2010.

[8] Chiu Wei-Hao, Huang Yu-Hsiang, and Li Tsung-Hsien, “A Dynamic Phase Error Compensation Technique for Fast-Locking Phase-Locked Loops”, IEEE Journal of Solid-State Circuits, Vol. 45, No. 6, pp. 1137-1149, Jun 2010.

[9] Nicholas H.T. III, Samueli H., and Kim B., “The optimization of direct digital frequency synthesizer performance in the presence of finite word length effects”, Frequency Control Symposium, 1988, Proceedings of the 42nd Annual, pp.357-363, 1-3 Jun 1988.

[10] Gardner F. M. and Front Matter, “Phaselock Techniques”, Third Edition, John Wiley & Sons, Inc., Hoboken, NJ, USA.

 ISBN: 978-1-61208-264-6

Research of Current Movements of the Earth's crust in the Territory of Almaty City

Zhumabek Zhantayev, Baurzhan Kurmanov, Assylkhan Bibossinov, Kairat Sadykov
Department of geophysical and geodynamic monitoring
LLP "Institute of Ionosphere"
Almaty, Kazakhstan
Emails: {Nckit@spaceres.kz, baur.kurman@gmail.com, bibossinov@yahoo.com, sadykovka@gmail.com}

***Abstract*—During the work carried out, measurements were taken by a local GPS network. It was the primary pre-processing and interpretation of the data network for the city of Almaty. The investigation had been carried to find the velocity field of modern movements of the Earth's surface according to the GNSS-service. All the GPS-data were processed by the software package GAMIT/GLOBK.**

Keywords-GNSS-network; IGS; SELE station; GNSS-measurements; velocity field; data interpretation.

I. INTRODUCTION

Deformation of the Earth's surface on the territories of large cities occurs very often. The main reason is the growing demand of high-rise buildings, the intensive development of underground space, hydro-mode system violations and finally vibration impacts. In some areas of Almaty, the level of impact on the geological structures is already approaching a critical point. This means that the number of destructions will increase dramatically due to any deformations of the Earth's surface.

Organization of a geodesic effective monitoring system of major cities is possible with high precision satellite methods. This allows almost continuous monitoring in a variety of geographical conditions to observe a certain strain down to millimeter level accuracy [1-4]. These studies were conducted for the first time in the territory of Almaty city.

II. GOALS AND OBJECTIVES

The goal of this work is to study the velocity of modern movements of the Earth's surface by GNSS-measurements data for the region of Almaty.

On the basis of the known geological conditions, taking into account the differences, a priori data was compiled which preliminary was used for observing the network for the Almaty region. Research showed that it is the stochastic network with distribution points which is the most appropriate solution for this region. We have relied on the size of the foundation block structures that may have a major impact on the surface deformation processes in case of their mutual relative movements during strong earthquakes.

There are several kilometers between large faults when we consider the Earth's crust depth is about 3 km.

The network is split over the Almaty region with insignificant deviations beyond its limits (Figure 1) and consists of 14 observation points (Table I). The expected results are maps of modern movements in the territory of Almaty city.

TABLE I. THE LOCAL GPS NETWORK

№	Points name	Id	Coordinates		
			X	***Y***	***H***
1	Base	Baza	$43^0$10'37.1850	$76^0$57'4.0122	1209
2	Astrophysics	Act2	$43^0$10'35.7349	$76^0$57'58.5639	1316
3	Koktobe	Kokt	$43^0$13'40.7683	$76^0$59'06.7640	925
4	Airport	Aers	$43^0$19'38.9931	$77^0$0'46.2605	639
5	Sairan	Sair	$43^0$14'17.5640	$76^0$51'54.7307	757
6	Kiziltu-4	Kzt4	$43^0$22'13.5082	$77^0$5'5.0653	634
7	Kapchagai highway	Kpch	$43^0$22'30.8869	$76^0$57'20.5690	614
8	Baiserke	Bser	$43^0$27'8.1595	$77^0$2'46.2691	573
9	Boraldai	Borl	$43^0$18'56.6571	$76^0$48'56.5204	727
10	Pervomaysky pond	Trpp	$43^0$23'46.1461	$76^0$54'32.1729	620
11	Hippodrome	Ipdr	$43^0$18'27.0849	$76^0$55'42.3869	668
12	12th city hospital	Gorb	$43^0$13'54.3048	$76^0$54'36.2963	791
13	Kazakhfilm	Kazf	$43^0$14'50.4854	$76^0$54'15.9350	927
14	Central Park	Cprk	$43^0$15'47.3451	$76^0$58'12.4722	743

III. METHOD

Not being able to organize a network of GPS-synchronized observations in the city, there were a restricted series of successive observations using one receiving station. Measurements are held periodically by each of the points using a Leica GRX 1200 GG Pro receiver, twice a year. The duration of recording satellite signals at one point is 48 hours in a continuous mode with intervals of 30 seconds which was adopted by regulations. Per one session, each point worked about 48 hours and produced 5720 independent acts of registration. This gives an opportunity for further processing

 ISBN: 978-1-61208-264-6

to increase the ratio of signal/random noise in the square root of this number (about 76 times).

GPS - measurements was conducted since 2010 to the present time. GAMIT / GLOBK software package is used for pre-processing GPS data [7].

During calculations of a priori coordinates and velocities of points, a priori data of the Earth's rotation and orbital data generate a single integrated set that must be internally consistent. Imposition of severe restrictions on any of these parameters for a regional solution can deform the system. In order to prevent such action restriction, a priori coordinate, the speed, the parameters of orbit satellite and the Earth's rotation in the solution should not be rigid. However, that decision could shift or collapse the entire system of points and/or their velocactionity vectors. Stabilization allowing to define reference system by minimizing the deviation of the resulting solution which was obtained as the result of a decision using the a priori coordinates and velocities for a set of well-defined stations. The iterative scheme of stabilization automatically excludes measurements points, for which coordinates have large deviations. The velocity fields of the region are shown in Figs. 2 and 3. The rest of the time points are not very accurately measured [4-6].

The permanent station SELE, part of the global network IGS, has an error about 0.1 mm / year. The rest of the time points are not very accurate measurements. This shows that is necessary to conduct special works to reduce the errors in the city network stations to the order of 1-2 mm/year.

IV. CONCLUSIONS

For the study of modern movements of the Earth's crust of Almaty, was built a local network and data collection from 2011 to 2012.

The first study which was conducted in the city of Almaty showed that within urbanized areas such work is possible and necessary. The main advantage of working with such a system is the possibility of rate parameters simultaneously in three mutually orthogonal components, characterized by significant variations during the year.

The errors of international IGS stations in the pre-processing were about- 0.5-2 mm/year, and the local points showing the error of 5-20 mm/year.

Errors are likely due to the small number of independent observations in temporary settlements, due to the inability to organize continuous monitoring because of the absence in receiver numbers and transportation problems.

During two years of follow up in urban areas, set features significant movement of surface points about 3- 25 mm/year. The conclusion shows that it is necessary to observe simultaneous points, then moving receivers to other items with overlapping observation systems.

To ensure the high quality of the primary data monitoring it is necessary to choose points of global network stations (IGS) with following control of the data quality.

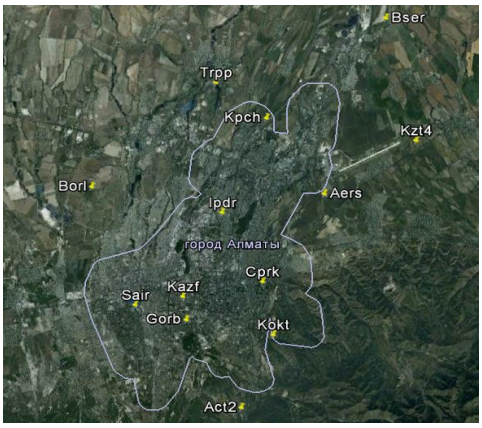

Figure 1. Local area network in the territory of Almaty city.

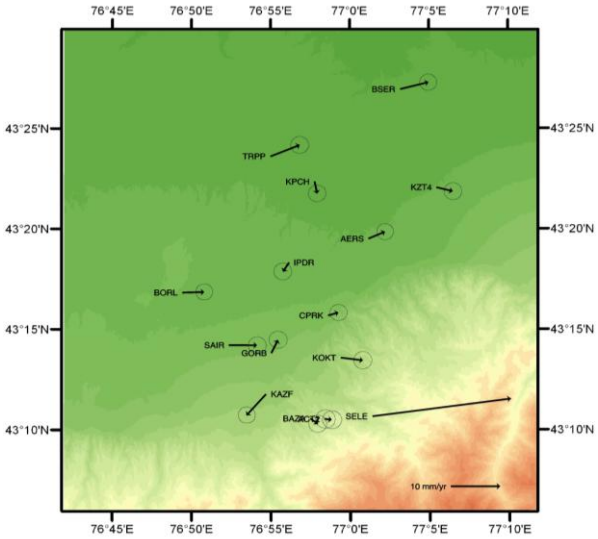

Figure 2. Velocity field relative to the Eurasian continent.

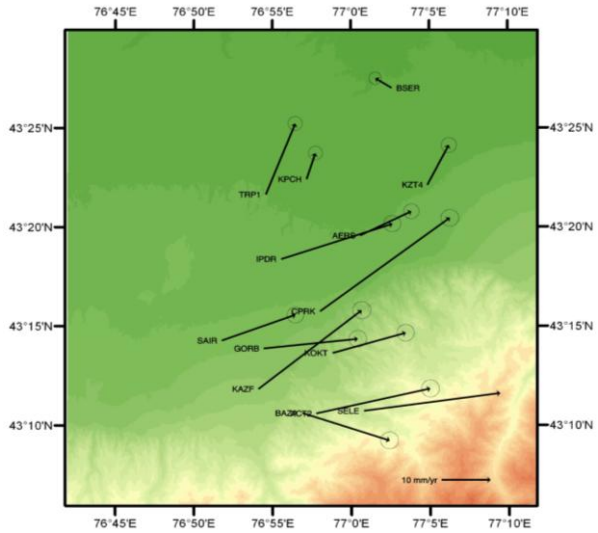

Figure 3. Velocity field relative to the center of the Earth.

 ISBN: 978-1-61208-264-6

REFERENCES

[1] Zubovich A.V., X.-q. Wang, Y.G. Scherba, G.G. Schelochkov, R. Reilinger, C. Reigber, O.I. Mosienko, P. Molnar, W. Michajljow, V.I. Makarov, J. Li, S.I. Kuzikov, T.A. Herring, M.W. Hamburger, B.H. Hager, Y.-m. Dang, V.D. Bragin and R.T. Beisenbaev; GPS velocity field for the Tien Shan and surrounding regions. Tectonics, 2010, Vol. 29, TC6014, doi:10.1029/2010TC002772.

[2] Zhantayev ZH.SH., Namvar R.A-A., Aketaev Zh.E. Shcherba Y.G.; The effectiveness of modern satellite GPS-monitoring technologies geodynamic state of the lithosphere in Kazakhstan. Almaty: Nauka, 2009. pp. 2-3. [Rus].

[3] Gabrielov A.I., Keylich-Borok V.I., Levshina T.A., Shaposhnikov V.A.; The block model of the lithosphere dynamics. Mathematical methods in seismology and geodynamics. Pergamon Press, 1986, pp. 168-178. [Rus]

[4] Garagash I.A., Patalaha E.I.; When the fracture collapse (shear flow) and folding / / Geotectonics, № 6, 1990, pp. 23-31. [Rus]

[5] Steinberg V.V., et al. Assessment methods of seismic effects. / / Problems of Engineering Seismology, Vol. 34, 1993, pp. 5-94. [Rus]

[6] Shebalin N.V. The estimation of seismic intensity. Seismic scale and methods of measurement of seismic intensity. Moscow: Nauka, 1975. pp. 87 - 109. [Rus]

[7] Http://www-gpsg.mit.edu/~simon/gtgk/ [retrieved: July 2009]

 ISBN: 978-1-61208-264-6

Cloud top Height Estimation from the Meteosat Water Vapor Imagery Using Computational Intelligence Techniques: Preliminary Results

Stavros Kolios, Petros Karvelis, Chrysostomos Stylios
Department of Informatics and Telecommunication Technology
Technological Educational Institute of Epirus
Arta, Greece
e-mail: stavroskolios@yahoo.gr, stylios@teleinfom.teiep.gr, pkarvelis@gmail.com

Periklis Tagkas
Department of Applied Foreign Languages in Management and Commerce
Technological Educational Institute of Epirus
Igoumenitsa, Greece
e-mail: ptangas@teiep.gr

***Abstract*—This study investigates the cloud top height estimation using nonlinear methods to Meteosat imagery. The suggested approach aims to develop an integrated statistical methodology to estimate the cloud top height on a pixel basis using Meteosat Second Generation water vapor imagery. Radiosonde measurements are used as reference dataset and a spatio-temporal correlation with Meteosat images is performed in order to collect a representative sample for the statistical analysis. Here, we apply Multi Layer Perceptron (MLP) and Support Vector Machines (SVM) and we compare the results to the Linear Regression model. The best results are achieved using SVM for regression. The proposed approach is very promising as it can be used for future in-depth analysis so as to develop a robust approach for geometrical height estimation on a pixel basis of the operational data of Meteosat imagery. It is noted that an accurate estimation of cloud top height can help to eliminate geometric restrictions (e.g. Parallax phenomenon) of the Meteosat satellite imagery, improving its usefulness in a wide area of applications and especially in satellite-based weather forecast.**

Keywords-Regression; SVM; MLP; Meteosat; Radiosondes; Geometric height

I. INTRODUCTION

Geostationary satellites nowadays provide many different data about the parameters concerning land, ocean and atmosphere and they are used in numerous applications not only in detecting but also in monitoring (on a real-time basis) and short-range forecasting [1], [2].

There are some limitations because of the geostationary satellite instrument field of view and their scanning mode that usually lead to inaccuracies about the exact location of some cloud features (especially convective cloud systems) on the Earth's surface. These cloud systems are usually vertically extended at several kilometers in the atmosphere, with the cloud tops reaching the middle and upper troposphere [3-5]. The above-mentioned inaccuracies are caused by the parallax phenomenon, [6] which is more evident in the convective nature cloud systems that are depicted at satellite images and appears at mid-latitudes growing towards the poles and the edges of the field of view of the satellite instruments.

The convective cloud systems have great importance because they are related to extreme weather phenomena and events like lightning, hail, strong winds and floods [5], [7] and [8].

As a result, the accurate estimation of Cloud Top Height (CTH) is appropriate in order to calculate and eliminate the parallax effect and it can provide the real location of the convective systems above the Earth's surface, more accurately.

There are several studies that propose different approaches and methodologies to estimate the geometric CTH but they are mainly lacking in high accuracy or usually refer to small geographic areas [9-12].

Our effort is to propose a robust, generalized and accurate methodology to estimate the geometrical height of different cloud features (especially convective ones) at a broad range of latitudes and longitudes. This methodology aims to improve on pixel basis the accuracy of clouds' location above the Earth's surface, so as to eliminate the parallax phenomenon in real-time monitoring applications based on Meteosat operational data.

Section II provides all the relative information about the data used and the area of interest. In Section III, the methodology was followed in order to estimate cloud top height, is provided. The Section IV presents the accuracy results of the proposed methodology and the Section V provides the conclusions of the the study.

II. DATA AND AREA OF INTEREST

Two different datasets were used in this study. Firstly, radiosonde observations (provided by the National Oceanic and Atmospheric Administration/Earth System Research Laboratory: NOAA/ESRL) of the greater area of the Mediterranean region (Fig. 1). Radiosonde data are suitable to measure vertical profiles of many important parameters like temperature, pressure and geometrical height. Secondly, Meteosat satellite images of two different channels (5 and 6) at spectral ranges of 5.35 - 7.15 μm (spectral center: 6.2 μm) and 6.85 - 7.85 μm (spectral center: 7.3 μm) respectively

 ISBN: 978-1-61208-264-6

(provided via the European Organization for the Exploitation of Meteorological Satellites: EUMETSAT). It is mentioned that the specific Meteosat channels have been chosen because they belong to the water vapor absorption spectral region and are used to detect water vapor levels especially in the middle and upper troposphere. All the data used were collected for a period between 5/6/2012 and 14/6/2012. The area of interest covers the greater area of the Mediterranean basin (Fig. 1) because in this region the convective systems are developing frequently and especially during the warm period of the year [13] and [14] causing floods, strong winds and hail among others that affect importantly humans and properties. These cloud systems are vertical extended in several kilometers.

The accurate detection of their spatial extent on the Earth's surface of the field of view of a geostationary satellite like Meteosat, needs an accurate estimation of the CTH in order to eliminate the parallax phenomenon that is evident in such convective cloud systems [6], [12].

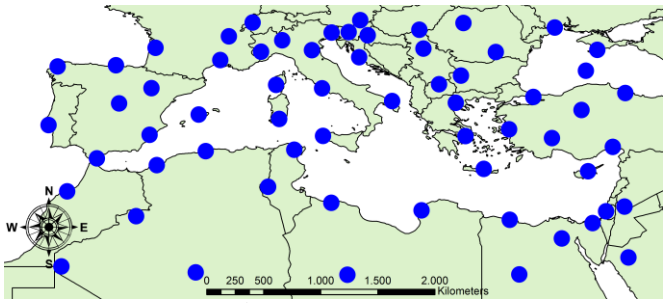

Figure. 1. Locations of radiosonde stations that are used in this study.

III. METHODOLOGY

A representative training sample was needed in order to determine the non-linear functions that combine the Meteosat pixel values with the cloud geometrical height that is recorded by the radiosonde measurements (Fig. 2). For this reason, a spatiotemporal correlation between radiosonde measurements and satellite images was implemented.

More specifically, the radiosonde balloons are usually released twice a day at times 00:00 UTC and 12:00 UTC. For the selected time period, a database was gathered with all the satellite images that have 90-min time distance from the point where radiosonde balloons were released. The 90-min time gap was chosen because our intention is to estimate optically thick and vertically extended cloud systems that are related to severe weather. These are generally called convective cloud systems where the cloud tops existed usually in the middle or the upper troposphere. The balloons reach these atmospheric levels at about 90 minutes after their release according to [15]. So, for each satellite image obtained 90 minutes after the radiosonde balloon release, a 5 x 5 kernel window (~25 x 25 km according to the Meteosat image pixel size at mid-latitudes) was created and implemented around the coordinates of every available Radiosonde point (Fig. 3). The mean Brightness Temperatures (BT) value of the two used channels and their mean value of BT differences of the kernel window pixels, are finally associated with the radiosonde measurement that was considered just above the cloud top (Fig. 2). In order to determine, if the radiosonde passed through a cloud and which is the height of its cloud top, we used the criterion of Relative Humidity level as it was proposed in [16]. If the value of the RH was higher than 85% (maximum value is the saturation level: 100%) then we consider that the balloon was in a cloud. More analytically, the higher (in km) measurement of a radiosonde balloon recordings that has RH lower than 85% and at least the three previous and consecutive measurements with RH higher than 85%, was considered as cloud top measurement (Fig. 2).

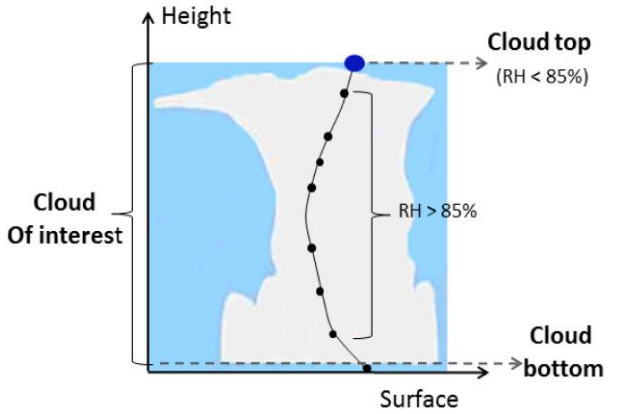

Figure 2. Schematic representation of a representative cloud system and its cloud top height, as it is calculated with the proposed methodology.

It is mentioned that the size of the kernel window was chosen because the radiosonde balloons during their ascent can reach more than 20 km horizontal distance from their initial location as it was mentioned in [15].

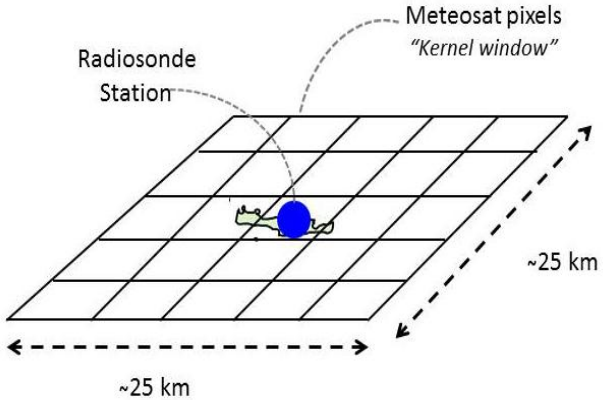

Figure 3. The kernel window of Metosat pixels that was implemented around the location of a radiosonde station.

The spatio-temporal correlation considering all the above-mentioned criteria was implemented in an automated

way using an algorithm developed for this purpose in the VB.NET programming language.

Using the above mentioned spatio-temporal correlation methodology for the radiosonde and Meteosat data, a final dataset of 181 cases in the area of interest for the selected time period, was collected. Each case is a given radiosonde dataset that satisfies the RH criteria. For each case, the geometric height above the ground was recorded (as it was measured from the radiosonde) along with the mean BT in the channels 5 and 6 of the kernel window Meteosat pixels and their mean BT difference. These samples (of 181 cases) comprised our final data set for the regression analysis.

More specifically, we defined our dataset as $\{x_i^1, x_i^2, x_i^3, y_i\}, i = 1,\ldots,n$ where n is the number of measured samples (181 cases), the x_i^1 is the mean BT value of Meteosat kernel window pixels in the channel 5, x_i^2 is the mean BT value of Meteosat kernel window pixels in the channel 6, x_i^3 is the BT difference between them and y_i is the measured height of the balloon for each one of the collected cases.

This is a classical regression problem where the variable that we have to predict is y_i. Here, we examine a Linear Regression model and two non-linear methods: Multi-Layer Perceptron (MLP) Neural Network and Support Vector Machines (SVM) , in order to predict this value.

A. Linear Regression

A linear regression model assumes that the relationship between the dependent variable y_i and the p-vector of observed x_i is linear. Thus, the model has the general form:

$$\mathbf{Y} = \boldsymbol{\beta}\mathbf{X} + \boldsymbol{\varepsilon}\,, \tag{1}$$

where

$\boldsymbol{\beta} = \begin{pmatrix} \beta_1 & \beta_2 & \cdots & \beta_p \end{pmatrix}^T$: are the regression coefficients,

$\mathbf{X} = \begin{pmatrix} x_1^1 & x_1^2 & \cdots & x_1^p \\ x_2^1 & x_2^1 & \cdots & x_1^p \\ \vdots & \vdots & \ddots & \vdots \\ x_n^1 & x_n^2 & \cdots & x_n^p \end{pmatrix}$: is the observation matrix and

$\boldsymbol{\varepsilon} = \begin{pmatrix} \varepsilon_1 & \varepsilon_2 & \cdots & \varepsilon_p \end{pmatrix}^T$:are the error terms.

The parameters $\boldsymbol{\beta}$ are estimated using the Least Squares method and a standard solution is obtained [4].

B. MLP

Neural networks are used as a direct substitute for multivariable regression and other statistical analysis techniques. A neural network is used to represent a nonlinear mapping between input and output vectors [2, 18].

Multi-Layer Perceptron (MLP) neural network is the most widely used neural network architecture for classification and/or regression problems. MLP networks consist of an input layer, one or more hidden layers and an output layer (Fig. 4 represents an MLP architecture with one hidden layer). Each layer has a number of units and each unit is fully interconnected with weighted connections to units in the subsequent layer.

The output of MLP is defined as a linear combination of the outputs of the hidden layer nodes where every neuron uses a weighted average of the inputs through a function (e.g. sigmoid function).

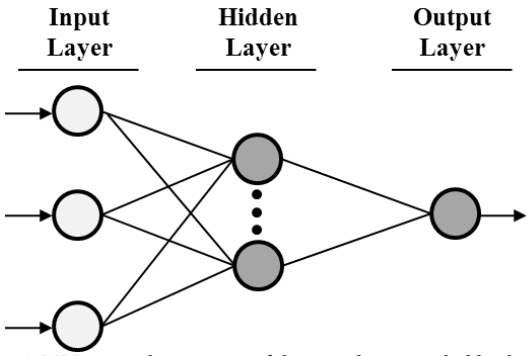

Figure 4. MLP network consisting of the input layer, one hidden layer and the output layer.

The MLP transforms p inputs to l outputs through some nonlinear functions. The output of the network is determined by the activation of the units in the output layer as follows:

$$g_0 = f(\sum_h g_h w_{h0})\,, \tag{2}$$

where $f()$ is the activation function, g_h is the activation of h -th hidden layer node and w_{h0} is the weight of the connection between the h -th hidden layer node and 0-th output layer node. The most used activation function is the sigmoid and it is given as follows:

$$g_0 = \frac{1}{1+e^{-\sum_h g_h w_{h0}}}\,. \tag{3}$$

The activation level of the nodes in the hidden layer is determined in a similar fashion. The error function is defined as the difference between the calculated value and the target value, as follows:

$$E = \frac{1}{2}\sum_i^n \sum_0^l (y_0^{(i)} - g_0^{(i)})\,, \tag{4}$$

where n is the number of pattern in data set and l is the number of output nodes.

The aim is to reduce the error by adjusting the interconnections between layers. The weights are adjusted using the Back Propagation (BP) algorithm. The algorithm

 ISBN: 978-1-61208-264-6

requires a training data that consists of a set of corresponding input and target pattern values y_i . During the training process, MLP starts with a random set of initial weights and then training continues until the set of w_{ih} and w_{h0} are optimized so that a predefined error threshold is met between g_0 and y_0 [3].

C. SVM for regression

Support Vector Machines are applied not only to classification problems but also to regression ones. SVM contain all the main features that characterize maximum margin algorithms: a nonlinear function is learned by linear learning machine mapping into high dimensional kernel induced feature space.

In SVM regression, the input x is firstly mapped onto a m-dimensional feature space using nonlinear mapping, and then a linear model is constructed in this feature space. The linear model is given by:

$$f(x,w)=\sum_{j=1}^{m} w_j g_j(x)+b\,, \qquad (5)$$

where $g_j(x),\ j=1,\ldots,m$ denotes a set of nonlinear transformations and b is the bias term.

SVM regression uses a new type of loss function called ε-insensitive loss function based on [5,6]:

$$L_\varepsilon(y, f(x,w))=\begin{cases} 0, & \text{if } |y-f(x,w)|\le\varepsilon \\ |y-f(x,w)|-\varepsilon, & \text{otherwise} \end{cases}. \qquad (6)$$

SVM regression performs linear regression in the high-dimension feature space using ε-insensitive loss and tries to reduce model complexity by minimizing $\|w\|^2$. This can be described by introducing slack variables $\xi_i^*, \xi_i, i=1,\ldots,n$, to measure the deviation of training samples outside ε - zone.

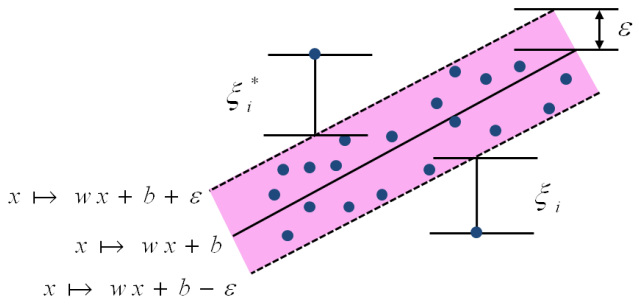

Figure 5. Epsilon zone with slack variables and selected data points.

Thus SVM regression is formulated as minimization of the following functional [6]:

$$\text{minimize} \quad \frac{1}{2}\|w\|^2 + C\sum_{i=1}^{n}(\xi_i+\xi_i^*)$$

$$s.t. \quad \begin{cases} y_i - f(x_i,w) \le \varepsilon+\xi_i^*\,, \\ f(x_i,w)-y_i \le \varepsilon+\xi_i^* \\ \xi_i^*, \xi_\iota \ge 0, \iota=1,\ldots,n \end{cases} \qquad (7)$$

IV. RESULTS

We have tested and evaluated the above-mentioned regression models using a dataset of $n=181$ samples. 80% of the dataset was randomly selected and used as the train set and the rest (20%) of the dataset was used as test set.

TABLE I. THE AVAILABLE DATASET DIVIDED INTO TRAIN AND TEST SET.

	Number of Instances (%)	**Number of Instances (#)**
Train Set	80	145
Test Set	20	36
Data Set	**100**	**181**

A. MLP architecture

In order to determine the best architecture for the MLP Neural Network, we tested different formulations consisting of one or two hidden layers, with 3 up to 20 neurons in each one. Table II, presents the best architectures for one and two hidden layers respectively in terms of R-coefficient and Mean Absolute Error.

TABLE II. BEST MLP ARCHITECTURES FOR ONE AND TWO HIDDEN LAYERS.

Layers	**Architecture (Input-Hidden-output) nodes**	**Correlation coefficient**	**Mean Absolute Error (MAE)**
One Hidden Layer	3-18-1	0.7272	1541.05
Two Hidden Layers	3-18-2-1	0.7372	1399.21

B. SVM parameter selection

In order to suggest the most appropriate values for the parameters C , ε of SVM, we applied a GridSearch method [7]. Table III, presents the results in terms of the correlation coefficient and MAE for the determined parameters that reported with the maximum correlation coefficient.

TABLE III. SVM PERFORMANCE FOR THE PARAMETERS $C=25$, $\varepsilon=0.1$.

Layers	**Correlation coefficient**	**Mean Absolute Error (MAE)**
SVM	0.7238	1286.97

 ISBN: 978-1-61208-264-6

C. Comparison of the Regression models

Table IV presents a comparison of the results of the three models used in our experiments including the Linear Regression method.

TABLE IV. COMPARISON OF THE THREE MODELS.

Layers	Correlation coefficient	Mean Absolute Error (MAE)
Linear Regression	0.7200	1401.93
MLP	**0.7372**	1399.21
SVM	0.7238	**1286.97**

Fig. 6 illustrates the SVM predicted values and the actual values for the test set.

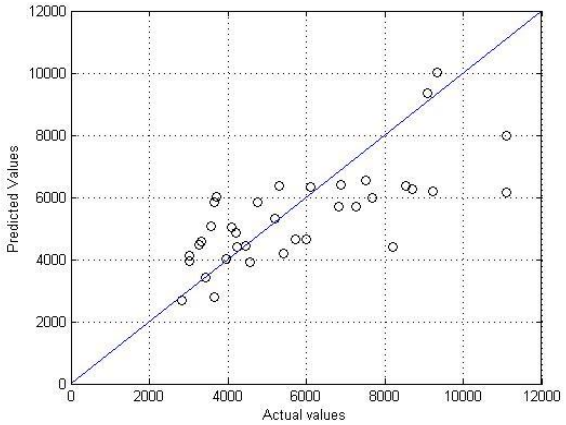

Figure 6. The SVM predictions and the actual values.

Fig. 7 displays the error of the predicted height versus the actual height in meters for the test set. As one can observe as the altitude rises from 8000 to 11000 km, the error becomes significantly large.

This is mainly due to the lack of a sufficient number of cloud tops (as they are defined with the RH criterion) in heights between 8000 and 1200 km in the selected time period. This fact led to a small number of collected cases and consequently to significant errors of the regression procedures at these heights. Increasing the time period of study, the number of the convective cases in the study area and consequently the number of convective cloud tops above 8000m will be increased. This goes beyond the scope of this study and it will be our first priority in the our future work.

In this study, all three recorded features were used in order to estimate the height; it would be interesting to study the effect of each one. For this reason we conducted the same experiments with all the combinations of the features and we present the results in terms of the correlation coefficient and MAE in Table V.

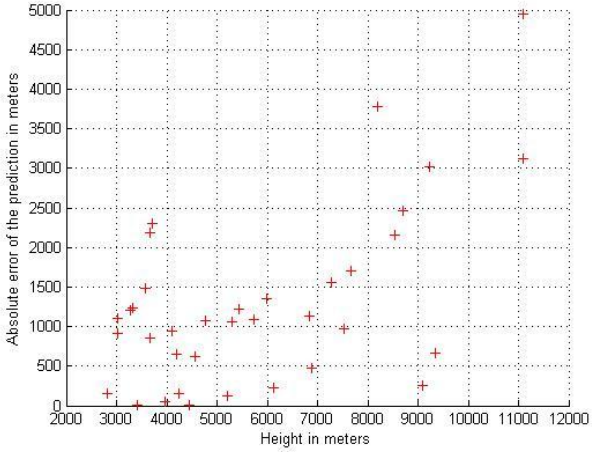

Figure 7. Absolute error of the prediction versus height (in meters).

It is concluded that the most powerful feature is the mean BT value of Meteosat kernel window pixels in channel 5, then is the BT difference between channels 5 and 6 and last is the mean BT value of Meteosat kernel window pixels in channel 6.

TABLE V. SVM REGRESSION USING EACH FEATURE.

	$BT_{channel\ 5}$	$BT_{channel\ 6}$	$BT_{channel\ 5} - BT_{channel\ 6}$
Corr. Coef.	**0.6979**	0.3348	0.4017
MAE	**1524.3**	1975.2	1813.6

V. CONCLUSIONS AND FUTURE WORK

In this study, some preliminary results regarding the cloud height estimation from Meteosat water vapor imagery were presented. An analytical and automated spatio-temporal methodology is suggested to investigate the correlation of radiosonde measurements and Meteosat Brightness Temperature values. For the estimation of geometrical cloud top height, three methodologies were examined: a linear one and two nonlinear algorithms, MLP and SVM.

Our purpose is to gradually develop a robust and accurate algorithm for CTH estimation for different cloud features (and especially the convective ones) as they are depicted in Meteosat infrared imagery. Our final intention is to cover the operational needs of CTH estimation in large geographic areas, with a simple, accurate and easy to use dataset. Using accurate estimations of the CTH, we intend in the near future to estimate (and reduce) the parallax phenomenon which is evident in the geostationary orbit satellite imagery, mainly used in the satellite-based weather forecasting.

The first results showed that mean errors vary in general between 1000 m and 1500 m and there are significant errors especially after the height of 8000 m in the atmosphere. These errors could be explained due to the lack of data for height above 8000 m in the selected time period. These findings require further investigation which is beyond the scope of this study. Nevertheless, the correlation coefficients

 ISBN: 978-1-61208-264-6

were considered quite satisfactory and promising for all the used algorithms and their parameterizations.

Future work will concern a categorization of the different types of clouds in order to study separately every discrete category of the cloud features that are depicted in the Meteosat satellite imagery. The handling of high cloud tops that penetrate the lower stratosphere is an additional topic that we are planning to study, too.

What is of great importance also, is the collection of a larger dataset that will allow more robust results and the use of additional channels of Meteosat imagery in the infrared region in order to evaluate their performance in the geometric height estimations.

In addition to this, other approaches such as Random Forests [18], could be used to try to test and improve the accuracy of the cloud height estimations.

ACKOWLEDGMENT

This work is partially supported by the project "Adriatic Port Community System APC" (code 111) funded by IPA Adriatic Cross-border Cooperation Programme 2007-2013 co-financed by European Union, Instrument for Pre-Accession Assistance.

REFERENCES

[1] A. D. Vila, A. L. Machado, H. Laurent, and I. Velasco, "Forecast and Tracking the Evolution of cloud clusters (FORTRACC) using satellite infrared imagery: methodology and verification," Weather Forecast. 2008, vol. 23, pp. 233-245.

[2] S. Kolios and H. Feidas, "An automated nowcasting system of Mesoscale Convective Systems for the Mediterranean basin using Meteosat imagery. Part I: System description," Meteorological Applications, 2012, DOI: 10.1002/met.1282.

[3] S. P. Ray, "Mesoscale Meteorology and Forecasting," American Meteorology Society, Boston, 1986.

[4] A. Roger and Sr. Pielke, "Mesoscale Meteorological Modeling," International geophysics series, Academic Press, Second Edition, 2002.

[5] A. R. Houze S. A. Rutledge, M .I. Biggerstaff, and B. F. Smull, "Interpretation of Doppler weather-radar displays in mid-latitude mesoscale convective systems," Bulletin of American Meteorological Society, 1989, vol. 70, pp. 608-719.

[6] G. A. Vicente, J. C. Davenport, and R. A. Scofield, "The role of orographic and parallax corrections on real time high resolution satellite rainfall rate distribution" International Journal of Remote Sensing, 2002, vol. 23, pp. 221-230.

[7] J. F. Correoso, E. Hernandez, R. Garcia-Herrera, E. Barriopedro, and D. Paredes, "A 3-year study of cloud-to-ground lightning flash characteristics of MCS over Western Mediterranean Sea," Atmospheric Research, 2006, vol., pp. 79 89-107.

[8] A. L. Machado, W. Lima, O. Pinto and A. Morales Relationship between cloud-to-ground discharge and penetrative clouds: A multi-channel satellite application," 2008, Atmospheric Research, In press.

[9] G. G. Campell and K. Holmlund, "Geometric cloud heights from Meteosat," International Journal of Remote Sensing, 2004, vol. 25, pp. 4505-4519.

[10] C. M. Naud, B.A. Baum, M. Pavolonis, A. Heidinger, R. Frey, and H. Zhang, "Comparison of MISR and MODIS cloud-top heights in the presence of cloud overlap," Remote Sensing of Environment, 2007, vol. 107, pp. 200-210.

[11] R. Borde and P. Dubuisson, "Cloud top height estimation using simulated METEOSAT-8 radiances", Proc. SPIE 6745, Remote Sensing of Clouds and the Atmosphere XII, 67450J (October 03,2007), doi:10.1117/12.737801.

[12] P. Pešice and Z. Sokol, "Meteosat parallax correction using radar echotops," ERAD 2008 – The fifth European Conference on radar in Meteorology and Hydrology. ISBN 978-951-697-676-4, CD.

[13] C. Morel and S. Senesi, "A climatology of mesoscale convective systems over Europe using satellite infrared imagery. I: Methodology," Quarterly J. of Royal Meteorological Society, 2002, vol. 128, pp. 1953-1971.

[14] S. Kolios and H. Feidas, "A warm season climatology of mesoscale convective systems in the Mediterranean basin using satellite data," Theoretical and Applied Climatology, 2010, vol. 102, pp. 29-42.

[15] D. J. Seidel, B. Sun, M. Pettey, and A. Reale, "Global radiosonde balloon drift statistics," J. of Geophysical Research, 2011, doi:10.1029/2010JD014891.

[16] J. Wang and W. B. Rossow, "Determination of cloud vertical structure from upper-air observations," Journal of Applied Meteorology. 1995, vol. 34, pp. 2243-2257.

[17] P. K. Simpson, "Artificial neural system-foundation, paradigm, application and implementation," New York: Pergamon Press, 1995.

[18] C. Bishop, "Neural Networks for Pattern Recognition," Oxford, University Press, 1995.

[19] S. Weisberg, "Applied Linear Regression," Willey, 2005.

[20] V. Vapnik, "The Nature of Statistical Learning Theory," Springer, New York, 1995.

[21] A. Smola and B. Schölkopf, "A tutorial on support vector regression", Journal Statistics and Computing, 2004, vol. 14(3), pp. 199-222.

[22] C-W. Hsu, C-C. Chang, and C-J. Lin, "A practical guide to support vector classification," Technical report, Department of Computer Science, National Taiwan University. July, 2003.

[23] L. Breiman, "Random Forests, Machine Learning," 2001, vol. 45(1), pp. 5-32.

 ISBN: 978-1-61208-264-6

The Two-Loop Tracking Strategy for Real-Time Multi-Antenna GNSS Receivers

Pedro A. Roncagliolo, Jorge Cogo, and Javier G. García
Laboratorio de Electrónica Industrial, Control e Instrumentación (LEICI),
Dto. Electrotecnia, Facultad Ingeniería, UNLP, La Plata, Argentina.
Emails: {agustinr, jorge.cogo, jgarcia}@ing.unlp.edu.ar

***Abstract*—A multi-antenna global navigation satellite system receiver accepts many radio-frequency inputs simultaneously. Then, many antennas can be deployed on a vehicle and the receiver can decide which one is useful for the reception of each satellite´s signal. As a consequence, navigation solutions can be obtained in more adverse conditions, but at the cost of an important increase of the receiver complexity. Particularly, tracking of the satellite signals is a challenging task in these receivers, especially when a variation in the vehicle´s attitude impose a change in the antenna used for a satellite signal reception. Carrier tracking is critical during these changes of antenna since the distance between them is larger than the signal wavelength. Thus, a direct antenna commutation can produce important tracking transients that degrade the navigation measurements, affect data demodulation, and can produce a loss of signal tracking. The strategy presented in this work allows the receiver to keep tracking during these antenna commutations avoiding the detrimental tracking transients. Since it is based on close-loop schemes, it is suitable for real-time receivers due to their low computational complexity. The proposed technique is tested in a simulated low-earth orbit satellite scenario assuming a constant change of attitude due to a roll movement along the orbit direction vector. It is shown that a four-antenna receiver using the proposed tracking strategy can properly track the satellites in view, in spite of the frequent antenna commutations imposed by the vehicle´s rotation.**

***Index Terms*—GPS; GLONASS; Antenna Radiation Pattern; Carrier Tracking Loops; Antenna Commutation.**

I. INTRODUCTION

Global navigation satellite system (GNSS) receivers allow the real-time computation of a vehicle´s position and velocity, generally referred as navigation solutions. For this purpose the receiver has to detect, track and demodulate at least four signals broadcasted from the satellites of the system constellation [1]. Currently, the two operative GNSS systems are the Global Position System (GPS), supported by the United States, and GLONASS developed by Russia that has been completely operational since 1995. Typical GNSS applications rely on a single antenna for satellite signals reception [2]. Since usual antenna radiation patterns are hemispherical, the antenna location in the vehicle must be properly chosen to maximize satellite visibility. Therefore, single-antenna receivers are useful only if the vehicle´s attitude does not depart significantly from their assumed values, as is often the case with cars, planes and ships. However, this is not the case for other applications where the vehicle´s attitude does change considerably, like during the flight of some satellites and rockets. Since vehicle dimensions are larger than the signal wavelength, the direct combination of multiple antennas creates interference patterns that preclude proper receiver operation. A multi-antenna receiver is required in these cases [3]. This kind of receiver can also be used for vehicle´s attitude determination [1], and currently they are also being proposed for usual GNSS applications because better interference and multipath mitigation techniques can be applied [4].

Direct sequence spread spectrum (DS-SS) signals are utilized in GNSS because they allow high time-resolution. Therefore, a correlation stage is needed at the receiver to despread them and obtain reasonable signal-to-noise ratios [1]. Tight code and carrier synchronization of the local replica is required to achieve the de-spreading. Typically, tracking loop schemes are adopted for code and carrier synchronization in real-time receivers due to their low computational complexity. We assume a multi-antenna receiver architecture where the signal from each antenna is correlated individually. The same code and carrier local replica is used for all the signals from different antennas when receiving a particular satellite signal, assuming the multi-correlator channel scheme of [4]. However, since the goal in this work is maximizing satellite visibility and not interference and/or multipath mitigation, the beamforming approach is not considered. Then, only the antenna that produces the highest signal-to-noise ratio will be used for the tracking of a given satellite.

Considering that the distance between the antennas deployed on a vehicle is in the order of meters and the carrier wavelength is approximately 0.2 meters, an antenna commutation can be unnoticed by a code loop but can severely affect a phase loop. The degradation caused by this effect to the GNSS satellite data demodulation and some techniques to cope with it has been recently reported on [5]. The sudden change in the input phase can be avoided if that phase difference can be properly measured before the commutation actually occurs. In this case, the radiation patterns of deployed antennas should have a significant overlapping to assure continuous satellite visibility under vehicle´s attitude changes. Then, there should be enough signal-to-noise ratio at the second best antenna to measure the phase difference accurately before the moment when this antenna becomes the best and the tracking loop should change its input and use the new signal. In this work, we propose to use an auxiliary carrier tracking loop to estimate the differences between the signals coming from

 ISBN: 978-1-61208-264-6

the best antenna and the second best one. In this way, the phase transient are completely avoided, the quality of phase measures preserved, and the data demodulation unaltered.

The rest of the paper is organized as follows. A digital model for the output of the correlation of the received GNSS signal from multiples antennas with the same code and carrier local replica is presented in Section 2. The proposed carrier tracking strategy is presented in Section 3. The proposed scheme is tested in a simulated low-earth orbit (LEO) satellite scenario in Section 4. The tracking transient effects found if a single carrier loop scheme is used, and their absence when the two-loop strategy is adopted, are verified. Finally, the conclusions and future work lines are given in Section 5.

II. Digital Measurements Model

Consider that N antennas have been deployed on a vehicle and connected to a multi-antenna GNSS receiver. According to the receiver architecture described in the previous section, the signal received at each antenna must be correlated with the same locally generated replica for each visible satellite. The complex correlations of the incoming signal at the i-th antenna, from a given satellite and for the k-th correlation interval of duration T, can be expressed as [1]

$$C_k^i = D_k \sqrt{T \left.\frac{C}{N_0}\right|_k^i} \operatorname{sinc}(\Delta f_k^i) R(\Delta \tau_k^i) e^{j(\pi \Delta f_k^i T + \Delta \theta_k^i)} + n_k^i \quad (1)$$

where $i = 1, ..., N$, $C/N_0|_k^i$ is the carrier power to noise power spectral density of the signal from antenna i, $\Delta\tau_k^i = \tau_k^i - \hat{\tau}_k$ is the code delay estimation error, $\Delta f_k^i = f_k^i - \hat{f}_k$ is the frequency estimation error, both assumed constant during the integration time, and $\Delta\theta_k^i = \theta_k^i - \hat{\theta}_k$ is the initial phase estimation error. The term n_k^i is a complex white Gaussian noise sequence with unit variance, assumed independent between antennas, $R(\cdot)$ is the code correlation function, and $\operatorname{sinc}(x) = \sin(\pi x)/(\pi x)$. This expression assumes that the binary data bits $D_k = \pm 1$ are the same in all the antenna signals –given the slow data rate, e.g., 50 bps for GPS– and that correlations are computed within the same bit period. This type of binary data modulation is present in the GPS and GLONASS civil signals and in the data components of composite modernized GNSS signals. Notice that the estimated values, which corresponds to the local-replica, are the same in the correlations of different antennas, and that the carrier power to noise power spectral density $C/N_0|_k^i$ is affected by the gain of each antenna according to the line-of-sight vector of the received satellite.

A. Phase Discrimination

After the acquisition process has been completed, i.e., in tracking conditions [1], code and frequency estimation errors are sufficiently small so that the functions $\operatorname{sinc}(\cdot)$ and $R(\cdot)$ can be approximated by 1. Hence, (1) becomes

$$C_k^i = I_k^i + jQ_k^i = D_k \sqrt{T \left.\frac{C}{N_0}\right|_k^i} e^{j\Delta\phi_i} + n_i \quad (2)$$

where we have defined $\Delta\phi_k^i = \phi_k^i - \hat{\phi}_k$, with $\phi_k^i = \pi f_k^i T + \theta_k^i$ and $\hat{\phi}_k = \pi \hat{f}_k T + \hat{\theta}_k$, to model the input and output of the digital carrier tracking loops [6].

The phase estimation error present in the signal of each antenna is obtained from the angle of the corresponding complex correlation. To avoid the effects of binary modulation, a two quadrant discriminator should be utilized. Then,

$$e_k^i = \tan^{-1}\left(\frac{Q_k^i}{I_k^i}\right) = \left[\Delta\phi_k^i + n_{\phi_k^i}\right]_\pi \quad (3)$$

where the notation $[\cdot]_\pi$ indicates that its argument is kept within the interval $(-\frac{\pi}{2}, \frac{\pi}{2}]$ by adding or subtracting π as many times as needed. The noise term $n_{\phi_k^i}$ has zero mean and a complicated probability distribution. However, for high $C/N_0|_k^i$ values, it can be approximated by a Gaussian distribution with zero mean and variance $1/(2TC/N_0|_k^i)$.

B. Carrier Tracking Loops

The phase error estimates obtained with (3) are ambiguous due to the periodic nature of the phase. This ambiguity is responsible of many of the non-linear behaviours present in phase locked loops (PLL). Due to these non-linearities the PLL can have very long lock-in times and low resistance to high dynamics, and therefore many GNSS receivers add a frequency locked loop (FLL) in a scheme called FLL-assisted-PLL [7]. In previous works we have proposed an alternative solution, called the unambiguous frequency aided (UFA) PLL [6]. In the UFA-PLL, the ambiguous phase discriminator values, e_k^i, are corrected by adding or subtracting an integer number of π. The corrected phase errors, u_k^i, are found such that the difference between two successive values is less than a quarter of a cycle in magnitude. Thus, starting with $u_0^i = e_0^i$, it must be hold that

$$u_k^i = e_k^i - I_\pi(e_k^i - u_{k-1}^i) \quad (4)$$

where $I_\pi(x) = x - [x]_\pi$ is like the integer part function, but with steps at the multiples of π. The obtained sequence of phase errors u_k^i has unambiguous values as long as the frequency error is lower than $1/(4T)$. We have also shown that the UFA-PLL has the same noise resistance, and so the same tracking threshold, that an equivalent FLL [8].

Through the rest of this work, the utilized carrier loop is the UFA-PLL shown in Figure 1 whose filter coefficients are $p_1 = C = 0.5$, $p_2 = 0.105$, and $p_3 = 0.0123$. For the correlation time, $T = 5$ms, the resulting PLL has an equivalent noise bandwidth of 75.6Hz. The two delays included in the loop model the real-time calculation of the correlations. One of them accounts for the time spent in the computation itself, and the second is present because the estimated values utilized to produce the local-replica used in the correlation have to be known before the calculations begin. That is, the estimated value $\hat{\phi}_k$ is obtained with the loop filter output of the $(k-1)$-th correlation interval, which in turn is calculated with the estimated value $\hat{\phi}_{(k-2)}$. The loop filter is optimized for the tracking of acceleration steps, which produces a quadratic ramp of phase at the loop input. This loop design has been implemented in experimental GPS receivers

 ISBN: 978-1-61208-264-6

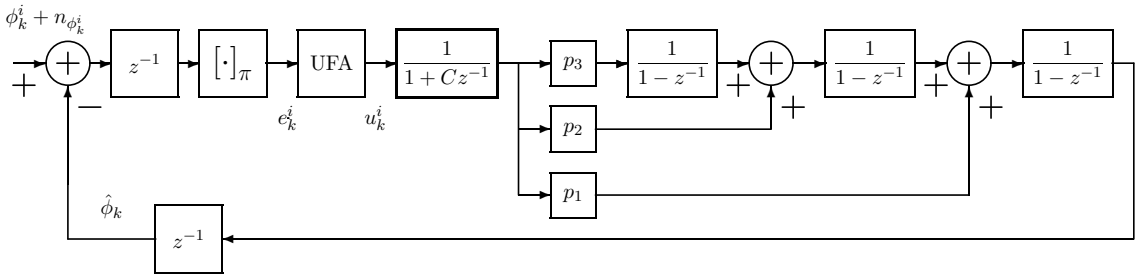

Fig. 1. Block diagram of the UFA-PLL model.

[6], and more details and properties can be found in [9]. The loop models previously described can be used operating data-bits synchronously as typically done, but can also be extended for data-bit asynchronous operation as proposed in [10].

III. The Two Loops Tracking Strategy

Assume the receiver is tracking a given satellite at the antenna l and that, due to the change in the vehicle´s attitude, the $C/N_0|_k^l$ values are decreasing and the $C/N_0|_k^j$ values, at the antenna j, are increasing. For the sake of simplicity, assume that the rest of the antennas has no useful signal levels. The correlations are computed based on the loop estimates computed with the signal from antenna l, but the error between the phase loop estimate and the phase of the signal from antena j can also be obtained as long as the $C/N_0|_k^j$ values are sufficiently high. This new phase error is

$$e_k^j = \tan^{-1}\left(\frac{Q_k^j}{I_k^j}\right) = \left[\Delta\phi_k^j + n_{\phi_k^j}\right]_\pi \qquad (5)$$

where $\Delta\phi_k^j = \phi_k^j - \hat{\phi}_k$. The phase error needed to build a new loop to track the signal from antenna j should be calculated with respect to a different phase estimate. However, if we assume that the frequency estimates from both loops are sufficiently close, the new phase error can be obtained from (5) by correcting it with the difference between both loop phase estimates. If we call $\hat{\phi}_k^M = \hat{\phi}_k$, the phase estimates of the actual loop or master loop, the phase error of an auxiliary loop, with phase estimate $\hat{\phi}_k^A$, is

$$eA_k^j = \left[e_k^j + \hat{\phi}_k^M - \hat{\phi}_k^A\right]_\pi = \left[\left[\Delta\phi_k^j + n_{\phi_k^j}\right]_\pi + \hat{\phi}_k^M - \hat{\phi}_k^A\right]_\pi$$

$$= \left[(\phi_k^j - \hat{\phi}_k^M + n_{\phi_k^j}) + \hat{\phi}_k^M - \hat{\phi}_k^A\right]_\pi = \left[\phi_k^j - \hat{\phi}_k^A + n_{\phi_k^j}\right]_\pi . \qquad (6)$$

The $[\cdot]_\pi$ operation is needed to obtain a phase error in the same range of values than the produced by a two quadrant inverse tangent. Notice that in the previous cases this operation was used to model the ambiguity of the measured phase error, but now it has to be actually implemented as part of the signal processing needed for the new auxiliary loop, which has input ϕ_k^j and output $\hat{\phi}_k^A$. The loop filter used for the auxiliary loop is exactly the same that the one used in the master loop. The reason for this choice will be clear in the following subsection.

A. Master Loop Actualization

Assume that the auxiliary loop has already been started and its initial transient, due to the initial phase and frequency errors, is already extinguished. Also assume that at the present moment the measured power at the antenna l becomes lower than the one at the antenna j. At this point the loop with the best estimates is the auxiliary one, and there is no reason to keep using the same loop estimates as parameters for the local-replica. Then, the master loop internal variables are overwritten by the ones from the auxiliary loop, and from now on its input is taken from the j antenna. In this way, the master loop is again tracking the best antenna, and the change has not produced any transient. Therefore, the logic for the master loop actualization is simple: each time that the power on the auxiliary loop becomes higher than the power on the master, the input of the master loop has to be changed by the auxiliary one. Depending on the auxiliary loop actualization logic, both loops can be tracking the signal from the same or different antennas. When both loops are tracking the signal from the same antenna no master loop actualization is possible, and the correction term of (6) becomes zero, and then $eA_k^j = eM_k^j$.

B. Auxiliary Loop Actualization

Now is clear that the aim of the auxiliary loop is to track the signal from the second best antenna whenever it is possible. Then, two possible situations have to be managed. The first is when the master loop is tracking the best antenna and the auxiliary one is properly tracking another antenna, which is not the second best antenna any more. That means that there is a better signal to be tracked with the auxiliary loop. Then, a direct commutation between these signals should be done at this loop. Of course, this change will produce a transient due to phase and frequency variations caused by the different physical locations and velocities of these antennas. However, since this loop is not generating the local-replica, the actual signal tracking will not be affected. The second situation is that the tracked signal in the auxiliary loop is actually the second best, but its power is too low to guarantee a satisfactory tracking. Then, the only possible option for the auxiliary loop is to switch its input to the same antenna that the master one. When this is the case, both loops should track the same signal until the second best antenna reaches a highly enough power level. At this point, the auxiliary loop should commute to this new antenna. Again, this change will cause a transient in the auxiliary loop, but it will not affect the master one.

 ISBN: 978-1-61208-264-6

TABLE I
ALGORITHMIC DESCRIPTION OF THE LOOP ACTUALIZATION.

if $P[a] > P[m]$ **then**
  $m \leftarrow a$
  Master loop variables $\leftarrow$ Auxiliary loop variables
end if
if $m = b$ **and** $P[s] > P[b]/10$ **then**
  $a \leftarrow s$
else
  $a \leftarrow b$
end if

C. Power Estimation

The strategy presented in this work needs a periodic estimation of the received power level for each satellite in view and for each antenna. This information can be obtained almost directly from the already computed correlations, (1), assuming that no interferences or severe signal obstructions or reflections are considered. A raw estimate of the received signal power from antenna i can be obtained as

$$\hat{P}_k^i = |C_k^i|^2 = (I_k^i)^2 + (Q_k^i)^2 = T \left.\frac{C}{N_0}\right|_k^i + noise \ . \quad (7)$$

Based on these values, better power estimates can be obtained by temporal filtering accordingly to the desired trade-off between noise reduction and the maximum rate of change of the filtered estimates, which is in turn established by the vehicle´s dynamics. One simple option is to take the average of each of these values during a selected time-window.

D. Summary of the Algorithm

A commutation period should be selected according to the expected vehicle´s dynamics, namely $L = KT$, with $K \in \mathbb{R}$. Then, every L seconds, a vector of estimated power at each antenna should be computed,

$$\bar{P} = [P[1]P[2] \cdots P[N]] \quad (8)$$

where each components is obtained as described in the previous subsection. Then, this vector has to be ordered and the two highest values and their corresponding indexes stored. If we called b the index of the first best antenna, and s to the index of the second best antenna, then $P[b] > P[s]$. Now consider that m and a are variables that indicate the number of the antenna selected for the master and the auxiliary loop respectively. Then, assuming that after the acquisition process of the satellite signal the loops are initialized with the best and the second best antenna at that moment, the algorithmic description –in pseudo code– of the proposed two loops tracking strategy is presented in Table I. In this code, it was considered that 10 dB less than the power of the signal in the master loop is the maximum difference allowed to the auxiliary loop to track a different signal.

IV. APPLICATION TO A LEO SATELLITE SCENARIO

In order to test the proposed tracking strategy, a LEO satellite scenario was simulated assuming a constant change of attitude due to a roll movement along the orbit direction vector of 5 revolutions per minute (rpm). This kind of rotation can be found during the first moments of the satellite life due to the spin stabilization used by the launching vehicles. In this case, the signals from the GNSS satellites can arrive from any direction. Then, the tetrahedron geometry shown in Figure 2 (a) was adopted for the placement of four antennas. The use of such non-aligned antenna array for this type of space application has been proposed in [11]. A typical GPS satellite constellation was considered and the position and velocity of each visible satellite were calculated. The same values were obtained for each antenna attached to the LEO satellite, whose trajectory is plotted in Figure 2 (b). Thirteen GPS satellites were found in view during some part of the 10 minutes of simulated trajectory. Notice that given the high velocity of the LEO satellite, $\simeq 7$ km/s, the time in view of a GPS satellite is much shorter than the found in earth applications. Based on the position and velocity values obtained, line-of-sight vectors, distances, and rate of change in these distances were computed every 10 ms to generate the input signals for the following digital processing. The change of the power level received at each antenna is a critical aspect in this analysis and therefore a realistic radiation pattern was considered. Since the GPS signals are radiating using right-handed circularly-polarized (RHCP) signals, the gain pattern of a typical patch antenna at the GPS L1 band (1575 MHz) was considered. The antenna gain pattern adopted is shown in Figure 2 (c).

A. Carrier tracking loop simulation

The loop simulations made are based on the correlation output model of (1). Then, the inputs required for each antenna and visible satellite are the carrier power to noise power spectral density, $C/N_0|_k^i$, the instantaneous carrier frequency f_k^i and the instantaneous input phase, θ_k^i. Since the code loops are not considered in this work, perfect code estimation is assumed. Neglecting second order terms, the instantaneous phase of the received signal can be obtained directly dividing the distance from the GPS satellite to the considered receiver´s antenna by the carrier wavelength, which is $\lambda \simeq 19$ cm for the GPS L1 frequency. In the same way, the frequency changes can be obtained considering only the Doppler effect, i.e., dividing the rate of change of the distance by λ. Finally, the gain factor G_{RHCP}, obtained with the line-of-sight vector and the gain pattern of the antennas, is converted into carrier power to noise power spectral density, according to

$$C/N_0|_k^i[dB] = G_{RHCP}[\text{dB}] + 42[\text{dB/Hz}] \quad (9)$$

where the value 42 dB/Hz, was obtained considering 2 dB of antenna losses, equivalent noise temperature of the antenna 130K, cable losses of 0.4dB and receiver noise figure of 1 dB.

B. Simulation results

The results presented in the first place correspond to a single loop tracking strategy. It simply consists on changing the loop input each time that the receiver detects that a better signal is available from another antenna. Only the results obtained with the tracking of one of the GPS satellites in view are presented due to space limitations. In Figure 3 (a), the C/N_0

 ISBN: 978-1-61208-264-6

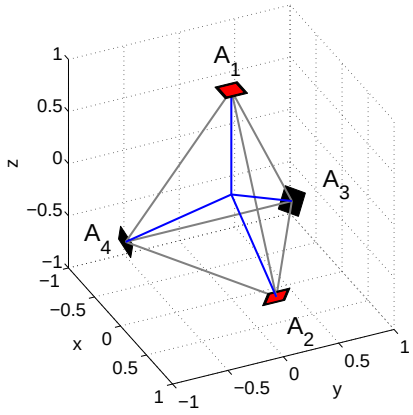

(a) Four antenna geometry on the LEO satellite.

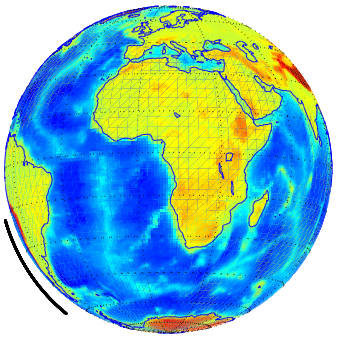

(b) Simulated LEO satellite trajectory.

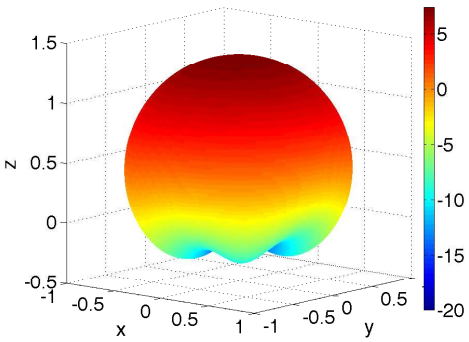

(c) Radiation pattern of a single antenna. RHCP gain in dB.

Fig. 2. Main elements of the simulated scenario.

levels of the signals received with each of the four antennas are plotted, for the first 30 seconds of the simulation, together with the indication of which antenna was used as input to the loop. A time-window of 0.25 seconds was selected for the power estimation average. The correct antenna selection made based on this power estimates, and the delay imposed by the averaging process can be clearly appreciated. The phase and frequency errors of the loop are presented in Figures 3 (b) and (c). Besides the first transient caused by the loop initialization, it can be clearly noticed the presence of a phase and frequency transients caused by the loop input commutations. Notice that half-cycle ambiguities present in the phase error were removed to appreciate the tracking error in a proper scale. These ambiguities can be easily compensated by the receiver, allowing continuous and reliable data demodulation.

The results obtained in the same situation but using the proposed two-loops tracking strategy are presented in Figure 4. In Figure 4 (a) the indication of the antennas selected as the input for the master and the auxiliary loops are plotted. It can be noticed that the master loop uses as input practically the same antenna that it would be used by the single loop. However, since its signal has been already tracked by the auxiliary loop, at the time of commutation the master loop can be properly initialized, and correspondingly a transient-free response is obtained as depicted in Figures 4 (b) and (c). Finally, it can be also appreciated that the estimation error levels change accordingly with the variation of the C/N_0 values of the tracked signal, as expected.

V. Conclusion and Future Work

An efficient tracking strategy devised for real-time multi-antenna GNSS receivers has been presented. The considered receiver architecture computes the correlations of the signal from each antenna with a common local-replica, for each tracked satellite. The use of a single carrier tracking loop in this kind of receiver will cause transient errors each time a commutation of the antenna used as loop input is done. These transients degrade the navigation measurements, affect data demodulation, and can produce a loss of signal tracking. The two-loop proposed strategy avoids these transients by properly modifying the internal loop variables at the moments of the commutations. The values of these variables are obtained by a second, twin loop, which does not require the calculation of extra correlations. The proposed strategy has been described in detail and tested in a simulated four-antenna LEO satellite scenario verifying that all the GPS satellites in view can be continuously tracked in the adverse situation of a rolling movement of 5 rpm.

The computational cost of the proposed strategy is minor assuming that in a multi-antenna receiver the power estimation and antenna selection algorithm is mandatory. Given the inherent increase of complexity of managing many radio-frequency inputs coherently, their digitalization, and the computation of the multi-correlations simultaneously, the cost of the extra loop seems negligible. The authors are now working on that multi-correlator architecture to be implemented in field programmable gate arrays (FPGA), and in the design of an experimental multi-antenna GNSS receiver.

VI. Acknowledgment

This work was funded by ANPCyT PICT 2011-0909 and UNLP 11-I-166.

References

[1] B. W. Parkinson and J. J. Spilker (eds.), *Global Positioning System: Theory and Applications*. Washington: American Institute of Aeronautics and Astronautics (AIAA), 1996.

[2] E. D. Kaplan, *Understanding GPS: Principles and Applications*. Boston: Artech House, 1996.

 ISBN: 978-1-61208-264-6

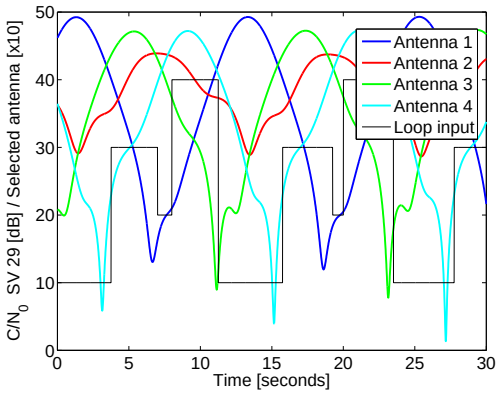

(a) C/N_0 values at each antenna and antenna selection.

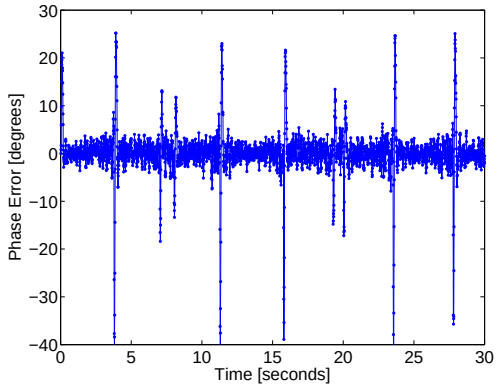

(b) Phase estimation error (commuted phase input).

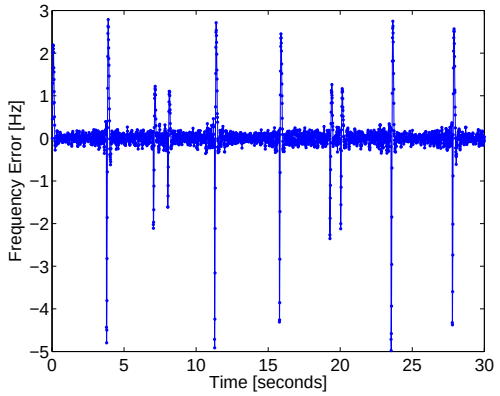

(c) Frequency estimation error (commuted frequency input).

Fig. 3. Tracking of SV 29 with a single loop strategy .

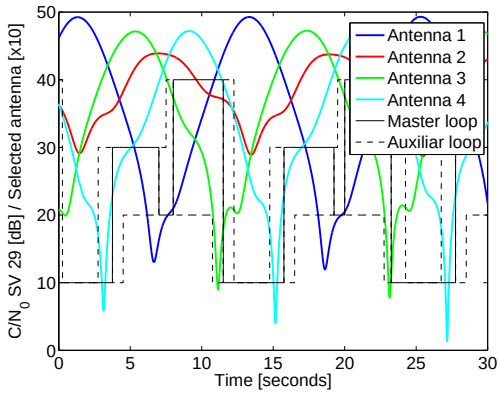

(a) C/N_0 values at each antenna and antenna selection.

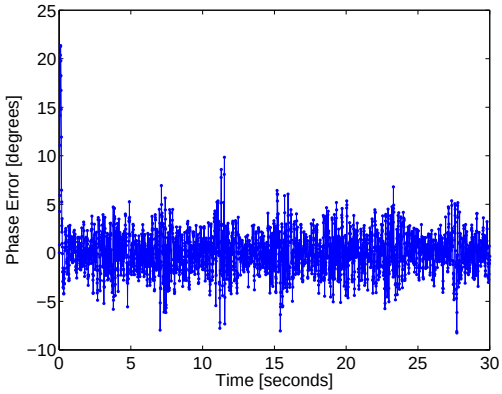

(b) Phase estimation error (commuted phase input).

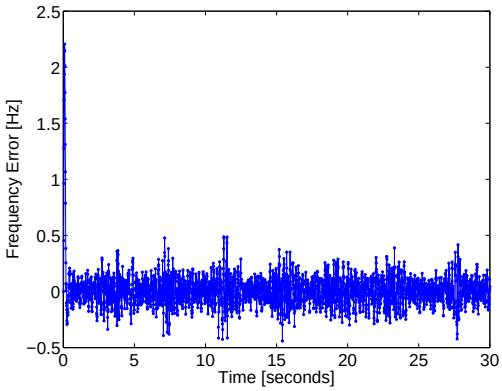

(c) Frequency estimation error (commuted frequency input).

Fig. 4. Tracking of SV 29 with the two loops strategy.

[3] T. Ebinuma, H. Saito, K. Tanaka, and T. Miyoshi, "GPS Signal Tracking on Spinning Vehicles with Antenna Diversity Techniques," in *Proccedings of ION GNSS 2009*, Savannah, GA, USA, September 2009, pp. 1413 – 1418.

[4] Kappen, G., C. Haettich, and M. Meurer, "Towards a Robust Multi-Antenna Mass Market GNSS Receiver," in *Proceedings of IEEE/ION PLANS 2012*, Myrtle Beach, SC, USA, April 2012, pp. 291–300.

[5] K. Harima, H. Saito, and T. Ebinuma, "Navigation Message Demodulation for GPS Receiver On-board Spinning Rockets," *GPS Solutions*, vol. 16, no. 4, pp. 495 – 505, October 2012.

[6] P. A. Roncagliolo and J. G. García, "High Dynamics and False Lock Resistant GNSS Carrier Tracking Loops," in *Proceedings ION GNSS 2007*, Fort Worth, TX, USA, September 2007, pp. 2364 – 2375.

[7] P. W. Ward, "Performance comparisons between FLL, PLL and a novel FLL-assisted-PLL carrier tracking loop under RF interference conditions," in *Proccedings of ION GPS 1998*, Nashville, TE, USA, September 1998, pp. 783 – 795.

[8] P. A. Roncagliolo, J. G. García, and C. H. Muravchik, "Pull-out Probability and Tracking Threshold Analysis for High Dynamics GNSS Carrier Loops," in *Proceedings of ION GNSS 2008*, Fort Worth, TX, USA, September 2008, pp. 221 – 228.

[9] P. A. Roncagliolo, J. G. García, and C. H. Muravchik, "Optimized Carrier Tracking Loop Design for Real-Time High-Dynamics GNSS Receivers," *Int. Journal of Navigation and Observation*, pp. 1–18, 2012.

[10] ——, "Data-Bits Asynchronous Tracking Loop Scheme for High Performance Real-Time GNSS Receivers," in *Proceedings of SPACOMM 2012*, Chamonix, France, April 2012, pp. 108 – 113.

[11] E. G. Lightsey, "Development and Flight Demonstration of a GPS Receiver for Space," Ph.D. dissertation, Department of Aeronautics and Astronautics, Stanford University, United States, Febraury 1997.

 ISBN: 978-1-61208-264-6